

Photocopy and Use Authorization

In presenting this thesis in partial fulfillment of the requirements for an advanced degree at Idaho State University, I agree that the Library shall make it freely available for inspection. I further state that permission for extensive copying of my thesis for scholarly purposes may be granted by the Dean of the Graduate School, Dean of my academic division, or by the University Librarian. It is understood that any copying or publication of this thesis for financial gain shall not be allowed without my written permission.

Signature _____

Date _____

A Novel Union of LiDAR and InSAR Analysis to Explore the Spatial Distribution and
Temporal Behavior of Landslides in Yellowstone National Park

by

Kyra Bornong

A thesis

submitted in partial fulfillment

of the requirements for the degree of

Master of Science in Geology

Idaho State University

Summer 2023

Copyright (2023) Kyra Bornong

To the Graduate Faculty:

The members of the committee appointed to examine the thesis of KYRA BORNONG find it satisfactory and recommend that it be accepted.

Dr. Benjamin Crosby,
Major Advisor

Dr. Glenn Thackray,
Committee Member

Dr. Colden Baxter,
Graduate Faculty Representative

Acknowledgments

Firstly, I would like to thank my advisor Ben Crosby, for his endless encouragement, enthusiasm, and support over the last two years. I would also like to thank Glenn Thackray and Colden Baxter, my committee members for their guidance and flexibility. Jefferson Hungerford of the NPS generously granted us permits to work and camp in Yellowstone; Al Handwerker at JPL provided indispensable guidance and assurance on our InSAR processing and interpretation. I had multiple field assistants who ensured that I was not eaten by bears while crawling over hillsides in Yellowstone; they included Katelyn Genta, Tyler Paladino, Becca Goughnour, Jase Clanton, and Joe Bornong (thanks Dad!!). I want to acknowledge Carrie Bottenberg and other denizens of the DML for their advice, solicited and not, and general good humor. Finally, I could not have done this work without the support of my fellow ISU graduate students not already mentioned, including (and not limited to!) Sarah Newcomb, Andrew Yokel-Deliduka, Matt Ruggiero, Olivia Stanley, Kyle Paulekas, and Robbie Manta.

This work was supported by the Geslin Grant, the Center for Ecological Research and Education, and ISU's Office of Research. These organizations provided financial support for my summer field work and research, as well as travel to GSA to share some of this work.

Table of Contents

Acknowledgments.....	iv
List of Figures.....	x
List of Tables	xi
List of Frequently Used Abbreviations.....	xii
1. Introduction.....	1
1.1. Motivation.....	1
1.2. Problem Statement.....	1
1.3. Landslides	2
1.3.1. Definitions and Classification.....	2
1.3.2. Rock Glaciers.....	3
1.3.3. Why Do Landslides Occur?	4
1.3.4. Landslide Creep	5
1.3.5. Landslides and Climate Change.....	6
1.4. Landslide Inventories.....	7
1.4.1. Types.....	7
1.4.2. Techniques	7
1.5. InSAR	9
1.5.1. What is InSAR and How Does it Work?	9
1.5.2. InSAR Limitations	11
1.5.3. InSAR Time Series Analysis	12

1.5.4. InSAR Applications to Landslides.....	13
1.6. Motivation to Study Landslides in Yellowstone National Park.....	14
1.6.1. Geographic Context and LiDAR Availability	14
1.6.2. Bedrock Geology	15
1.6.3. Glaciation.....	16
1.6.4. Precipitation	17
1.6.5. Earthquakes.....	17
1.6.6. Climate Change Predictions.....	18
1.6.7. Visitors and Park Infrastructure	18
1.6.8. Previous Landslide Mapping	19
1.7. Conclusion	20
1.8. Figures.....	21
1.9. References.....	27
2. A LiDAR-Based Landslide Inventory and Analysis of Landslide Distribution in Yellowstone National Park	46
2.1. Introduction.....	46
2.1.1. Why Study Landslides	46
2.1.2. Landslide Inventories.....	47
2.1.3. Knowledge Gap/Opportunity.....	48
2.2. Site Description.....	49
2.3. Methods.....	51
2.3.1. Data Sets	51

2.3.2.	GIS Inventory Structure.....	52
2.3.3.	Identification of Landslide Deposits.....	52
2.3.4.	Field Observations	53
2.3.5.	Classifying Landslide Deposits.....	54
2.3.6.	Rock Glaciers.....	55
2.3.7.	Extracting Attributes.....	55
2.3.8.	Visualization and Analysis Tools	56
2.4.	Results.....	57
2.4.1.	Characteristics of Landslide Types.....	57
2.4.2.	Spatial Distribution of Entire Inventory	60
2.4.3.	Distribution of Landslide Types	61
2.4.4.	Substrate Lithologies	61
2.5.	Discussion.....	62
2.5.1.	Different Landslide Risks Throughout the Park.....	62
2.5.2.	Lithologic Influence on Landslide Distribution.....	62
2.5.3.	Open-Slope Debris Flows Dominate Landslide Type	64
2.5.4.	The Conceptual Yellowstone Landslide	65
2.5.5.	Comparison to Previous Yellowstone Inventories.....	66
2.5.6.	Extraordinary Preservation of Deposits	66
2.5.7.	The Advantage to Non-Automated Mapping	67
2.5.8.	Limitations of this Inventory	67
2.6.	Conclusion	68
2.7.	Figures.....	70

2.8.	References.....	75
3.	Using InSAR to Identify Creeping Landslides in Yellowstone.....	85
3.1.	Introduction.....	85
3.2.	Site Description.....	87
3.3.	Methods.....	89
3.3.1.	Data Acquisition and InSAR Processing	89
3.3.2.	MintPy Velocity Inventory	90
3.3.3.	Time Series Analysis on Individual Features	91
3.4.	Results.....	92
3.4.1.	Movement Inventory.....	92
3.4.2.	Time Series of Motion	93
3.5.	Discussion.....	95
3.5.1.	LiDAR Inventory vs. InSAR Inventory.....	95
3.5.2.	Time Series Interpretations	96
3.5.3.	Hazard/Risk Implications.....	98
3.5.4.	Limitations and Future Opportunities.....	98
3.6.	Conclusion	100
3.7.	Figures.....	101
3.8.	References.....	107
4.	Conclusion	113
4.1.	Summary.....	113

4.2.	Limitations	114
4.3.	Opportunities.....	115
4.4.	Recommendations for Future Landslide Inventories.....	116
4.5.	References.....	119

List of Figures

Figure 1.1 Proposed national landslide database.....	21
Figure 1.2 Examples of landslide inventories.....	22
Figure 1.3 Schematic InSAR measurement.....	23
Figure 1.4 Reference map of Yellowstone.....	25
Figure 1.5 Potential drivers of landslide activity.....	26
Figure 2.1 Example landslide types.....	70
Figure 2.2 Spatial distribution of LiDAR-mapped landslides.....	71
Figure 2.3 Distribution of landslide types.....	72
Figure 2.4 Distribution of source lithologies.....	73
Figure 2.5 Conceptual landslide cross-section.....	74
Figure 3.1 Hypothetical displacement time series.....	101
Figure 3.2 Conceptualization of interferogram network.....	102
Figure 3.3 Park wide distribution of creeping and stable landslides.....	103
Figure 3.4 Pie charts of landslide types.....	104
Figure 3.5 Bar plot of landslide source lithologies.....	105
Figure 3.6 Displacement time series of 3 landslides.....	106

List of Tables

Table 1.1 List of SAR satellites.....24

List of Frequently Used Abbreviations

DEM Digital Elevation Model

LiDAR Light Detection and Ranging

InSAR Interferometric Synthetic Aperture Radar

Ma millions of years before present

ka thousands of years before present

mm millimeters

cm centimeters

m meters

USGS United States Geological Survey

MintPy Miami InSAR Time-series software in PYthon

A Novel Union of LiDAR and InSAR Analysis to Explore the Spatial Distribution and Temporal
Behavior of Landslides in Yellowstone National Park

Thesis Abstract–Idaho State University (2023)

Landslide inventories are critical to assessing landslide hazards and to understanding processes that drive long-term landscape evolution. Here we use LiDAR to create a landslide inventory of all of Yellowstone National Park and InSAR time series analysis to assess the activity state of those landslides. We manually mapped and classified ~1800 deposits in LiDAR and measured ~200 of them actively creeping between May 2017 and October 2021. We determined that most landslides occur as flow-type movements and bedrock lithology likely influences landslide distribution throughout the park. Creeping movement (on cm/year scales) occurs on many of the largest landslide deposits and creep rates vary over time. We identified continuous, event-based, and seasonal displacement patterns that likely reflect different failure mechanisms and forcing processes. This project lays a robust foundation for landslide hazard assessment and landscape evolution investigations in Yellowstone.

Keywords: landslides, landslide inventory, LiDAR, InSAR, Yellowstone, geomorphology, creep, time series

1. Introduction

1.1. Motivation

Landslides are widespread and destructive geologic hazards, posing risk especially in places where human infrastructure intersects with landslide-prone terrain. Globally, they are estimated to kill thousands of people (Froude and Petley, 2018) and cause billions of dollars in damage to infrastructure annually (Klose et al., 2016; Godt et al., 2022), and are particularly frequent and abundant in mountainous regions (Schlögl et al., 2019). Understanding where and why landslides occur is essential for assessing landslide hazard, particularly in light of a changing climate and a growing human population that encroaches on ever-more susceptible terrain.

The United States' executive branch passed the National Landslide Preparedness Act in 2021. The act aims to reduce losses due to landslides through coordinated efforts to identify and communicate landslide hazard and risk and to improve planning and emergency response (Godt et al., 2022), supporting a major investment in landslide science in the coming decade. A fundamental step in assessing landslide hazard and risk is documenting where landslides occur. Proposed products such as the National Landslide Database (Figure 1.1) and automated monitoring tools are essential for predicting where they may occur in the future and preparing for such events.

1.2. Problem Statement

This study aims to combine two remote sensing datasets from LiDAR (Light Detection and Ranging) and InSAR (Differential Interferometry Synthetic Aperture Radar) with field observations to create multiple landslide inventories for Yellowstone National Park. Collection

of the first park-wide, high-resolution LiDAR topographic dataset in October 2020 created an opportunity to map surficial features, including landslides, with an unprecedented level of detail and accuracy. We use InSAR to interrogate the LiDAR inventory for actively creeping landslides and construct time series of displacement for selected movements. Both the LiDAR- and InSAR-derived data sets are foundational products for future investigations of landslide hazard and risk assessment throughout the park as well as the analysis of patterns of landscape evolution in this unique geologic setting.

1.3. Landslides

1.3.1. Definitions and Classification

In general, we use the term “landslide” to describe the subaerial downslope movement of a significant volume of material. Our use of the term landslide is interchangeable with terms like “slope failure” and “mass movement.” These movements can occur at rates as slow as mm/year and as fast as m/sec and range from infrequent episodes of activity to nearly continuous (Hungr et al., 2014). We use specific terms to refer to distinguish different types of landslides, classifying by their style of movement and the type of material in motion (Cruden and Varnes, 1996; Hungr et al., 2014). These broadly utilized classifications focus on observable characteristics, minimizing interpretation. Because the types differentiate failure mechanisms and thus characterize the rate or extent of movement, they are useful in assessing risk and choosing mitigation strategies (Highland and Bobrowsky, 2008).

Types of material are based on grain size. We classify materials as rock (intact bedrock prior to movement), debris (aggregate particles of which 20% or more are greater than 2 mm in diameter), and earth (aggregate particles of which 20% or less are greater than 2 mm in

diameter). Styles of movement describe how the material is displaced and include falls, slides, and flows (Cruden and Varnes, 1996; Hungr et al., 2014). A fully classified landslide combines definitions for material and movement such as a “rock slide” or a “debris flow.” A deposit from a single event may contain multiple zones sourced from different styles of movement or materials and are classified as “complexes.” Most landslides, especially larger ones, could be called complexes. Different types of movement can occur on at the same feature simultaneously or at different times (Highland and Bobrowsky, 2008). Here, we use complexes to describe landslide deposits where a zone of the deposit, defined by one type, appears to influence movement of another type, within the same contiguous landslide deposit.

As with any classification scheme, landslides can be further broken down into different types that imply additional characteristics, including temporal history of the movement (e.g., Hungr et al., 2014). In this study we opt for simplified classifications following Burns and Madin (2009) and Slaughter et al. (2017) to be consistent with other regional work (e.g., Lingbloom 2022) and to directly reflect the observations we are making while limiting assumptions or interpretations as much as possible in the mapping process.

1.3.2. Rock Glaciers

Ice-influenced landforms are not typically included in landslide classification schemes (Cruden and Varnes, 1996), but we propose in this study that rock glaciers share key morphological and kinematic characteristics with landslides that warrant their inclusion in our inventory. Rock glaciers are masses of rocky debris and ice that slowly deform downslope and are common in alpine settings (Hamilton and Whalley, 1995; Whalley and Azizi, 2003; Anderson et al., 2018). They accelerate the transport of debris from valley headwalls to valley

floors (Anderson et al., 2018) and respond to multi-year shifts in precipitation patterns (Brencher et al., 2021). Some rock glaciers are thought to have formed through the interaction of landslide processes such as rockfall with glaciers or snow fields (Whalley and Azizi, 2003), which would make them landslide deposits in the conventional sense. The oversteepened snouts of rock glaciers can pose similar hazards as landslides (Anderson et al., 2018). Including rock glaciers in our landslide inventory gives a more complete record of mass movement processes in our study area with regard to both unstable slope hazards and landscape evolution processes.

1.3.3. Why Do Landslides Occur?

Landslides occur where the shear stress along a rupture surface is equal to or greater than the shear strength of that surface (Carson and Kirkby, 1972). These stresses are affected by slope angle, pore water pressure, cohesion, and the angle of internal friction and other factors (Crozier, 2010). These factors are influenced by the material and topographic properties of a hillslope as well as environmental conditions. Landslides can occur both without an obvious trigger and in response to other natural hazards including earthquakes or intense storms (Godt et al., 2022). Identifying where past landslides have occurred, the local characteristics that make particular slopes susceptible to failure and the local triggering forces are an important step in assessing where future landslides are likely to occur.

Initial slope failures and subsequent reactivations are driven by a variety of processes acting on a wide range of time scales. Bedrock lithology is an important control on topographic form (Korup, 2008), influencing slope angles. Material and structural properties of different bedrock units exert a control on landslide distribution (Roering et al., 2005; Xu et al., 2021); dip-slope oriented fractures or clay-rich interbeds can offer zones of instability (e.g., Calabro et al.,

2010). Human modification can destabilize slopes through oversteepening (e.g., Froude and Petley, 2018) or diminished cohesion through vegetation clearing (e.g., Montgomery et al., 2000; Crozier, 2010). Similarly, wildfires kill vegetation and decrease infiltration rates, often resulting in channelized debris flows (DeGraff et al., 2015). Glacial debuitressing also triggers landslides; as ice retreats and modern climate change destabilizes permafrost, oversteepened valley walls collapse towards a more stable angle over thousands of years (Ballantyne, 2002; Holm et al., 2004; Cossart et al., 2014).

Though landslides can occur without any obvious trigger, many landslide events are driven by other natural hazards. Earthquakes often trigger widespread landsliding (Tian et al., 2022). Significant precipitation events, especially those within a context of longer-term precipitation patterns decrease hillslope cohesion and lead to slope failures (Coe et al., 2003, 2014; Crozier, 2010; Handwerger et al., 2019b, 2019a, 2022). Snowmelt-related failures are common in regions with a significant snowpack as meltwater infiltrates the ground in the spring (Chleborad, 1998). None of these predisposing or triggering conditions or processes work in isolation from one another; interactions between some or all of them work together through time to create the landslide record we see on the landscape today.

1.3.4. Landslide Creep

In contrast to slope failures that displace a mass of material nearly instantaneously, many landslide features “creep” slowly (mm to cm/year) and nearly continually. Previous studies have found that creeping landslide and rock glacier behavior can be coupled to climate conditions (Handwerger et al., 2019a; Brencher et al., 2021) and respond to seasonal precipitation patterns (Coe et al., 2003). We contrast this phenomenon of landslide creep with shallow soil creep, in

which surficial soil layers move extremely slowly (less than 1 cm/year), as a result of volume changes driven by wetting and drying and freezing and thawing cycles (Hungr et al., 2014).

Continual deformation (particularly through landslide creep) can demand continuous upkeep of infrastructure such as roads, pipelines or other built features and it can also indicate incipient reactivation and the potential for catastrophic failure (e.g., Šilhán, 2020), making its identification and measurement valuable to a comprehensive risk assessment.

1.3.5. Landslides and Climate Change

As the Earth's climate warms, intense precipitation events are becoming more frequent (Seneviratne et al., 2012) and wildfire regimes are changing (Jia et al., 2019). Because they often respond to precipitation events, landslide patterns are likely to change as precipitation regimes become more frequent and intense (Gariano and Guzzetti, 2016). Intense precipitation events have been shown to trigger movement on previously stable features (Handwerger et al., 2019b). Post-wildfire debris flows can be incredibly destructive and occur on a range of time scales after fire activity and are often triggered by storm events that occur on previously burned hillslopes (Parise and Cannon, 2012). Additionally, in peri- and paraglacial settings, melting of glaciers and permafrost have been shown to change landslide activity (Borgatti and Soldati, 2010; Huggel et al., 2012). Mapping past occurrences of landslides now is critical for understanding the effects of climate change on the landscape.

1.4. Landslide Inventories

1.4.1. Types

Landslide inventories serve as foundational data sets for assessing landslide risk, studying landscape evolution, and investigating spatial and geologic patterns in landslide distribution. Inventories take a wide variety of forms (Figure 1.2), but generally describe the location and selected attributes of landslides within a region of interest (Guzzetti et al., 2012). Some inventories are compiled to characterize a specific type of slope failure such as earthflows (e.g., Hungr et al., 2008; Blahut et al., 2010; Lauknes et al., 2010; Mackey and Roering, 2011; Cafiso and Cappadonia, 2019). Landslide inventories can also be compiled immediately after an event to quantify the hillslope response to specific triggers including earthquakes, snow melt, or precipitation events (e.g., Keefer, 1984; Malamud et al., 2004; Coe et al., 2014; Marc et al., 2019; Jones et al., 2021). Many inventories record all deposits present on the landscape (e.g., Cardinali et al., 1990; Case, 1990; Bennett et al., 2016). A single landslide inventory map may contain a variety of landslide types that are attributed to different triggers (Figure 1.2). Given this diversity of inventories, it is important that each clearly state the intention and scope of the product.

1.4.2. Techniques

Landslide inventory mapping generally combines multiple remote sensing and/or field techniques. Technologies available to accomplish inventories have rapidly evolved over the last couple of decades. Interpretation of stereographic aerial imagery formed the basis of traditional inventories (Guzzetti et al., 2012). LiDAR interpretation, with its meter- to sub-meter scale and ability to characterize the texture of the bare ground beneath vegetation has been

transformational for landslide inventory mapping and other geomorphic studies (Roering et al., 2013). An investigator using LiDAR to inventory landslide deposits can identify up to 200 times the number of landslides as an investigator relying on aerial photography in the same area (Burns and Madin, 2009). Increasing availability and accessibility of LiDAR data (e.g. OpenTopography.org or the USGS 3DEP program) provides an impetus to revisit and update older, photo-based landslide inventories, especially in vegetated areas.

Field investigations are less effective at identifying the extent of landslides but may complement remote-sensing-based inventories by providing insights into the material character of the deposit or the activity of the feature not visible in the imagery (Guzzetti et al., 2012). Interferometric Synthetic Aperture Radar (InSAR) has also been widely used to identify and inventory actively moving landslides through measuring precise change on the surface of the earth (Guzzetti et al., 2009; Roering et al., 2009; Barboux et al., 2014; Su et al., 2022). This technique will be discussed in depth later in the subsequent section. Finally, inventories may also be based around an automated topographic classification scheme, though the computers have yet to fully match capability of a trained human eye (e.g., Roering et al., 2005; Booth et al., 2009; Bunn et al., 2019).

There is no single set of agreed-upon methods or protocols for creating a landslide inventory (Guzzetti et al., 2012), an issue that hampers the comparison between inventories prepared by different groups including private companies, academics, and state and federal agencies. In parts of the United States with significant landslide hazards, state agencies have created protocols to build landslide inventories that enable the creation of landslide susceptibility maps (e.g., Burns and Madin, 2009; Slaughter et al., 2017). Widespread adoption of these or

similar protocols would allow for better comparison between data sets compiled by different groups.

The internet greatly facilitates the communication of landslide inventory maps. Several state and federal agencies publish interactive web maps to share landslide inventories and other spatial geologic data sets (e.g., <https://www.usgs.gov/tools/us-landslide-inventory>, <https://www.dnr.wa.gov/geologyportal>, Figure 1.2). These public-facing maps can help create a greater awareness of landslide hazards and facilitate the sharing of data sets, while often illuminating stark contrasts between mapping approaches in different states (Mirus et al., 2020).

1.5. InSAR

1.5.1. What is InSAR and How Does it Work?

Synthetic aperture radar (SAR) uses microwave pulses to measure the Earth's surface. It is extremely sensitive to elevation change, capable of measuring phase differences between acquisitions that correspond to mm-scale change over large areas (Gabriel et al., 1989). SAR is also an active-source measurement that can penetrate clouds and is able to collect data at night (Ferretti et al., 2007). With repeat SAR acquisitions over the same area, we can create interferograms (InSAR), or maps of phase differences over tens to hundreds of kilometers. In its raw form, the change in SAR phase can be attributed to many processes, including atmospheric interference, the Earth's geometry, and differences in satellite geometry between acquisitions (Figure 1.3). With good estimates and models of the confounding processes (e.g., using a digital elevation model to remove the topographic phase or modeling out atmospheric effects based on global weather data), we can remove sources of error and noise and create maps of cm-scale deformation at the surface of the Earth.

SAR data are widely available; various countries have been launching SAR-equipped satellites since 1978 (Table 1.1). Different satellites offer advantages and disadvantages in terms of return times, orbit precision, measurement capabilities, and data accessibility and availability. There are also different software packages available for processing interferograms including ISCE (Rosen et al., 2012), ROI-PAC (Rosen et al., 2004), GMT-SAR (Sandwell et al., 2011), SNAP (Veci et al., 2017), and Gamma (Wegmüller et al., 2016). With the exception of Gamma, these software packages are free and open-source, though have varying capabilities and degrees of user-friendliness.

InSAR is able to measure change up to roughly half of the wavelength of the SAR instrument per pixel (Massonnet and Feigl, 1998). SAR sensors operate at different wavelengths which are suitable for measuring different rates of change. Signal wavelength is also related to a signal's ability to penetrate through the atmosphere and through vegetation (Meyer, 2019). Longer wavelengths can measure greater rates of change and better penetrate vegetation but suffer from ionospheric effects; shorter wavelengths can detect change at a higher resolution but have limited ability to penetrate dense vegetation. SAR satellites tend to operate at C-, L-, or X-band wavelengths which can measure up to about 2.5, 12, or 1.5 cm of change, respectively, in a single interferogram (Table 1.1).

InSAR has been used to study a myriad of different processes that manifest as change on the surface of the earth. These processes include, but are not limited to volcanic inflation and deflation (Rosen et al., 1996; Chang et al., 2007; Kelevitz et al., 2021); earthquake events (Funning et al., 2005; Hamling et al., 2017); fault creep (Funning et al., 2007; Marshall et al., 2013); subsidence due to groundwater withdrawal (Amelung et al., 1999; Nikos et al., 2016; Chaussard et al., 2021) or oil extraction (Fielding et al., 1998); flooding (Uddin et al., 2019);

permafrost active layer dynamics (Liu et al., 2010); permafrost thaw (Iwahana et al., 2016); changes in land or sea ice cover (Atwood et al., 2010; Meyer et al., 2011; Engram et al., 2018); and, of course, rock glacier (Liu et al., 2013; Brencher et al., 2021) and landslide creep (Roering et al., 2009; Calabro et al., 2010; Handwerger et al., 2015; Mantovani et al., 2019; Aslan et al., 2020; Solari et al., 2020; Hu and Bürgmann, 2020; Xu et al., 2021; Cook et al., 2022). With its diversity of applications, collection of SAR data with a focus on interferometry remains a priority for space agencies. Particularly exciting is the upcoming NASA/ISRO NISAR mission. Scheduled to launch in 2024, NISAR will collect L-band SAR with a 12-day repeat time over most of the earth and will provide direct download of SAR and InSAR products, eliminating the need for users to process their own interferograms (Rosen et al., 2017).

1.5.2. InSAR Limitations

Radar signals are affected by many sources of noise including the ionosphere and troposphere, scattering properties of different materials on of the Earth's surface (e.g., water vs. buildings), limitations related to the viewing geometry of the satellite (it cannot "see" movement that occurs parallel to its flight azimuth, typically north-south), and a small amount of random noise (Massonnet and Feigl, 1998). Large amounts of noise are responsible for a loss of coherence between SAR acquisitions and prevent accurate deformation estimation.

Interferograms also experience loss of coherence if deformation in an area exceeds the SAR instrument's measurement capacity (Calabro et al., 2010). Many of those sources of error may be mitigated by modeling atmospheric effects and removing them from an interferogram (Jolivet et al., 2014) and making choices based on local context to avoid widespread decorrelation involved with weather (e.g., Brencher et al., 2021). It is also important to double check InSAR data

against other sources of information such as digital elevation models, satellite imagery or, where available, GPS measurements before drawing conclusions.

1.5.3. InSAR Time Series Analysis

We can use a single interferogram to measure change between two points in time; we can also combine multiple (dozens to hundreds) interferograms to create a continuous time series of change. This time series analysis is both useful for overcoming decorrelation issues inherent to interferograms with long temporal baselines and can reveal patterns of movement that occur on variable time scales. Time series InSAR analysis can be broadly defined as either persistent scatterer (PS) or distributed scatterer (DS) methods. PS and DS methods tend to give similar results (Yan et al., 2012; Osmanoglu et al., 2016) but have strengths and limitations related to the phenomena they might be used to study.

PS InSAR relies on the identification of highly reflective, highly coherent, sub-pixel sized features to create a “natural GPS network” to measure deformation as a grid of points (Ferretti et al., 2001). Because of its need for high-coherence features, PS InSAR relies on the presence of these persistent scatterers and so it works best in urban or rocky environments and is of more limited use in vegetated ones. A lack of natural reflectors can be overcome by strategically placing artificial ones, but this requires planning (Crosetto et al., 2016). PS InSAR assumes linear deformation and uses interferograms that are all referenced to the same primary acquisition without any baseline limits (Yan et al., 2012). PS InSAR is ideal for measuring deformation of already-identified point features and works particularly well in urban areas where there is an abundance of persistent scatterers.

DS InSAR techniques rely on redundant and continuous networks of interferograms with small temporal and perpendicular baselines to create continuous deformation maps and velocity estimates over an entire acquisition area (Berardino et al., 2002; Yunjun et al., 2019). There are multiple available algorithms for exploiting these networks which take different approaches to estimating displacement and correcting errors (Yunjun et al., 2019). DS InSAR is useful for exploring large areas or examining deformation in places that lack persistent scatterers, such as forested terrain. For this last reason, we use DS InSAR in this project.

1.5.4. InSAR Applications to Landslides

As stated above, InSAR is widely used to study the motion of landslides and rock glaciers. These studies tend to fall into two broad categories: ones that create landslide or rock glacier inventories based on InSAR velocity maps (Aslan et al., 2020; Bekaert et al., 2020; Xu et al., 2021) and ones that use InSAR to investigate spatial and/or temporal patterns of movement within single, previously identified features (Delbridge et al., 2016; Mantovani et al., 2019; Cook et al., 2022). Many studies do both, creating an inventory to identify a small number of active features to focus on with the time series (Guzzetti et al., 2009; Liu et al., 2013; Roering et al., 2015; Solari et al., 2020; Brencher et al., 2021). C-band and L-band data are both commonly used to study landslides (e.g., Schlögel et al., 2015; Handwerger et al., 2015; Mantovani et al., 2019; Xu et al., 2021). Because creeping landslides move at rates in the range of cm/year, they are particularly well-suited to InSAR time series analysis.

We use the European Space Agency's Sentinel 1 A/B C-band SAR data in this study because it is open-access and is collected every 6-24 days at a given site. The Alaska Satellite Facility's HyP3 software allows users to download hundreds of already-processed interferograms

over a specified location and period of time (Hogenson et al., 2020). While it does not offer control over processing parameters (e.g., high-resolution DEMs for removing the topographic phase), Hyp3 offers a unique opportunity to leverage a large amount of data with relative ease and can hopefully overcome noise or errors present in single interferograms. The open-source Miami INsar Time-series software in PYthon (MintPy) offers a relatively user-friendly tool to perform a time-series analysis and multiple noise corrections on a stack of many interferograms to create displacement and velocity estimates (Yunjun et al., 2019).

1.6. Motivation to Study Landslides in Yellowstone National Park

1.6.1. Geographic Context and LiDAR Availability

Yellowstone National Park is located in northwest Wyoming and is well-known for its vast array of hydrothermal features and volcanic history. The park is centered on a broad, low-relief plateau surrounded to the northwest, north, east, and south by the rugged, higher-relief Gallatin, Beartooth, and Absaroka ranges respectively (Figure 1.4). While the driver behind the volcanic history is contested, (e.g., Christiansen et al., 2002; Camp and Wells, 2021) the Yellowstone Plateau is generally accepted to be the modern position of a time-transgressive hotspot that has been migrating northeastward across North America since at least 17 Ma (Pierce and Morgan, 2009). The hotspot reached its modern position around 2 Ma; massive, caldera-forming eruption cycles occurred around 2 Ma, 1.3 Ma, and 0.63 Ma (Christiansen, 2001). These calderas have largely collapsed and been filled in with rhyolite flows, creating the high-elevation, low relief plateau we see today.

The USGS collected 1-m resolution LiDAR topography data covering all of the park in October 2020. The data set is freely available (<https://apps.nationalmap.gov/lidar-explorer/#/>)

and provides unprecedented access to the ground surface in Yellowstone, revealing previously obscured faults, moraines, glacial lineations, and landslides (Crosby and Bornong, 2022).

Yellowstone's unique geologic and geographic setting, as well as its immense popularity as a national park, make it an exciting and societally relevant place to study landslides.

1.6.2. Bedrock Geology

Yellowstone National Park hosts a variety of rocks that reflect processes throughout the entire geologic history of North America (Figure 1.5D). Grouped by age, these rocks tend to occupy specific spatial domains throughout the park. Quaternary volcanic rocks dominate the center of the park, mostly in the form of extensive rhyolite flows and thick tuff deposits (Christiansen, 2001). Much of the landscape is mantled by glacial deposits from extensive ice cover during the Pleistocene (Pierce, 1979; Licciardi and Pierce, 2018).

Ringling the central plateau, the Absaroka Mountains and parts of the Gallatin Range are composed of the Absaroka Volcanic Supergroup, a collection of volcanic and interbedded sedimentary rocks related to pre-Yellowstone volcanic activity during the Eocene (Smedes and Prostka, 1972). Rocks in the Absaroka Volcanic Supergroup consist of basaltic and andesitic lava flows, tufts, and intrusive rocks, as well as clastic deposits sourced from them (Smedes and Prostka, 1972). The Absaroka volcanic processes are thought to have occurred independent of Yellowstone hot spot volcanism; if the hot spot existed during the Eocene, it would have been located much farther west (Camp and Wells, 2021). The Absaroka rocks have been deeply eroded, at present comprising the steep, rugged mountains on the eastern side of Yellowstone National Park.

Though not spatially extensive, Yellowstone hosts some sedimentary rocks of Mesozoic and Proterozoic ages as well as Precambrian metamorphic rocks. Precambrian gneiss and schist of the Wyoming Province crop out in the northern part of the park and are fairly uniform in lithology (Ruppel, 1972). Sedimentary rocks are largely exposed in the Gallatin Mountains and west of Two Ocean Plateau in the Basin Creek Uplift and the Red Mountains. The Gallatin Mountains and the Red Mountains were thought to have been structurally connected before hotspot volcanism (Christiansen, 2001) and so, though formation names are different, rocks in the south and northwest parts of the park share many characteristics. The Gallatin Range is made up of slightly north-dipping Middle Cambrian to Cretaceous-aged sedimentary rocks intruded by Tertiary-aged laccoliths, sills, and dikes (Ruppel, 1972). The Red Mountains and the Basin Creek Uplift in the southern part of the park are composed of Devonian- to Cretaceous-aged sedimentary rocks, topped, in places, by Absaroka and Quaternary volcanic rocks (Love and Keefer, 1975).

1.6.3. Glaciation

During the Pleistocene, the Yellowstone Plateau hosted the largest ice cap south of Laurentia during multiple glacial cycles (Figure 1.5C). During the most recent cycle, regionally called the Pinedale Glaciation, glaciers sourced from the surrounding mountain ranges coalesced onto the plateau ~22 ka and formed an ice cap that retreated ~13 ka. Ice retreat is thought to have been rapid, occurring over about 1000 years (Licciardi and Pierce, 2018; Licciardi et al., 2022). From a landslide perspective, this glacial history is important for two reasons. First, we assume that the ice sheet eroded older surficial deposits. Consequently, the features we see today represent the cumulative record of geomorphic events and processes that have occurred, on a

variety of time scales, since glacial retreat. Second, the ice retreat itself creates a mechanism for landsliding through glacial debuttressing and the mobilization and deposition of unconsolidated materials.

1.6.4. Precipitation

Yellowstone's unique geographic setting creates orographic precipitation on the plateau. Moisture from the Pacific Ocean is funneled east along the low-elevation Snake River Plain and is forced to ascend by the topographic barrier of the Yellowstone Plateau, causing storms to release significant amounts of precipitation throughout the park (Licciardi and Pierce, 2018). At present, a majority of the park's annual precipitation falls as snow and its hydrologic regimes are dominated by a pulse of moisture in the spring from the melting snowpack (Gardner et al., 2010). Throughout the summer, generally dry conditions are punctuated by intense thunderstorms (Hostetler et al., 2021).

1.6.5. Earthquakes

Yellowstone is one of the most seismically active regions in the United States (Figure 1.5B). Swarms of mostly low-magnitude earthquakes occur throughout the park periodically and are thought to be related to the subsurface movement of magma and hydrothermal fluids due to the influence of the hotspot (Shelly et al., 2013). Yellowstone also lies at the edge of the Basin and Range tectonic province; the hotspot and subsequent volcanic activity is thought to have buried much of that topography and possibly large faults (Christiansen, 2001; Thigpen et al., 2021). Outside of the park, Basin and Range faults are associated with some of the largest earthquakes in western United States. Notably, the Hebgen Lake earthquake in 1959 triggered

widespread landslide activity both by triggering new landslides and reactivating old ones (Hadley, 1964). The Teton Fault is located just south of Yellowstone National Park; paleoseismic evidence suggests that the fault has experienced at least three surface-rupturing earthquake events with estimated M_{ws} of 6.6-7.2 since the retreat of the Pinedale ice sheet (Zellman et al., 2020).

1.6.6. Climate Change Predictions

By 2100, the Greater Yellowstone Ecosystem (GYE) is predicted to see at least a 3°C increase in annual temperatures, a 9% increase in precipitation, and a 40% reduction in snowpack (Hostetler et al., 2021). As the GYE experiences a higher amount of precipitation, more of that precipitation will also be falling as rain instead of snow. With links between intense precipitation events and landslides (e.g., Handwerger et al., 2022), Yellowstone may be subject to increased landslide hazard and will be an ideal location to study landscape (and other) effects of climate change. Without a robust baseline inventory or current conditions however, it will be challenging to quantify those effects and to make future predictions.

1.6.7. Visitors and Park Infrastructure

Yellowstone hosts millions of visitors annually on ~500 km of paved roads (<https://www.nps.gov/yell/planyourvisit/parkfacts.htm>). These narrow, winding roads often traverse steep, landslide-prone terrain and, without a comprehensive landslide inventory of the park, infrastructure managers are unable to fully characterize and plan for risks to those roads. A massive rain-on-snow event in June 2022 caused widespread flooding and associated erosion throughout the northern half of the park resulting in millions of dollars' worth of damage to park

infrastructure (<https://www.nps.gov/yell/planyourvisit/flood-recovery.htm>). This extreme weather event highlighted a need in the park for infrastructure to be well-adapted to natural hazards; a robust understanding of where those hazards occur and what they are is essential to preparing for them. With no modern landslide inventory of the park, it is not currently possible to fully characterize landslides hazards in Yellowstone.

1.6.8. Previous Landslide Mapping

The USGS carried out an ambitious mapping project of Yellowstone National Park in the 1970s, resulting in a series of professional papers and 1:62,500-scale maps of bedrock and surficial geology (Ruppel, 1972; Smedes and Prostka, 1972; Pierce, 1973; Love and Keefer, 1975). All of these maps and reports mention landslides, but landslides are not treated in a systematic manner in any of the reports and the mappers do not generally distinguish types of movements or make connections between different areas of the park. Multiple studies have focused on a specific cluster of landslides just north of Mammoth Hot Springs near the north entrance to the park (Waldrop and Hyden, 1962; Nicholas, 2018) but do not examine the broader-scale distribution of landslides throughout the region.

Throughout the 1980s, the Wyoming State Geological Survey used aerial photographs to compile a landslide inventory for the entire state at a 1:24,000 scale (Case, 1990). The inventory outlines landslide features and assigns them a type. The inventory claims to follow the Cruden and Varnes classification scheme but contains many types of features that do not fall into the classification, including colluvium, slopewash, and solifluction. Within Yellowstone National Park, the Case (1990) inventory identifies ~1300 landslide features, and ~400 of those are not typical mass movement features. New LiDAR data presents an opportunity to update this

inventory, collect lithologic and topographic attributes that may better inform a hazard analysis and to create a product that may be better integrated into a national data set.

To our knowledge, InSAR has not been applied to academic studies of landslides in Yellowstone. InSAR has previously been used extensively to study volcanic deformation in the park (e.g., Chang et al., 2007; Tizzani et al., 2015; Kelevitz et al., 2021) so we know that there is SAR coverage of the area and that it is possible to measure ground deformation despite complications posed by atmospheric or vegetation effects.

1.7. Conclusion

Our work within this thesis builds on previous landslide mapping efforts through the use of finer-resolution LiDAR data to map landslide deposits throughout the entirety of Yellowstone National Park at a 1:4000 scale and characterize the movement style and lithologic characteristics of those deposits. We use InSAR-derived displacement and velocity estimates to identify actively creeping landslide deposits and to examine the movement patterns of selected active landslides.

This thesis is organized into four chapters. This chapter is the introduction that provides context for the following chapters. Chapter Two concerns the LiDAR-based landslide inventory for all of Yellowstone National Park. Chapter Three concerns InSAR time series analysis of Yellowstone and the creation of a velocity inventory and the time series analysis of selected landslides. Chapters Two and Three are formatted to be stand-alone papers for submission to peer-reviewed journals. Consequently, there is some redundancy between the first three chapters. Chapter Four offers concluding remarks for the entire project, including suggestions for future work.

1.8. Figures

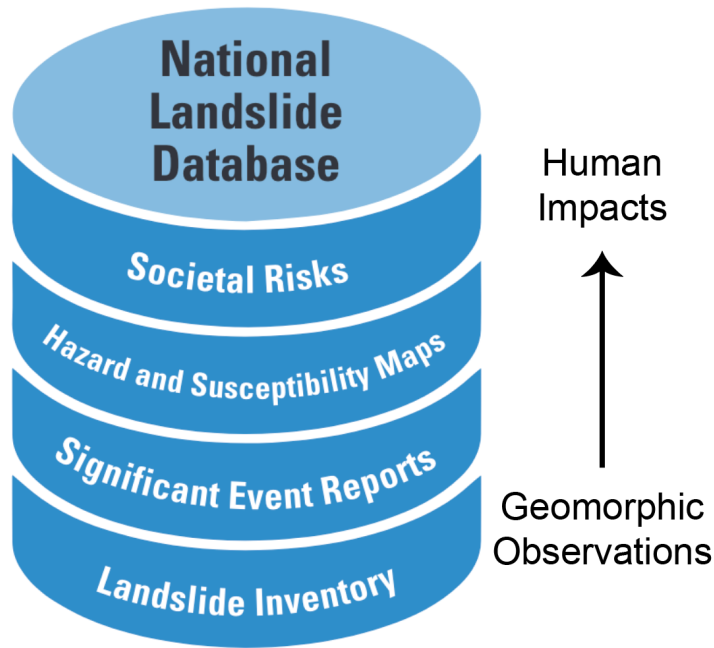


Figure 1.1. Proposed structure of a national landslide database for the United States (modified from Godt et al., 2022). Landslide inventories form the foundation of assessments of landslide hazard and risk and including susceptibility maps, early warning systems, response plans and preparedness protocols.

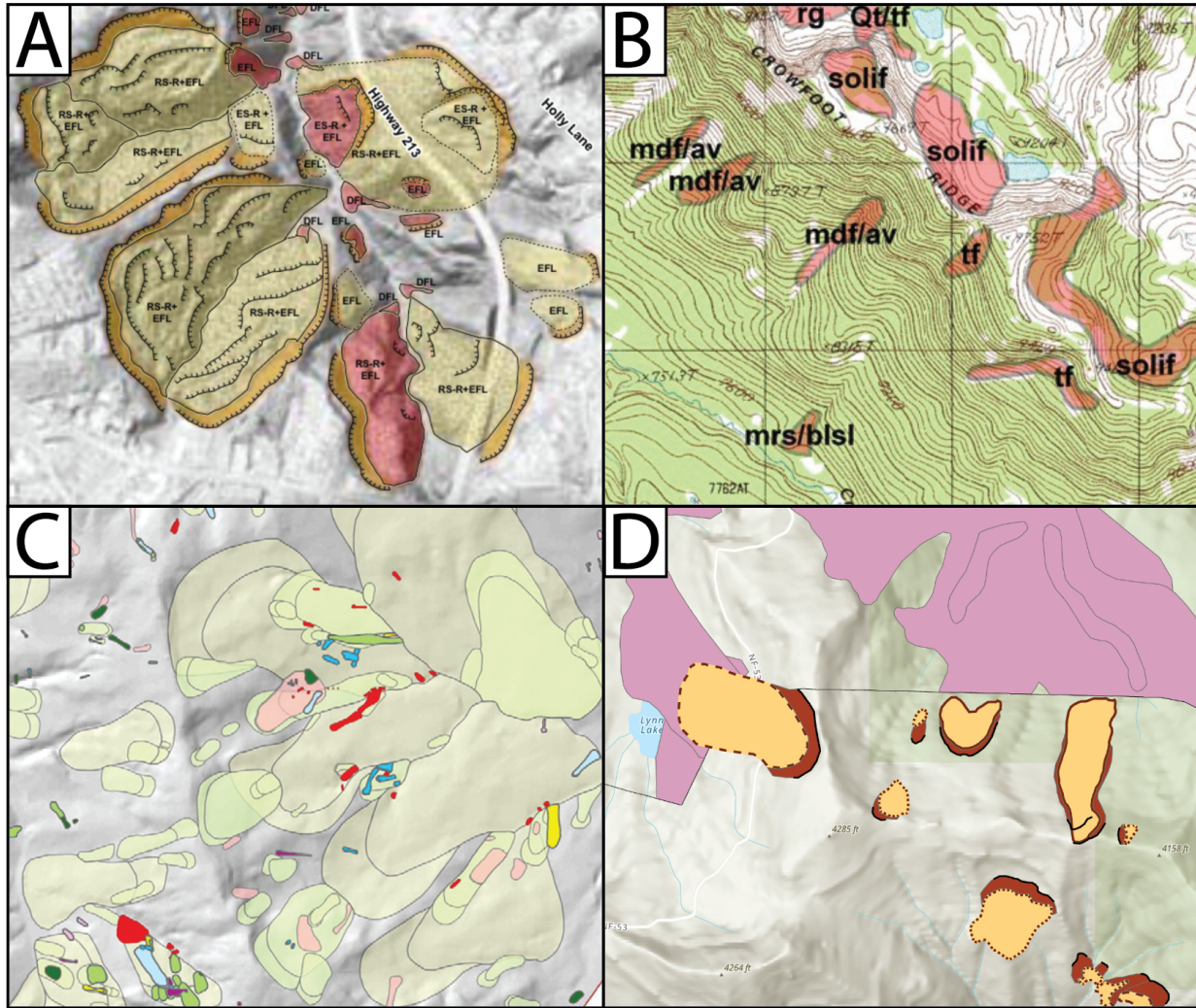


Figure 1.2. Details of selected landslide inventories. A) From Burns and Madin (2009), an inventory near Oregon City, Oregon based on LiDAR and aerial photo interpretation and compilation of older landslide observations. This inventory outlines deposits, head scarps, and internal scarps and defines landslide type over a LiDAR-derived hillshade map. Deposits are colored by estimated ages: red indicates deposits that are less than 150 years old; yellow are older. B) From Case (1990), a detail of the Wyoming state landslide inventory. This inventory outlines features attributed to landslides and was compiled through interpretation of stereo aerial photos. Each polygon is assigned a type or multiple types. The polygons are displayed over a USGS 7.5-minute Quadrangle. C) From Guzzetti et al. (2012), a detail from a multi-temporal inventory of Umbria, Italy. This inventory outlines landslide deposits and crowns and colors them by age. This map was produced through repeated aerial imagery surveys over a period of 50 years. D) From <https://geologyportal.dnr.wa.gov/>, a web-map compilation of multiple landslide inventories in Washington state. Pink and yellow polygons come from different data sources and display different attributes. The pink polygons are compiled from geologic maps and the yellow from targeted landslide mapping by the Washington Geological Survey. The yellow inventory distinguishes upper and internal scarps and uses dashed, dotted, and solid lines as a confidence indication.

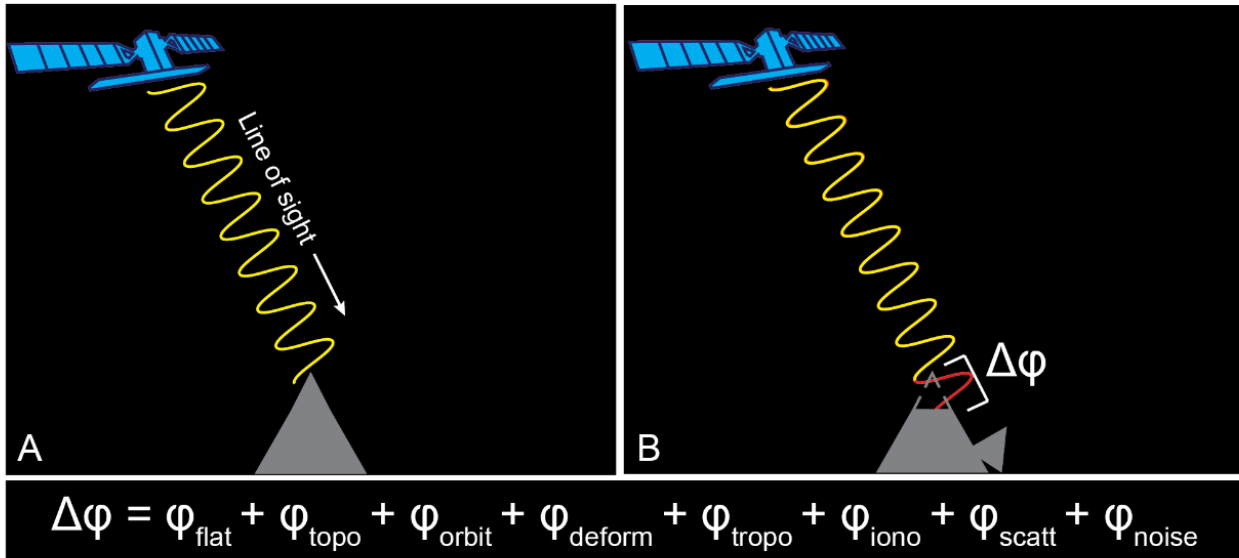


Figure 1.3. Schematic diagram showing InSAR displacement measurement. As a SAR satellite flies over the Earth, it reads the microwave signal reflected by the earth’s surface (A). When the satellite returns (B), the satellite will detect a change in phase, which it can measure very precisely. The measured phase change, $\Delta\phi$, includes ground surface deformation (pictured), a flat earth assumption, topography, differences in satellite orbits, interference from the troposphere and ionosphere, scattering properties of the ground, and inherent radar noise. The flat earth, topography, and orbit phases are removed during interferogram formation. The scatterer and noise phases are typically assumed to be negligible compared to the deformation phase, especially if the region of interest has good coherence (Osmanoğlu et al., 2016).

Satellite Name	Lifetime	Wavelength	Minimum Repeat Time	Notes
Seasat*	1978	L-band	??	*Seasat failed after 105 days
ERS-1	1991-2001	C-band	35 days	
ERS-2	1995-2011	C-band	35 days	
SIR-C	1994	L, X, and C-band	1 day, 6 months	
ENVISAT	2002-2012	C-band	30-35 days	
ALOS-1	2006-2011	L-band	46 days	
ALOS-2 PALSAR	2014-present	L-band	14 days	
Radarsat-1	1995-2013	C-band	24 days	
Radarsat-2	2007-present	C-band	24 days	
TerraSAR-X	2007-2012	X-band	11 days	
COSMO-SkyMed	2007-present	X-band	16 days	
Sentinel-1	2014-present	C-band	12 days	(Data used in this thesis)
NISAR	planned 2024	L-band	12 days	
UAVSAR**	2008-present	L-band, others	as needed	**UAVSAR is an airborne sensor that NASA uses for targeted applications

Table 1.1. List of SAR satellites compiled from earthdata.nasa.gov and uavsar.jpl.nasa.gov, noting operational periods and wavelengths. X-band has a wavelength of 3.5 cm, C-band has a wavelength of 5.6 cm, and L-band has a wavelength of 24.6 cm. Interferometry can measure approximately one-half of a wavelength of change per pixel.

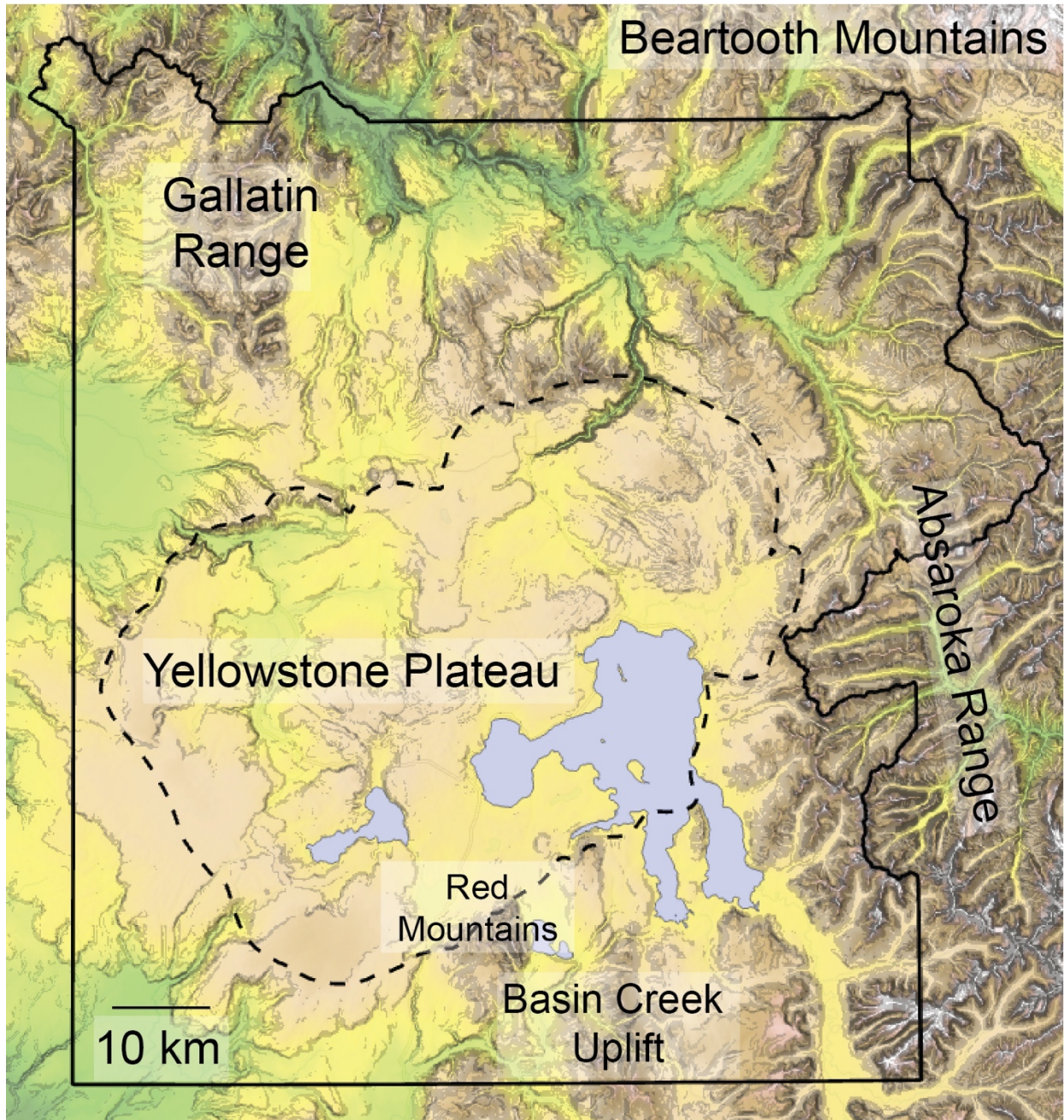


Figure 1.4. Elevation and slope map derived from a 30-m DEM of Yellowstone National Park (park boundary shown with solid black polygon). Darker shading indicates steeper slopes and lower elevations are green and higher elevations are brown to white. Dashed polygon indicates the outline of the collapsed 0.63 Ma caldera, which broadly defines a boundary between the low-relief Yellowstone Plateau in the center of the park and the steep, highly dissected Gallatin, Beartooth, and Absaroka mountains to the north and east.

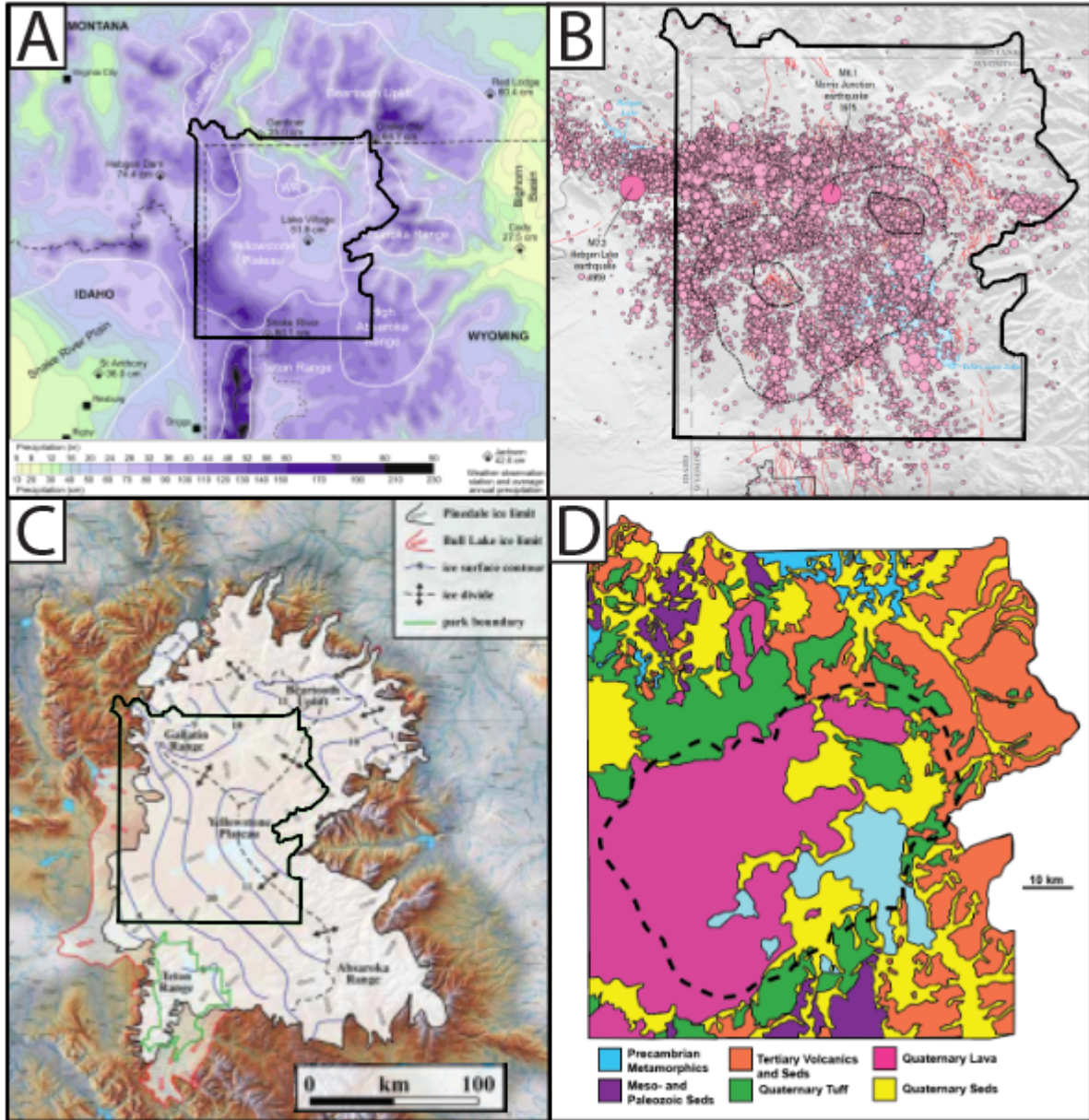


Figure 1.5. Potential factors contributing to landslide activity in Yellowstone. Note the park boundary for scale in all four maps. A) Precipitation map of the Yellowstone region, adapted from Licciardi and Pierce, (2018). B) All recorded earthquakes in the Yellowstone region 1972-2017, adapted from Morgan et al. (2017). C) Map of greatest extent of Pinedale and Bull Lake ice caps adapted from Licciardi and Pierce (2018). D) Simplified bedrock geology map of Yellowstone National Park, adapted from USGS (1972)

1.9. References

- Amelung, F., Galloway, D.L., Bell, J.W., Zebker, H.A., and Laczniak, R.J., 1999, Sensing the ups and downs of Las Vegas: InSAR reveals structural control of land subsidence and aquifer-system deformation: *Geology*, v. 27, p. 483–486, doi:10.1130/0091-7613(1999)027<0483:STUADO>2.3.CO;2.
- Anderson, R.S., Anderson, L.S., Armstrong, W.H., Rossi, M.W., and Crump, S.E., 2018, Glaciation of alpine valleys: The glacier – debris-covered glacier – rock glacier continuum: *Geomorphology*, v. 311, p. 127–142, doi:10.1016/j.geomorph.2018.03.015.
- Aslan, G., Fouvelis, M., Raucoules, D., De Michele, M., Bernardie, S., and Cakir, Z., 2020, Landslide Mapping and Monitoring Using Persistent Scatterer Interferometry (PSI) Technique in the French Alps: *Remote Sensing*, v. 12, p. 1305, doi:10.3390/rs12081305.
- Atwood, D., Meyer, F., and Arendt, A., 2010, Using L-band SAR coherence to delineate glacier extent: *Canadian Journal of Remote Sensing*, v. 36, p. 186, doi:10.5589/m10-014.
- Ballantyne, C.K., 2002, Paraglacial geomorphology: *Quaternary Science Reviews*, v. 21, p. 1935–2017.
- Barboux, C., Delaloye, R., and Lambiel, C., 2014, Inventorying slope movements in an Alpine environment using InSAR: *Earth Surface Processes and Landforms*, v. 39, p. 2087–2099, doi:10.1002/esp.3603.
- Bekaert, D.P.S., Handwerger, A.L., Agram, P., and Kirschbaum, D.B., 2020, InSAR-based detection method for mapping and monitoring slow-moving landslides in remote regions with steep and mountainous terrain: An application to Nepal: *Remote Sensing of Environment*, v. 249, p. 111983, doi:10.1016/j.rse.2020.111983.

- Bennett, G.L., Miller, S.R., Roering, J.J., and Schmidt, D.A., 2016, Landslides, threshold slopes, and the survival of relict terrain in the wake of the Mendocino Triple Junction: *Geology*, v. 44, p. 363–366, doi:10.1130/G37530.1.
- Berardino, P., Fornaro, G., Lanari, R., and Sansosti, E., 2002, A new algorithm for surface deformation monitoring based on small baseline differential SAR interferograms: *IEEE Transactions on Geoscience and Remote Sensing*, v. 40, p. 2375–2383, doi:10.1109/TGRS.2002.803792.
- Blahut, J., van Westen, C.J., and Sterlacchini, S., 2010, Analysis of landslide inventories for accurate prediction of debris-flow source areas: *Geomorphology*, v. 119, p. 36–51, doi:10.1016/j.geomorph.2010.02.017.
- Booth, A.M., Roering, J.J., and Perron, J.T., 2009, Automated landslide mapping using spectral analysis and high-resolution topographic data: Puget Sound lowlands, Washington, and Portland Hills, Oregon: *Geomorphology*, v. 109, p. 132–147, doi:10.1016/j.geomorph.2009.02.027.
- Borgatti, L., and Soldati, M., 2010, Landslides as a geomorphological proxy for climate change: A record from the Dolomites (northern Italy): *Geomorphology*, v. 120, p. 56–64, doi:10.1016/j.geomorph.2009.09.015.
- Brencher, G., Handwerger, A.L., and Munroe, J.S., 2021, InSAR-based characterization of rock glacier movement in the Uinta Mountains, Utah, USA: *The Cryosphere*, v. 15, p. 4823–4844, doi:10.5194/tc-15-4823-2021.
- Bunn, M., Leshchinsky, B., Olsen, M., and Booth, A., 2019, A Simplified, Object-Based Framework for Efficient Landslide Inventorying Using LIDAR Digital Elevation Model Derivatives: *Remote Sensing*, v. 11, p. 303, doi:10.3390/rs11030303.

- Burns, W.J., and Madin, I.P., 2009, Protocol for Inventory Mapping of Landslide Deposits from Light Detection and Ranging (lidar) Imagery: Oregon Department of Geology and Mineral Industries Special Paper 42, 36 p.
- Cafiso, F., and Cappadonia, C., 2019, Landslide inventory and rockfall risk assessment of a strategic urban area (Palermo, Sicily): *Rendiconti Online della Società Geologica Italiana*, v. 48, p. 96–105, doi:10.3301/ROL.2019.42.
- Calabro, M.D., Schmidt, D.A., and Roering, J.J., 2010, An examination of seasonal deformation at the Portuguese Bend landslide, southern California, using radar interferometry: *Journal of Geophysical Research: Earth Surface*, v. 115, doi:10.1029/2009JF001314.
- Camp, V., and Wells, R., 2021, The Case for a Long-Lived and Robust Yellowstone Hotspot: *GSA Today*, v. 31, p. 4–10, doi:10.1130/GSATG477A.1.
- Cardinali, M., Guzzetti, F., and Brabb, E.E., 1990, Preliminary maps showing landslide deposits and related features in New Mexico: U.S. Geological Survey 90–293, doi:10.3133/ofr90293.
- Carson, M.A., and Kirkby, M.J., 1972, *Hillslope Form and Process*: London, Cambridge University Press, 475 p.
- Case, J.C., 1990, Preliminary Landslide Maps: Wyoming State Geological Survey, <http://www.wrds.uwyo.edu/wrds/wsgs/hazards/landslides/lshome.html> (accessed April 2023).
- Chang, W.-L., Smith, R.B., Wicks, C., Farrell, J.M., and Puskas, C.M., 2007, Accelerated Uplift and Magmatic Intrusion of the Yellowstone Caldera, 2004 to 2006: *Science*, v. 318, p. 952–956, doi:10.1126/science.1146842.

- Chaussard, E., Havazli, E., Fattahi, H., Cabral-Cano, E., and Solano-Rojas, D., 2021, Over a Century of Sinking in Mexico City: No Hope for Significant Elevation and Storage Capacity Recovery: *Journal of Geophysical Research: Solid Earth*, v. 126, p. e2020JB020648, doi:10.1029/2020JB020648.
- Chleborad, A.F., 1998, Use of Air Temperature Data to Anticipate the Onset of Snowmelt-Season Landslides: U.S. Geological Survey Open-File Report 98-124, 16 p., <https://pubs.usgs.gov/of/1998/0124/report.pdf> (accessed April 2023).
- Christiansen, R.L., 2001, The Quaternary and Pliocene Yellowstone Plateau Volcanic Field of Wyoming, Idaho, and Montana: Washington, United States Government Printing Office, *Geology of Yellowstone National Park G*, 145 p.
- Christiansen, R.L., Foulger, G.R., and Evans, J.R., 2002, Upper-mantle origin of the Yellowstone hotspot: *Geological Society of America Bulletin*, v. 114, p. 1245–1256, doi:10.1130/0016-7606(2002)114<1245:UMOOTY>2.0.CO;2.
- Coe, J.A., Ellis, W.L., Godt, J.W., Savage, W.Z., Savage, J.E., Michael, J.A., Kibler, J.D., Powers, P.S., Lidke, D.J., and Debray, S., 2003, Seasonal movement of the Slumgullion landslide determined from Global Positioning System surveys and field instrumentation, July 1998–March 2002: *Engineering Geology*, v. 68, p. 67–101, doi:10.1016/S0013-7952(02)00199-0.
- Coe, J.A., Kean, J.W., Godt, J.W., Baum, R.L., Jones, E.S., Gochis, D.J., and Anderson, G.S., 2014, New insights into debris-flow hazards from an extraordinary event in the Colorado Front Range: *GSA Today*, v. 24, p. 4–10, doi:10.1130/GSATG214A.1.

- Cook, M.E., Brook, M.S., Hamling, I.J., Cave, M., Tunnicliffe, J.F., Holley, R., and Alama, D.J., 2022, Engineering geomorphological and InSAR investigation of an urban landslide, Gisborne, New Zealand: *Landslides*, v. 19, p. 2423–2437, doi:10.1007/s10346-022-01938-z.
- Cossart, E., Mercier, D., Decaulne, A., Feuillet, T., Jónsson, H.P., and Sæmundsson, Þ., 2014, Impacts of post-glacial rebound on landslide spatial distribution at a regional scale in northern Iceland (Skagafjörður): *Earth Surface Processes and Landforms*, v. 39, p. 336–350, doi:10.1002/esp.3450.
- Crosby, B., and Bornong, K., 2022, Yellowstone exposed! New elevation map reveals park’s complex geologic history | U.S. Geological Survey: *Yellowstone Caldera Chronicles*, <https://www.usgs.gov/observatories/yvo/news/yellowstone-exposed-new-elevation-map-reveals-parks-complex-geologic-history> (accessed April 2023).
- Crosetto, M., Monserrat, O., Cuevas-González, M., Devanthéry, N., and Crippa, B., 2016, Persistent Scatterer Interferometry: A review: *ISPRS Journal of Photogrammetry and Remote Sensing*, v. 115, p. 78–89, doi:10.1016/j.isprsjprs.2015.10.011.
- Crozier, M.J., 2010, Deciphering the effect of climate change on landslide activity: A review: *Geomorphology*, v. 124, p. 260–267, doi:10.1016/j.geomorph.2010.04.009.
- Cruden, D.M., and Varnes, D.J., 1996, *Landslide Types and Processes*, in Turner, A.K. and Shuster, R.L. eds., *Landslides: Investigation and Mitigation*, Transportation Research Special Report 247, p. 36–75.
- DeGraff, J.V., Cannon, S.H., and Gartner, J.E., 2015, The Timing of Susceptibility to Post-Fire Debris Flows in the Western United States: *Environmental & Engineering Geoscience*, v. 21, p. 277–292, doi:10.2113/gseegeosci.21.4.277.

- Delbridge, B.G., Bürgmann, R., Fielding, E., Hensley, S., and Schulz, W.H., 2016, Three-dimensional surface deformation derived from airborne interferometric UAVSAR: Application to the Slumgullion Landslide: UAVSAR-DERIVED 3-D SURFACE DEFORMATION: *Journal of Geophysical Research: Solid Earth*, v. 121, p. 3951–3977, doi:10.1002/2015JB012559.
- Engram, M., Arp, C.D., Jones, B.M., Ajadi, O.A., and Meyer, F.J., 2018, Analyzing floating and bedfast lake ice regimes across Arctic Alaska using 25 years of space-borne SAR imagery: *Remote Sensing of Environment*, v. 209, p. 660–676, doi:10.1016/j.rse.2018.02.022.
- Ferretti, A., Monti-Guarnieri, A., Prati, C., Rocca, F., and Massonnet, D., 2007, *InSar Principles - Guidelines for SAR Interferometry Processing and Interpretation: European Space Agency TM-19*.
- Ferretti, A., Prati, C., and Rocca, F., 2001, Permanent scatterers in SAR interferometry: *IEEE Transactions on Geoscience and Remote Sensing*, v. 39, p. 8–20, doi:10.1109/36.898661.
- Fielding, E.J., Blom, R.G., and Goldstein, R.M., 1998, Rapid subsidence over oil fields measured by SAR interferometry: *Geophysical Research Letters*, v. 25, p. 3215–3218, doi:10.1029/98GL52260.
- Froude, M.J., and Petley, D.N., 2018, Global fatal landslide occurrence from 2004 to 2016: *Natural Hazards and Earth System Sciences*, v. 18, p. 2161–2181, doi:10.5194/nhess-18-2161-2018.
- Funning, G.J., Bürgmann, R., Ferretti, A., Novali, F., and Fumagalli, A., 2007, Creep on the Rodgers Creek fault, northern San Francisco Bay area from a 10 year PS-InSAR dataset: *Geophysical Research Letters*, v. 34, doi:10.1029/2007GL030836.

- Funning, G.J., Parsons, B., Wright, T.J., Jackson, J.A., and Fielding, E.J., 2005, Surface displacements and source parameters of the 2003 Bam (Iran) earthquake from Envisat advanced synthetic aperture radar imagery: *Journal of Geophysical Research: Solid Earth*, v. 110, doi:10.1029/2004JB003338.
- Gabriel, A.K., Goldstein, R.M., and Zebker, H.A., 1989, Mapping small elevation changes over large areas: Differential radar interferometry: *Journal of Geophysical Research*, v. 94, p. 9183, doi:10.1029/JB094iB07p09183.
- Gardner, W.P., Susong, D.D., Solomon, D.K., and Heasler, H., 2010, Snowmelt hydrograph interpretation: Revealing watershed scale hydrologic characteristics of the Yellowstone volcanic plateau: *Journal of Hydrology*, v. 383, p. 209–222, doi:10.1016/j.jhydrol.2009.12.037.
- Gariano, S.L., and Guzzetti, F., 2016, Landslides in a changing climate: *Earth-Science Reviews*, v. 162, p. 227–252, doi:10.1016/j.earscirev.2016.08.011.
- Godt, J.W., Wood, N.J., Pennaz, A.B., Dacey, C.M., Mirus, B.B., Schaefer, L.N., and Slaughter, S.L., 2022, National Strategy for Landslide Loss Reduction: United States Geological Survey Open-File Report Open-File Report 2022–1075, 36 p.
- Guzzetti, F., Manunta, M., Ardizzone, F., Pepe, A., Cardinali, M., Zeni, G., Reichenbach, P., and Lanari, R., 2009, Analysis of Ground Deformation Detected Using the SBAS-InSAR Technique in Umbria, Central Italy: *Pure and Applied Geophysics*, v. 166, p. 1425–1459, doi:10.1007/s00024-009-0491-4.
- Guzzetti, F., Mondini, A.C., Cardinali, M., Fiorucci, F., Santangelo, M., and Chang, K.-T., 2012, Landslide inventory maps: New tools for an old problem: *Earth-Science Reviews*, v. 112, p. 42–66, doi:10.1016/j.earscirev.2012.02.001.

- Hadley, J.D., 1964, Landslides and related phenomena accompanying the Hebgen Lake earthquake of August 17, 1959: U.S. Geological Survey Professional Paper 435-K.
- Hamilton, S.J., and Whalley, W.B., 1995, Rock glacier nomenclature: A re-assessment: *Geomorphology*, v. 14, p. 73–80, doi:10.1016/0169-555X(95)00036-5.
- Hamling, I.J. et al., 2017, Complex multifault rupture during the 2016 Mw 7.8 Kaikōura earthquake, New Zealand: *Science*, v. 356, p. eaam7194, doi:10.1126/science.aam7194.
- Handwerger, A.L., Fielding, E.J., Huang, M., Bennett, G.L., Liang, C., and Schulz, W.H., 2019a, Widespread Initiation, Reactivation, and Acceleration of Landslides in the Northern California Coast Ranges due to Extreme Rainfall: *Journal of Geophysical Research: Earth Surface*, v. 124, p. 1782–1797, doi:10.1029/2019JF005035.
- Handwerger, A.L., Fielding, E.J., Sangha, S.S., and Bekaert, D.P.S., 2022, Landslide Sensitivity and Response to Precipitation Changes in Wet and Dry Climates: *Geophysical Research Letters*, v. 49, p. e2022GL099499, doi:10.1029/2022GL099499.
- Handwerger, A.L., Huang, M.-H., Fielding, E.J., Booth, A.M., and Bürgmann, R., 2019b, A shift from drought to extreme rainfall drives a stable landslide to catastrophic failure: *Scientific Reports*, v. 9, p. 1569, doi:10.1038/s41598-018-38300-0.
- Handwerger, A.L., Roering, J.J., Schmidt, D.A., and Rempel, A.W., 2015, Kinematics of earthflows in the Northern California Coast Ranges using satellite interferometry: *Geomorphology*, v. 246, p. 321–333, doi:10.1016/j.geomorph.2015.06.003.
- Highland, L.M., and Bobrowsky, P., 2008, *The Landslide Handbook- A Guide to Understanding Landslides*: United States Geological Survey Circular Circular 1325, 129 p.

- Hogenson, K. et al., 2020, Hybrid Pluggable Processing Pipeline (HyP3): A cloud-native infrastructure for generic processing of SAR data:, <https://doi.org/10.5281/zenodo.4646138>.
- Holm, K., Bovis, M., and Jakob, M., 2004, The landslide response of alpine basins to post-Little Ice Age glacial thinning and retreat in southwestern British Columbia: *Geomorphology*, v. 57, p. 201–216, doi:10.1016/S0169-555X(03)00103-X.
- Hostetler, S. et al., 2021, Greater Yellowstone climate assessment: past, present, and future climate change in greater Yellowstone watersheds: Montana State University, doi:10.15788/GYCA2021.
- Hu, X., and Bürgmann, R., 2020, Rheology of a Debris Slide From the Joint Analysis of UAVSAR and LiDAR Data: *Geophysical Research Letters*, v. 47, doi:10.1029/2020GL087452.
- Huggel, C., Clague, J.J., and Korup, O., 2012, Is climate change responsible for changing landslide activity in high mountains?: CLIMATE CHANGE AND LANDSLIDES IN HIGH MOUNTAINS: *Earth Surface Processes and Landforms*, v. 37, p. 77–91, doi:10.1002/esp.2223.
- Hungr, O., Leroueil, S., and Picarelli, L., 2014, The Varnes classification of landslide types, an update: *Landslides*, v. 11, p. 167–194, doi:10.1007/s10346-013-0436-y.
- Hungr, O., McDougall, S., Wise, M., and Cullen, M., 2008, Magnitude–frequency relationships of debris flows and debris avalanches in relation to slope relief: *Geomorphology*, v. 96, p. 355–365, doi:10.1016/j.geomorph.2007.03.020.

- Iwahana, G., Uchida, M., Liu, L., Gong, W., Meyer, F.J., Guritz, R., Yamanokuchi, T., and Hinzman, L., 2016, InSAR Detection and Field Evidence for Thermokarst after a Tundra Wildfire, Using ALOS-PALSAR: *Remote Sensing*, v. 8, p. 218, doi:10.3390/rs8030218.
- Jia, G. et al., 2019, Land-Climate Interactions, *in* Shukla, P.R. et al. eds., *Climate Change and Land: an IPCC special report on climate change, desertification, land degradation, sustainable land management, food security, and greenhouse gas fluxes in terrestrial ecosystems*, <https://doi.org/10.1017/9781009157988.004>.
- Jolivet, R., Agram, P.S., Lin, N.Y., Simons, M., Doin, M.-P., Peltzer, G., and Li, Z., 2014, Improving InSAR geodesy using Global Atmospheric Models: *Journal of Geophysical Research: Solid Earth*, v. 119, p. 2324–2341, doi:10.1002/2013JB010588.
- Jones, J.N., Boulton, S.J., Bennett, G.L., Stokes, M., and Whitworth, M.R.Z., 2021, Temporal Variations in Landslide Distributions Following Extreme Events: Implications for Landslide Susceptibility Modeling: *Journal of Geophysical Research: Earth Surface*, v. 126, doi:10.1029/2021JF006067.
- Keefer, D., K., 1984, Landslides caused by earthquakes: *GSA Bulletin*, v. 95, p. 406–421, doi:10.1130/0016-7606(1984)95<406:LCBE>2.0.CO;2.
- Kelevitz, K., Tiampo, K.F., and Corsa, B.D., 2021, Improved Real-Time Natural Hazard Monitoring Using Automated InSAR Time Series: *Remote Sensing*, v. 13, p. 867, doi:10.3390/rs13050867.
- Klose, M., Maurischat, P., and Damm, B., 2016, Landslide impacts in Germany: A historical and socioeconomic perspective: *Landslides*, v. 13, p. 183–199, doi:10.1007/s10346-015-0643-9.

- Korup, O., 2008, Rock type leaves topographic signature in landslide-dominated mountain ranges: *Geophysical Research Letters*, v. 35, doi:10.1029/2008GL034157.
- Lauknes, T.R., Piyush Shanker, A., Dehls, J.F., Zebker, H.A., Henderson, I.H.C., and Larsen, Y., 2010, Detailed rockslide mapping in northern Norway with small baseline and persistent scatterer interferometric SAR time series methods: *Remote Sensing of Environment*, v. 114, p. 2097–2109, doi:10.1016/j.rse.2010.04.015.
- Licciardi, J., Hurwitz, S., and Harrison, L., 2022, The Last Deglaciation of the Yellowstone Plateau: Timing and Implications: *Geological Society of America Abstracts with Programs*, v. 54, doi:10.1130/abs/2022AM-381490.
- Licciardi, J.M., and Pierce, K.L., 2018, History and dynamics of the Greater Yellowstone Glacial System during the last two glaciations: *Quaternary Science Reviews*, v. 200, p. 1–33, doi:10.1016/j.quascirev.2018.08.027.
- Lingbloom, J., 2022, A Landslide Inventory and Analysis for Grand Teton National Park, Wyoming [MS Thesis]: Idaho State University, 95 p.
- Liu, L., Millar, C.I., Westfall, R.D., and Zebker, H.A., 2013, Surface motion of active rock glaciers in the Sierra Nevada, California, USA: inventory and a case study using InSAR: *The Cryosphere*, v. 7, p. 1109–1119, doi:10.5194/tc-7-1109-2013.
- Liu, L., Zhang, T., and Wahr, J., 2010, InSAR measurements of surface deformation over permafrost on the North Slope of Alaska: *Journal of Geophysical Research: Earth Surface*, v. 115, doi:10.1029/2009JF001547.
- Love, J.D., and Keefer, W.R., 1975, Geology of sedimentary rocks in southern Yellowstone National Park, Wyoming: U.S. Geological Survey Professional Paper 729-D, <https://pubs.er.usgs.gov/publication/pp729D> (accessed March 2023).

- Mackey, B.H., and Roering, J.J., 2011, Sediment yield, spatial characteristics, and the long-term evolution of active earthflows determined from airborne LiDAR and historical aerial photographs, Eel River, California: *Geological Society of America Bulletin*, p. 17.
- Malamud, B.D., Turcotte, D.L., Guzzetti, F., and Reichenbach, P., 2004, Landslide inventories and their statistical properties: *Earth Surface Processes and Landforms*, v. 29, p. 687–711, doi:10.1002/esp.1064.
- Mantovani, M., Bossi, G., Marcato, G., Schenato, L., Tedesco, G., Titti, G., and Pasuto, A., 2019, New Perspectives in Landslide Displacement Detection Using Sentinel-1 Datasets: *Remote Sensing*, v. 11, p. 2135, doi:10.3390/rs11182135.
- Marc, O., Gosset, M., Saito, H., Uchida, T., and Malet, J.-P., 2019, Spatial Patterns of Storm-Induced Landslides and Their Relation to Rainfall Anomaly Maps: *Geophysical Research Letters*, v. 46, p. 11167–11177, doi:10.1029/2019GL083173.
- Marshall, S.T., Funning, G.J., and Owen, S.E., 2013, Fault slip rates and interseismic deformation in the western Transverse Ranges, California: *Journal of Geophysical Research: Solid Earth*, v. 118, p. 4511–4534, doi:10.1002/jgrb.50312.
- Massonnet, D., and Feigl, K.L., 1998, Radar interferometry and its application to changes in the Earth's surface: *Reviews of Geophysics*, v. 36, p. 441–500, doi:10.1029/97RG03139.
- Meyer, F., 2019, Spaceborne synthetic aperture radar-Principles, data access, and basic processing techniques, *in* Flores, A., Herndon, K., Thapa, R., and Cherrington, E. eds., *SAR Handbook: Comprehensive Methodologies for Forest Monitoring and Biomass Estimation*, NASA, doi:10.25966/ez4f-mg98.

- Meyer, F.J., Mahoney, A.R., Eicken, H., Denny, C.L., Druckenmiller, H.C., and Hendricks, S., 2011, Mapping arctic landfast ice extent using L-band synthetic aperture radar interferometry: *Remote Sensing of Environment*, v. 115, p. 3029–3043, doi:10.1016/j.rse.2011.06.006.
- Mirus, B.B. et al., 2020, Landslides across the USA: occurrence, susceptibility, and data limitations: *Landslides*, v. 17, p. 2271–2285, doi:10.1007/s10346-020-01424-4.
- Montgomery, D.R., Schmidt, K.M., Greenberg, H.M., and Dietrich, W.E., 2000, Forest clearing and regional landsliding: *Geology*, v. 28, p. 311–314.
- Morgan, L., Shanks, W.C.P., Lowenstern, J., Farrell, J., and Robinson, J., 2017, *Geologic Field-Trip Guide to the Volcanic and Hydrothermal Landscape of the Yellowstone Plateau: U.S. Geological Survey Scientific Investigations Report Scientific Investigations Report 2017-5022-P*.
- Nicholas, G.E., 2018, *Landslide morphology and its insight into the timing and causes of slope failure: Case study of post-glacial landslides in Yellowstone National Park [M.S. Thesis]: Montana State University, 54 p.*
- Nikos, S., Ioannis, P., Constantinos, L., Paraskevas, T., Anastasia, K., and Charalambos (Haris), K., 2016, Land subsidence rebound detected via multi-temporal InSAR and ground truth data in Kalochori and Sindos regions, Northern Greece: *Engineering Geology*, v. 209, p. 175–186, doi:10.1016/j.enggeo.2016.05.017.
- Osmanoğlu, B., Sunar, F., Wdowinski, S., and Cabral-Cano, E., 2016, Time series analysis of InSAR data: Methods and trends: *ISPRS Journal of Photogrammetry and Remote Sensing*, v. 115, p. 90–102, doi:10.1016/j.isprsjprs.2015.10.003.

- Parise, M., and Cannon, S.H., 2012, Wildfire impacts on the processes that generate debris flows in burned watersheds: *Natural Hazards*, v. 61, p. 217–227, doi:10.1007/s11069-011-9769-9.
- Pierce, K.L., 1979, History and dynamics of glaciation in the northern Yellowstone National Park area: Professional Paper, doi:10.3133/pp729F.
- Pierce, K.L., 1973, Surficial geologic map of the Mount Holmes quadrangle and parts of the Tepee Creek, Crown Butte, and Miner quadrangles, Yellowstone National Park, Wyoming and Montana: IMAP Report 640, doi:10.3133/i640.
- Pierce, K.L., and Morgan, L.A., 2009, Is the track of the Yellowstone hotspot driven by a deep mantle plume? — Review of volcanism, faulting, and uplift in light of new data: *Journal of Volcanology and Geothermal Research*, v. 188, p. 1–25, doi:10.1016/j.jvolgeores.2009.07.009.
- Roering, J.J., Kirchner, J.W., and Dietrich, W.E., 2005, Characterizing structural and lithologic controls on deep-seated landsliding: Implications for topographic relief and landscape evolution in the Oregon Coast Range, USA: *Geological Society of America Bulletin*, v. 117, p. 654, doi:10.1130/B25567.1.
- Roering, J.J., Mackey, B.H., Handwerger, A.L., Booth, A.M., Schmidt, D.A., Bennett, G.L., and Cerovski-Darriau, C., 2015, Beyond the angle of repose: A review and synthesis of landslide processes in response to rapid uplift, Eel River, Northern California: *Geomorphology*, v. 236, p. 109–131, doi:10.1016/j.geomorph.2015.02.013.

- Roering, J.J., Mackey, B.H., Marshall, J.A., Sweeney, K.E., Deligne, N.I., Booth, A.M., Handwerger, A.L., and Cerovski-Darriau, C., 2013, 'You are HERE': Connecting the dots with airborne lidar for geomorphic fieldwork: *Geomorphology*, v. 200, p. 172–183, doi:10.1016/j.geomorph.2013.04.009.
- Roering, J.J., Stimely, L.L., Mackey, B.H., and Schmidt, D.A., 2009, Using InSAR, airborne LiDAR, and archival air photos to quantify landsliding and sediment transport: *Geophysical Research Letters*, v. 36, p. L19402, doi:10.1029/2009GL040374.
- Rosen, P.A., Gurrola, E., Sacco G.F., and Zebker, H., 2012, The InSAR scientific computing environment, *in* EUSAR 2012; 9th European Conference on Synthetic Aperture Radar, p. 730–733.
- Rosen, P.A., Hensley, S., Peltzer, G., and Simons, M., 2004, Updated repeat orbit interferometry package released: *Eos, Transactions American Geophysical Union*, v. 85, p. 47–47, doi:10.1029/2004EO050004.
- Rosen, P.A., Hensley, S., Zebker, H.A., Webb, F.H., and Fielding, E.J., 1996, Surface deformation and coherence measurements of Kilauea Volcano, Hawaii, from SIR-C radar interferometry: *Journal of Geophysical Research: Planets*, v. 101, p. 23109–23125, doi:10.1029/96JE01459.
- Rosen, P.A., Kim, Y., Kumar, R., Misra, T., Bhan, R., and Sagi, V.R., 2017, Global persistent SAR sampling with the NASA-ISRO SAR (NISAR) mission, *in* 2017 IEEE Radar Conference (RadarConf), p. 0410–0414, doi:10.1109/RADAR.2017.7944237.
- Ruppel, E.T., 1972, Geology of pre-Tertiary rocks in the northern part of Yellowstone National Park, Wyoming: U.S. Geological Survey Professional Paper USGS Numbered Series 729-A, doi:10.3133/pp729A.

- Sandwell, D., Mellors, R., Tong, X., Wei, M., and Wessel, P., 2011, GMTSAR: An InSAR Processing System Based on Generic Mapping Tools:, <https://escholarship.org/uc/item/8zq2c02m> (accessed May 2023).
- Schlögel, R., Doubre, C., Malet, J.-P., and Masson, F., 2015, Landslide deformation monitoring with ALOS/PALSAR imagery: A D-InSAR geomorphological interpretation method: *Geomorphology*, v. 231, p. 314–330, doi:10.1016/j.geomorph.2014.11.031.
- Schlögl, M., Richter, G., Avian, M., Thaler, T., Heiss, G., Lenz, G., and Fuchs, S., 2019, On the nexus between landslide susceptibility and transport infrastructure – an agent-based approach: *Natural Hazards and Earth System Sciences*, v. 19, p. 201–219, doi:10.5194/nhess-19-201-2019.
- Seneviratne, S.I. et al., 2012, Changes in climate extremes and their impacts on the natural physical environment, *in* Field, C.B. et al. eds., *Managing the Risks of Extreme Events and Disasters to Advance Climate Change Adaptation: A Special Report of Working Groups I and II of the Intergovernmental Panel on Climate Change (IPCC)*, Cambridge [England] ; New York, Cambridge University Press, p. 109–230.
- Shelly, D.R., Hill, D.P., Massin, F., Farrell, J., Smith, R.B., and Taira, T., 2013, A fluid-driven earthquake swarm on the margin of the Yellowstone caldera: *Journal of Geophysical Research: Solid Earth*, v. 118, p. 4872–4886, doi:10.1002/jgrb.50362.
- Šilhán, K., 2020, Tree ring evidence of slope movements preceding catastrophic landslides: *Landslides*, v. 17, p. 615–626, doi:10.1007/s10346-019-01300-w.
- Slaughter, S.L., Mickelson, K.A., Biel, A., and Contreras, T.A., 2017, Protocol for Landslide Inventory Mapping from LiDAR Data in Washington State: *Washington Geological Survey Bulletin 82*, 35 p.

- Smedes, H., and Prostka, H., 1972, Stratigraphic Framework of the Absaroka Volcanic Supergroup in the Yellowstone National Park Region: United States Geological Survey Geological Survey Professional Paper 729–C.
- Solari, L., Del Soldato, M., Raspini, F., Barra, A., Bianchini, S., Confuorto, P., Casagli, N., and Crosetto, M., 2020, Review of Satellite Interferometry for Landslide Detection in Italy: Remote Sensing, v. 12, p. 1351, doi:10.3390/rs12081351.
- Su, X., Zhang, Y., Meng, X., Rehman, M.U., Khalid, Z., and Yue, D., 2022, Updating Inventory, Deformation, and Development Characteristics of Landslides in Hunza Valley, NW Karakoram, Pakistan by SBAS-InSAR: Remote Sensing, v. 14, p. 4907, doi:10.3390/rs14194907.
- Thigpen, R., Brown, S.J., Helfrich, A.L., Hoar, R., McGlue, M., Woolery, E., Guenther, W.R., Swallow, M.L., Dixon, S., and Gallen, S., 2021, Removal of the Northern Paleo-Teton Range along the Yellowstone Hotspot Track (A. Wöfler, Ed.): Lithosphere, v. 2021, p. 1052819, doi:10.2113/2021/1052819.
- Tian, Y., Xu, C., and Yuan, R., 2022, 2.21 - Earthquake-Triggered Landslides, *in* Shroder, J. (Jack) F. ed., Treatise on Geomorphology (Second Edition), Oxford, Academic Press, p. 583–614, doi:10.1016/B978-0-12-818234-5.00120-6.
- Tizzani, P., Battaglia, M., Castaldo, R., Pepe, A., Zeni, G., and Lanari, R., 2015, Magma and fluid migration at Yellowstone Caldera in the last three decades inferred from InSAR, leveling, and gravity measurements: Journal of Geophysical Research: Solid Earth, v. 120, p. 2627–2647, doi:10.1002/2014JB011502.

- Uddin, K., Matin, M.A., and Meyer, F.J., 2019, Operational Flood Mapping Using Multi-Temporal Sentinel-1 SAR Images: A Case Study from Bangladesh: *Remote Sensing*, v. 11, p. 1581, doi:10.3390/rs11131581.
- USGS, 1972, Geologic Map of Yellowstone National Park: U.S. Geological Survey Miscellaneous Geologic Investigations I-711.
- Veci, L., Lu, J., Fomelis, M., and Engdahl, M., 2017, ESA's Multi-mission Sentinel-1 Toolbox: , p. 19398.
- Waldrop, H.A., and Hyden, H.J., 1962, Landslides Near Gardiner, Montana: U.S. Geological Survey Short Papers in Geology, Hydrology, and Topography Professional Paper 450-E, E11–E14 p.
- Wegnüller, U., Werner, C., Strozzi, T., Wiesmann, A., Frey, O., and Santoro, M., 2016, Sentinel-1 Support in the GAMMA Software: *Procedia Computer Science*, v. 100, p. 1305–1312, doi:10.1016/j.procs.2016.09.246.
- Whalley, W.B., and Azizi, F., 2003, Rock glaciers and protalus landforms: Analogous forms and ice sources on Earth and Mars: *Journal of Geophysical Research: Planets*, v. 108, doi:10.1029/2002JE001864.
- Xu, Y., Schulz, W.H., Lu, Z., Kim, J., and Baxstrom, K., 2021, Geologic controls of slow-moving landslides near the US West Coast: *Landslides*, v. 18, p. 3353–3365, doi:10.1007/s10346-021-01732-3.
- Yan, Y., Doin, M.-P., Lopez-Quiroz, P., Tupin, F., Fruneau, B., Pinel, V., and Trouve, E., 2012, Mexico City Subsidence Measured by InSAR Time Series: Joint Analysis Using PS and SBAS Approaches: *IEEE Journal of Selected Topics in Applied Earth Observations and Remote Sensing*, v. 5, p. 1312–1326, doi:10.1109/JSTARS.2012.2191146.

Yunjun, Z., Fattahi, H., and Amelung, F., 2019, Small baseline InSAR time series analysis:

Unwrapping error correction and noise reduction: *Computers & Geosciences*, v. 133, p. 104331, doi:10.1016/j.cageo.2019.104331.

Zellman, M.S., DuRoss, C.B., Thackray, G.D., Personius, S.F., Reitman, N.G., Mahan, S.A., and

Brossy, C.C., 2020, Holocene Rupture History of the Central Teton Fault at Leigh Lake, Grand Teton National Park, Wyoming: *Bulletin of the Seismological Society of America*, v. 110, p. 67–82, doi:10.1785/0120190129.

2. A LiDAR-Based Landslide Inventory and Analysis of Landslide Distribution in Yellowstone National Park

2.1. Introduction

2.1.1. Why Study Landslides

Landslides are incredibly widespread and destructive geologic hazards, killing thousands of people and causing billions of dollars in damage to infrastructure around the world every year (Froude and Petley, 2018; Godt et al., 2022). Landsliding is also a key process for shaping landscapes as they alter topography, accelerate weathering, and deliver large volumes of sediment to river channels (Korup et al., 2010). Understanding where and why landslides occur is essential for characterizing landslide hazard and assessing risk, and for exploring landscape evolution, particularly in light of changing climate and increasing human population.

Landslides can occur without an obvious trigger, or be initiated by other natural hazards, like intense storms or earthquakes (Godt et al., 2022). Hillslope stability is influenced by material and topographic properties, as well as environmental conditions. Many factors, often working in concert with one another, have been shown to influence these properties and make some areas more prone to landsliding than other including properties of bedrock geology (Roering et al., 2005; Xu et al., 2021), presence of clay minerals (Calabro et al., 2010; Watkins et al., 2020), a decrease in soil cohesion and infiltration capability following wildfires (Parise and Cannon, 2012), vegetation removal (Montgomery et al., 2000), and permafrost melting and topographic readjustment following glacier retreat (Ballantyne, 2002; Holm et al., 2004; Cossart et al., 2008). Earthquakes (Tanyaş et al., 2021), rapid snow melt (Chleborad, 1998), and intense precipitation events (Coe et al., 2016; Handwerger et al., 2019) can destabilize slopes that are already primed to fail. As the Earth's climate warms, intense precipitation events, including rain-

on-snow, are expected to become more common in many regions, which may trigger more landslides (Gariano and Guzzetti, 2016). Understanding the interplay between all of these predisposing and triggering factors is essential to understanding why landslides occur where they do and for predicting where they may occur in the future.

2.1.2. Landslide Inventories

Landslide inventories are foundational data sets for assessing landslide hazard, creating susceptibility maps, and investigating patterns of landscape evolution. We cannot understand or attempt to predict something if we do not know where, and under what conditions it occurs. Published landslide inventories take a variety of forms but generally describe the location, and selected attributes of landslides that span multiple hillslopes (Guzzetti et al., 2012). Inventories may compile specific types of slope failures (e.g., Hungr et al., 2008; Blahut et al., 2010; Lauknes et al., 2010; Mackey and Roering, 2011), document landslide events that occurred in response to specific triggers (e.g., Keefer, 1984; Coe et al., 2014; Marc et al., 2019; Jones et al., 2021), or document the cumulative record of all deposits present on the landscape at the time of the inventory (e.g., Cardinali et al., 1990; Case, 1990; Bennett et al., 2016).

Landslide inventories are compiled using a combination of remote sensing and field-based observations. Increasing availability of LiDAR in particular has allowed for highly accurate identification of landslide features over large areas, supplanting stereographic image interpretation as the “best” technique for identifying landslide deposits, especially in vegetated areas (Burns and Madin, 2009; Roering et al., 2013).

There is no agreed-upon protocol for creating or validating a landslide inventory (Guzzetti et al., 2012), which hinders the comparison of maps prepared by different groups. The

United States' government passed the National Landslide Preparedness Act in 2021, which aims to reduce national losses due to landslides through coordinated multi-agency efforts to identify and communicate landslide hazard and improve emergency response (Godt et al., 2022). Though a national landslide inventory is an essential product to support the act, inconsistent protocols and resources allocated to landslide mapping across the country hinders collaboration and standardization between the different groups responsible for creating and compiling landslide inventory maps.

2.1.3. Knowledge Gap/Opportunity

The USGS collected LiDAR data for all of Yellowstone National Park in the fall of 2020, providing an unprecedented look at the ground surface of this geologically diverse and unique area. Previous information on landslide distribution throughout the park comes from bedrock and surficial geologic maps (Ruppel, 1972; Smedes and Prostka, 1972; Love and Keefer, 1975; Pierce, 1979) and from the Wyoming Statewide Landslide Inventory (Case, 1990). The geologic maps were not focused on landslides and do not include landslides classifications or other details. The Case (1990) inventory, which was created largely through interpretation of aerial photographs, does not cover the portions of the park in Montana and Idaho and includes many features that are not typically considered mass movements, including slopewash, colluvium, and solifluction deposits.

This study aims to improve upon these previous works by creating a geospatial inventory of all landslide deposits throughout Yellowstone National Park at a 1:4,000 scale that includes type classifications, as well as topographic and geologic attributes to better define the context in which these movements occur. We then use the inventory to examine patterns in the park-wide

distribution of landslides, assessing park-scale controls on landslide occurrence and building a dataset that creates a robust foundation for future hazard and risk assessment.

2.2. Site Description

Yellowstone National Park is centered on a broad, high-elevation plateau surrounded to the northwest, north, east, and south by the rugged Gallatin, Beartooth, and Absaroka mountain ranges. The ranges expose metamorphic, sedimentary, and volcanic rocks that are Precambrian to Tertiary in age (Christiansen, 2001). Tertiary rocks are the Absaroka Volcanic Supergroup, composed of interbedded volcanic and sedimentary rocks that form the Absaroka and part of the Gallatin ranges. Mesozoic and Paleozoic sedimentary rocks form most of the Gallatin Range and crop out in the southern part of the park. Precambrian metamorphic rocks are found to a limited extent in the northern part of the park.

While its origins are contested (e.g., Christiansen et al., 2002; Camp and Wells, 2021) the Yellowstone Plateau is generally accepted to be the modern position of a time-transgressive volcanic hotspot that had been moving northeastward across North America since at least 17 Ma (Pierce and Morgan, 2009). Three caldera-forming supereruptions occurred around 2 Ma, 1.3 Ma, and 0.63 Ma; these eruptions produced thick tuff deposits and were followed by extensive rhyolite flows that filled the subsiding calderas, creating a broad, high-elevation plateau in the center of the park (Christiansen, 2001).

During the Pleistocene, the Yellowstone plateau hosted the largest ice cap south of the Laurentide Ice Sheet over multiple glacial cycles. Increased precipitation and a cooler climate allowed glaciers from the surrounding mountain ranges to coalesce onto the plateau and form a single, multi-lobed ice mass (Licciardi and Pierce, 2018). Erosion from these lobes steepened

valley walls, mobilized massive amounts of sediment, and largely erased records of previous surficial processes, including landslide deposits. During the most recent Pinedale glacial cycle, the ice cap formed ~22 ka and retreated rapidly at ~13 ka (Licciardi and Pierce, 2018; Licciardi et al., 2022), so we assume that the landslide deposits visible today are mostly an accumulation of processes acting over that post-glaciation time period.

The Yellowstone plateau's unique geographic setting at the eastern end of the low-elevation Snake River Plain creates an orographic precipitation effect. Moisture from the Pacific Ocean is funneled east until it hits the topographic barrier of the Yellowstone plateau where ascending and cooling air masses then release significant amounts of precipitation throughout the park (Licciardi and Pierce, 2018). Presently, a majority of the park's annual precipitation falls as snow that is released as a pulse of melt in the spring (Gardner et al., 2010). Intense thunderstorms punctuate generally dry summer conditions. As the Earth's climate warms in the coming decades, total annual precipitation in Yellowstone is expected to increase, though a diminishing proportion will be falling as snow (Hostetler et al., 2021).

Yellowstone is one of the most seismically active regions in the United States due to the combined influence of the volcanic hotspot, hydrothermal activity and its tectonic setting in the Basin and Range province. Swarms of mostly low-magnitude earthquakes occur periodically throughout the park related to the movements of magma and fluids in the subsurface (Shelly et al., 2013). Yellowstone also lies at the eastern extent of the Basin and Range tectonic province; the 1959 Hebgen Lake earthquake occurred just outside the park on multiple Basin and Range faults and produced widespread landslides (Hadley, 1964). The Teton Fault lies just south of Yellowstone National Park; it has not experienced significant activity in recorded human history

but paleoseismic studies show multiple surface rupturing events on the fault since the retreat of the Pinedale ice sheet (Zellman et al., 2020).

2.3. Methods

2.3.1. Data Sets

We identified and characterized landslide deposits primarily through inspection of a LiDAR-derived, 0.5-meter resolution bare-earth digital elevation model and slope map. Woolpert Inc collected the LiDAR in two projects for the USGS in September and October 2020, when both vegetation and snow cover were at a minimum in the park. We downloaded 500 x 500 m² tiles covering the entire park from the USGS LiDAR Explorer in February 2022 (<https://apps.nationalmap.gov/lidar-explorer/#/>) and combined them in ArcGIS Pro to create continuous rasters for the northern and southern halves of the park.

Satellite imagery from ESRI's World Imagery base map provided a secondary reference to the LiDAR, offering a general sense of vegetation cover and helping to identify human-made features. We used digital bedrock geology (NPS, 2020a) and surficial geology (NPS, 2020b) datasets from the National Park Service Geologic Resources Inventory to determine the underlying lithology of landslide deposits. These digital maps compile 1:24,000, 1:62,500, and 1:125,000-scale maps produced by the USGS and the Montana Bureau of Mines and Geology. Field checks were conducted on approximately 40 deposits throughout the park to confirm information on our mapped extents, inferred movement type, deposit material, substrate lithology and the activity state of selected landslides. These observations, where applicable, are recorded in the notes point feature in the inventory database.

2.3.2. GIS Inventory Structure

We created a geodatabase to identify landslide deposits and associated features. Our inventory is an expanded version of Slaughter et al.'s (2017) Streamlined Landslide Inventory Protocol (SLIP) that incorporates some of the elements of a more detailed inventory described in Burns and Madin (2009). We ultimately determined that this adapted protocol was the best way to accomplish our goals to map such a large area (~10,000 km²) over a relatively short period of time (~1 year) and accurately characterize the landforms and substrates based largely on remotely sensed observations.

Our geodatabase combines multiple polygon, line, and point features. Three different polygon features identify landslide deposits, rock glaciers, and suspected movements. Deposit and rock glacier polygons contain attribute tables. The deposit attribute table contains a landslide classification (detailed below), bedrock lithology interpreted from head scarps, surficial geology, deposit area, comments, aspect, and elevation. The rock glacier attribute table contains the same fields, excluding a landslide classification and surficial geology. We use another polygon feature to define, where present, the upper bounding scarp of each deposit, which may expose the primary failure plane of the deposit. Two different line features denote (1) scarps that do not bound deposits and (2) flow paths for channelized debris flows. Two different point features (1) mark initiation points for channelized debris flows and (2) mark the location of field or mapping notes.

2.3.3. Identification of Landslide Deposits

Deposits were identified through a combination of multiple characteristics including the presence of upper or internal scarps, hummocky topography, fan- or lobe-shaped deposits,

sometimes with oversteepened fronts, breaks or offset in drainages or other topographic features, or levees and other flow features. Rock glaciers are distinguished by lobate forms, chaotic furrowed texture, and topographic position at the bottoms of largely north-facing cirque valleys.

We do not outline the deposits of every reactivation. Many of our mapped deposits, especially in the cluster in the southern part of the park, likely initiated as several separate deposits whose boundaries are now indistinguishable. We typically map coalesced features like these as a single deposit unless there are clear secondary failures. Throughout our inventory, many of our individual polygons likely represent more than one landslide “event.”

2.3.4. Field Observations

We performed field checks on about 40 individual landslide deposits throughout the park during summer 2022. After creating a preliminary deposit inventory from LiDAR, we identified areas that were accessible by either day hikes or overnight backpacking and would be representative of the range of deposits and substrates we observed throughout the park. We were able to visit about 40 deposits along US Highway 191, near Mammoth Hot Springs and Flagg Ranch, along the East Entrance Road, along Basin Creek south of Heart Lake, and around Fawn Pass in the Gallatin Range. We were unable to access features between Tower Junction and the northeast park entrance due to road closures from historic flooding in mid-June.

While in the field, we used ESRI Field Maps to display satellite imagery, LiDAR-derived elevation and slope maps, our preliminary inventory, and digital bedrock and surficial geology maps. We used GPS-referenced point features to record observations that included signs of recent movement, deposit material, substrate lithology, vegetation characteristics, water features

and failure geometry. Those observations are included in the final geodatabase and inform the characterization of several individual features as well as overall patterns in the inventory.

2.3.5. Classifying Landslide Deposits

We use a simplified version of Cruden and Varnes (1996) movement and material types to classify landslide deposits by their mode of emplacement. We do not attempt to characterize the initial mode of failure for deposits, but rather seek to describe the mechanisms that created the landforms that are currently present on the landscape. Movement types include falls, slides, and flows. Types of material are based on grain size and include rock (intact bedrock prior to movement), debris (aggregate particles of which 20% or more are greater than 2 mm in diameter), and earth (aggregate particles of which 20% or less are greater than 2 mm in diameter). Because this inventory is largely based on remote sensing observations, it is not feasible to accurately distinguish the difference between earth and debris (Slaughter et al., 2017). Topographic roughness, aerial imagery, field observations, and our general knowledge of Yellowstone's glacial history and thin soils led us to assume that most, if not all of the features mapped contain a significant debris fraction and are best classified as debris movements. Our simplified classification ultimately includes complexes, debris and rock slides (which we combine in our analysis), rockfalls (creating protalus lobes), channelized debris flows, and open-slope debris flows. Other landslide types were either not present in our study area or not distinguishable from these other types in LiDAR and satellite imagery.

2.3.6. Rock Glaciers

Ice-influenced landforms are not typically included in landslide classification schemes (Cruden and Varnes, 1996), but we propose in this study that rock glaciers share key morphological and kinematic characteristics with some landslides, so we include them in this inventory as a type of landslide deposit. Rock glaciers accelerate the transport of debris from valley headwalls to valley floors (Anderson et al., 2018) and respond to multi-year shifts in precipitation patterns (Brencher et al., 2021) and so function similarly to landslides from a landscape evolution perspective. Some rock glaciers are thought to have formed through the interaction of conventional landslide processes (e.g., rockfall) with glaciers or snow fields (Whalley and Azizi, 2003).

2.3.7. Extracting Attributes

Bedrock and surficial geology were determined from interpretation of digital geologic map layers, which were compiled at scales between 1:125,000 and 1:24,000. Bedrock geology was assessed at the head scarp rather than over the entire deposit itself, while we noted the mapped surficial geology within the landslide polygon. If the bedrock map also noted the deposit area as Q_{ls} (Quaternary landslide), that was included in the bedrock geology field, along with, where possible, the inferred failure lithology. Because most of the mapped deposits have rocky head scarps that are meters to tens of meters high, we are confident that the mapped bedrock lithology is relevant to the emplacement of these features. The attribute table also included a simplified geology field where we noted the generalized substrate lithology and age, based on generalized lithologic domains of the park. We used a 10-m DEM from the USGS National Map and ESRI's zonal statistics tool to calculate the average aspect and elevation of landslide deposit

polygons. Deposit area was automatically calculated from the polygons and added to the attribute table.

2.3.8. Visualization and Analysis Tools

We created histograms from the deposit feature attribute table. We decided to display inventory characteristics in terms of area rather than feature count because we feel that best represents the extent and impact of landsliding.

We visualize the inventory as a series of heat maps weighted by area, which helps to illuminate clusters of mapped landslide deposits- essentially where the most material is moving. These maps are created using a kernel density algorithm, which takes the centroid of each deposit and fits a smooth quadratic surface over it where the highest value is at the center and values taper to zero over a set distance (ESRI, 2023b, 2023a). Each of these surfaces is multiplied by the area of the deposit. The final kernel density raster is calculated by adding together all of the kernel surface values- so landslides with large areas and locations where many of these surfaces overlap (where there is a large number of landslides) have higher kernel density values. We visualize these kernel surfaces as contour maps that highlight the largest kernel density values, which are the locations where the greatest landslide area is concentrated. We used ESRI's Spatial Autocorrelation (Global Moran's I) tool to determine the distance at which autocorrelation is the strongest and used this as the search radius to calculate kernel density, to best display the overall clusters within our inventory (ESRI, 2023c).

2.4. Results

2.4.1. Characteristics of Landslide Types

We distinguished landslide deposits by their dominant movement style. We prioritize the distinction between slides and flows, suspecting that the enhanced mobility of flow-type movements (e.g., Watkins et al., 2020) presents a different hazard than that of slides. Many deposits display characteristics of multiple landslide types and we typically chose to assign a single classification based on the dominant characteristics. Our goal is to classify the mode of emplacement of the feature visible on the landscape today- not necessarily the initial mode of failure. Strict classifications were complicated by pervasive reactivation that alters the type of material moving or the style in which it moves over time.

2.4.1.1. Channelized Debris Flows

Channelized debris flow deposits are coarse-textured fans at the mouths of scoured channels (Figure 2.1). They are characterized by a low-relief divergent texture with irregular longitudinal lobes and discontinuous incised channels. Debris flow fans share many characteristics of alluvial fans and, in many cases, the two features are difficult to distinguish from each other. Alluvial channels may transport debris to fans, but in this inventory, we choose to map only the fans with rougher textures indicative of more energetic, high volume, coarse depositional events. We assume that these features represent the most significant areas of debris transport. Debris flow paths are drawn through scoured channels from the head of the fan deposit to a clear break in channel topography, which is marked by the “debris flow initiation point.” Many individual debris flow fans have multiple flow paths and initiation points.

2.4.1.2. Open-Slope Debris Flows

Open-slope debris flow deposits are characterized by their hillslope-wide topographic extent and fluid-like, highly deformed internal texture (Figure 2.1). Other distinguishing features include nested longitudinal ridges and levees parallel to transport direction, concentric transverse ridges and furrows perpendicular to the transport direction, and steep-fronted toes. Many deposits flow around other topographic features. The upper part of many, especially the larger, of these features is composed mostly of talus; the toes tend to be more heavily vegetated. Closed basins between hummocks often collect water near the head scarps or between ridges closer to the toes of these features. Parts of these features may be confined to channels but they do not scour those channels like channelized debris flows. In the upper reaches of these features, some evidence of rotated blocks suggest that these features initiated as rock or debris slides, but converted to flows during extended, high-energy transport.

2.4.1.3. Rockfall/Protalus Lobes

Steep fronted talus deposits, located at the base of near-vertical slopes, were classified as rockfall/protalus lobes (Figure 2.1). These features are typically much wider than they are long and parallel their source cliffs. The deposits have steep fronts and occasionally thick internal ridges that are generally parallel to cliff faces. Many of the deposits had a rougher texture than the adjacent talus slope. We did not map all talus deposits in the park, which are accumulations of likely small-magnitude events. We assume that these lobes are the product of larger events and chose to map them because of their somewhat similar morphology to our other landslide features and, as larger features, their greater potential for future activity.

2.4.1.4. Debris and Rock Slides

We group translational and rotational debris and rock slides together for our analysis to encompass all deposits that are emplaced through sliding along a basal surface with minimal deformation of material being moved. They are often characterized by parallel, nested, occasionally uphill-facing scarps and intact blocks, particularly near the head scarp (Figure 2.1). As slides are reactivated, travel farther downslope, or become saturated, they often break up into flows (Cruden and Varnes, 1996). This raises the likelihood that flows are overrepresented in our inventory simply as a function of the complexity and reactivation of many of the deposits.

2.4.1.5. Rock Glaciers

Rock glaciers, in general, are lobe-shaped masses at the bottom of cirque valleys and at the base of talus slopes (Figure 2.1). Many of the rock glaciers in our inventory were characterized by thick, ropy internal ridges and furrows and terminate in steep toes. In aerial imagery, they are largely unvegetated. Rock glaciers share some characteristics with open-slope debris flows but are distinguished by their thicker ridge features that are a product of ice-supported internal deformation and a lack of upper or internal scarps.

2.4.1.6. Complexes

We mapped complexes where we saw deposits that had characteristics of multiple landslide types that seemed to influence each other and occupied similar extents of the overall deposit (Figure 2.1). Arguably, most of the deposits in our inventory contain elements of multiple landslide types (i.e., rockfall from head scarps creating talus aprons or a small intact block at the top of a long-runout open-slope debris flow) but we saved the complex classification

for the features that seemed to be equally influenced by different movement styles. In our inventory, we use the complex types to classify deposits shared characteristics of both slides and flows without a clear distinction (i.e., internal scarps or major difference in surface roughness) between the two domains. We avoided classifying complexes as much as possible, in order to capture differences in movement styles across the park; but we felt that these particular slide/flow complexes were distinctly different than the other deposits that we mapped as either slides or flows.

2.4.1.7. Suspected Movements

Suspected movements are features that might have been emplaced through landsliding but were different enough from the other mapped deposits that we were not confident that they were not also products of other processes. This classification also includes landslide deposits that are on the edge of the map, so we cannot see their full extent, and some very shallow lobe-like features that may be solifluction. We thought that these features were useful to include from a hazard perspective, but were unable to fully characterize them to include in our overall analysis.

2.4.2. Spatial Distribution of Entire Inventory

In total, we mapped 1756 landslide deposits and 62 rock glaciers. Almost all of these features occur in clusters outside of the most recent caldera and low-relief rhyolite plateaus in the center of the park (Figure 2.2). Three clusters dominate the inventory: one in the northwest corner of the park in the Gallatin Range, one in the northeast corner of the park at the northern end of the Absaroka Mountains, and one near the southern park entrance south of Heart Lake.

2.4.3. Distribution of Landslide Types

The different landslide types do not occur homogeneously throughout the overall population of landslides. Open-slope debris flows dominate the inventory, representing a larger area than all of the other deposit types combined (Figure 2.3). Their largest clusters occur in the Gallatin Range and south of Heart Lake, which are also where the bedrock is composed of predominantly Meso- and Paleozoic sedimentary rocks. Complexes occur in three large clusters that are the same as the distribution of the overall inventory. Slides are more evenly distributed around the caldera, though they are largely absent from the area south of Heart Lake. Channelized debris flows are concentrated in the northeast corner of the park. Rock falls are the only movement type with a significant presence inside of the caldera area and do not occur on the east side of the park. The majority of rock glaciers are found in the Gallatin Range. The eastern border of the park in the Absaroka Range had few landslides even though it has high relief, formerly-glaciated terrain.

2.4.4. Substrate Lithologies

Sedimentary lithologies underlie the greatest proportion of landslide deposits in our inventory (Figure 2.4). Despite their limited exposure in the park, Mesozoic and Paleozoic sedimentary lithologies are the single largest source lithology for landslides. Volcanic rocks make up the next most common source lithology, with Tertiary volcanics being the most common and underlying some of the largest individual deposits. Metamorphic lithologies as well as Quaternary surficial deposits and rhyolite/basalt flows are the least common sources and do not form very large deposits. Average aspect and elevation deposit attributes did not reveal any patterns.

2.5. Discussion

2.5.1. Different Landslide Risks Throughout the Park

Because different landslide types are not evenly distributed around the park (Figure 2.3), park managers can expect to encounter different landslide hazards in different areas, which has implications for future risk analyses within Yellowstone. Park resource managers will still want to conduct site-specific investigations, but our inventory provides a useful starting point and context for these. Different landslide types generally present different hazards, may be triggered by different conditions, and require different mitigation measures. Flows are much more mobile than slides, often incorporating air or water, and so may occur at greater speeds and travel farther (Highland and Bobrowsky, 2008). Rock falls happen extremely quickly and their length of travel is related to the setting in which they fail.

Our inventory shows that channelized debris flows occur almost exclusively in the northeast corner of the park, presenting particular risks to the northeast entrance road that are not as significant for roads in other areas of the park. The large cluster of landslide deposits near the southern park entrance are mostly open-slope debris flows, which we would expect to behave differently than slides (e.g., possibly moving faster or farther) or channelized debris flows (e.g., mobilizing different amounts of water and sizes of material). Large rock fall deposits (proctalus lobes) are concentrated in the northwest and west of the park; these rapidly emplaced movements also present different risks to infrastructure, that seems to be unique to that region.

2.5.2. Lithologic Influence on Landslide Distribution

A vast majority of landslides, of all types, occur outside of the most recent caldera. This caldera-circling pattern does not align with regional patterns of precipitation, earthquake activity,

or glacial history (Figure 2.2). While these factors likely influence local landsliding regimes, we suggest that bedrock lithology, for three reasons, correlates and may influence the park-scale patterns in landslide activity.

Firstly, the interior of the caldera is underlain by thousands of cubic kilometers of rhyolite flows (Christiansen, 2001), which have created a relatively low-relief, lithologically homogeneous landscape compared to the mountains ringing the caldera. Outside of the caldera, where we see the most landslides, older and more diverse lithologies have been uplifted and later eroded by rivers and glaciers to form steep mountains and deep canyons, offering more relief to generate mass movements.

Secondly, we suspect that composition of particular rock units plays an important role in landslide distribution. The disproportionate representation of Mesozoic and Paleozoic sedimentary rocks in the landslide inventory suggests that those lithologies are more susceptible to landslides (Figure 2.4). We suspect that the presence of shale or clay interbeds or bedding planes—which generally occur in these areas (Ruppel, 1972; Love and Keefer, 1975)—may form planes of weakness and zones of saturation that support persistent landslides. Ruppel (1972) noted that, in the Gallatin Range, north-facing valleys and cirques with north-dipping rock units seem particularly prone to landsliding. The Tertiary rocks contain ash beds and many of the sedimentary units are held together by an ashy matrix (Smedes and Prostka, 1972). Compared to the Yellowstone eruptive products, these ashes have had considerable time to weather to clays and form weak, failure-inducing layers. Flow-type movements are softer material moving over a rigid surface (Hungr et al., 2001), while hummocks are formed where rigid material moves over a less rigid surface (Paguican et al., 2014). Both flow features (e.g. levees) and hummocks,

which are common in our mapped features, then suggest rigidity differences within these deposits.

Finally, contacts between rock units of different ages and lithologies offer a final important geology-controlled context for the distribution of landslides throughout the park. In the field, we repeatedly observed landslide deposits composed of debris made of Quaternary tuff, which also capped head scarps. Further downslope, deposits incorporated older, crumblier rock. This implies that the failure occurred at some sort of basal contact between the tuff and the underlying lithology. This is not surprising as the paleotopography at the time of eruption likely had a slope and the paleosol at the contact is typically clay rich. We also consistently observed this pattern when comparing our landslide polygons to the bedrock geologic maps; mapped contacts frequently intersected with our mapped deposits or head scarps.

2.5.3. Open-Slope Debris Flows Dominate Landslide Type

Open-slope debris flows represent the greatest proportion of the inventory (Figure 2.3). This is not a landslide classification that has received much attention in the literature. Many of the open-slope debris flows we mapped had previously been classified as earthflows (e.g., Pierce, 1973) or share morphology with features that, in other locations, have been described as debris avalanches (e.g., Geertsema et al., 2006; Coe et al., 2016). We prefer the classification of open-slope debris flows to debris avalanche because the classification of debris avalanche tends to imply an extremely high speed of emplacement with air as the interstitial fluid (Cruden and Varnes, 1996; Hungr et al., 2014; Coe et al., 2016). We do not have the information to assess the speed of emplacement of these features and feel that the classification of open-slope debris flow,

though not widely used, is the most accurate classification for what we see in Yellowstone, as we see clear flow features in decidedly debris-size deposits.

We attribute some of the ubiquity of flows to the age and pervasive reactivation of these deposits and some to a specific failure mechanism. As slides travel, blocks break up and incorporate water and air and move more like flows. As with the overall distribution of landslides, we suspect that lithology, particularly the presence of clays within sedimentary units, helps to create the large proportion of flow-type landslides that we see. Paleosols and thin ash beds, more common in the rock units surrounding the plateau, likely play a similar role.

2.5.4. The Conceptual Yellowstone Landslide

Overall, we suspect that basal planes of weakness, related to lithologic contrasts or weaknesses, are responsible for the initiation of many of the deposits we mapped (Figure 2.5). These planes of weakness may be influenced and exploited by other triggering factors present in the park, including glacial debuttressing, precipitation (in the form of snowmelt runoff saturating hillslopes or large rainfall events or a combination), and earthquakes. Because we see so many flow-type features, we suspect that there may be a significant amount of water involved with these failures. With subsurface clays, the basal slide planes may act as an aquitard, lubricating the deposit and supporting reactivation. Steep, rocky head scraps and thin soils lead us to believe that these are not shallow flows but have deeper planes of weakness that initiate slides in competent rock that energetically disaggregate and evolve downslope into debris flows.

2.5.5. Comparison to Previous Yellowstone Inventories

Our LiDAR-based inventory offers a more nuanced look at landslides than previous work. Our inventory maps ~1800 deposits comprising ~314 km². The Case (1990) inventory maps ~1300 features comprising ~364 km² in the Wyoming part of the park. All landslide deposits in bedrock and surficial maps comprise about 306 km² with ~900 identified deposits (NPS, 2020b, 2020a). 676 of our polygons overlap with landslides in the geologic maps; 1010 of ours overlap with the Case inventory. As expected, our inventory gives a more detailed look at landslide deposits than previous mapping efforts, while eliminating previously mapped features that do not have a clear surface expression.

2.5.6. Extraordinary Preservation of Deposits

We have assumed that our inventory represents ~13,000 years of landslide movements. It is easy to think of these deposits as representing singular, discrete events that remain on the landscape and are subject to modification through erosional processes. If that were the case, we might expect to see differential preservation related to the ages of deposits, with older deposits displaying more subdued morphology that may make them more difficult to identify.

Notably, throughout this inventory, we encountered very little difficulty in differentiating landslide deposits from undisturbed terrain. Most ambiguity was related to assigning different classification types. We suspect that there are multiple reasons, likely acting in concert, that contribute to the preservation of these deposits. As previously stated, the Pinedale Ice Sheet acted as a reset to the landscape, so there are simply not a lot of deposits that are old enough to have been modified into ambiguous landforms. Additionally, continued reactivations or gradual,

creeping deformation may contribute to the maintenance of the distinct morphology of these landslide deposits.

2.5.7. The Advantage to Non-Automated Mapping

Drawing and classifying ~1800 landslide deposits polygons was a time-intensive effort that required a skilled human to perform, which raises questions over the advantage of manual mapping compared to using an automated detection tool (e.g., Booth et al., 2009). We believe that creating this inventory would not have been possible using automated methods and that creating the inventory was a valuable educational experience that enhanced the mapper's ability to make interpretations and draw conclusions about the inventory. The scope of this study— with particular regard to its broad spatial extent, coupled with the level of detail needed to identify different deposit types— challenges the ability of automated mapping tools. The complexity of the continuously reactivated and overlapping deposits would also strain the capabilities of automated mapping and

We can also think about the “informed interpreter” as an outcome of this work. After creating this data set, the mapper is now an expert in recognizing landslide deposits on the Yellowstone landscape, as well as their context. This expertise informs interpretation of patterns and processes at different scales that would not be possible or nearly as effective if this inventory had been generated automatically.

2.5.8. Limitations of this Inventory

This inventory highlights challenges to creating static characterizations of dynamic landforms. Throughout this inventory, we see clear signs – overlapping lobes, internal scraps,

differences in roughness – that many of these landslide deposits represent multiple generations of movement. We speculate that many of their forms have changed over some period of time since their initial failure; but our type and material-based classification scheme does not have room to acknowledge this change. This evolution in type may impact hazard assessment and mitigation decisions and certainly reflects processes that we do not have a full picture of.

Because this inventory represents the accumulation of thousands of years of landslide initiation and reactivation, the record we see on the ground today does not capture the initial condition of many of the features we are mapping. We know that single events may set off a cascade of related, though morphologically distinct movements, potentially over a period of hours and may move more gradually over longer timescales (Coe et al., 2016). These are important considerations for exploring hazards and processes but cannot be assessed from this inventory.

2.6. Conclusion

We have created an updated, high-resolution landslide and rock glacier inventory that covers all of Yellowstone National Park, identifying over 1800 individual features along with their type and style of movement, and their source lithology. We found that most of the landslides within the park area are best described as open-slope debris flows and occur outside of the caldera area in the rugged mountain ranges that ring the Yellowstone Plateau. The bedrock geology of these ranges likely exerts an important influence on the distribution and mechanism of mass movements in the park; broad-scale bedrock patterns prime slopes to be exploited by more local triggers related to patterns of glacial debuitressing, earthquakes, and precipitation, all of which are influenced by the Yellowstone hotspot.

Despite its limitations, this inventory is a strong starting point for future studies; we cannot study landslides in Yellowstone if we do not know where they occur. By identifying the extent and types of landslides throughout the park, this data set may be used by park managers for risk analysis or for training a machine learning model to identify other landslides from LiDAR data. Additionally, future workers may add additional attributes to the existing geodatabase in order to investigate other spatial relationships and assess other controls on the landslide distribution we see, including local slope and different forms of precipitation. We hope that this database may be combined with or compared against other datasets and forms a baseline from which to study the temporal evolution of these features.

2.7. Figures

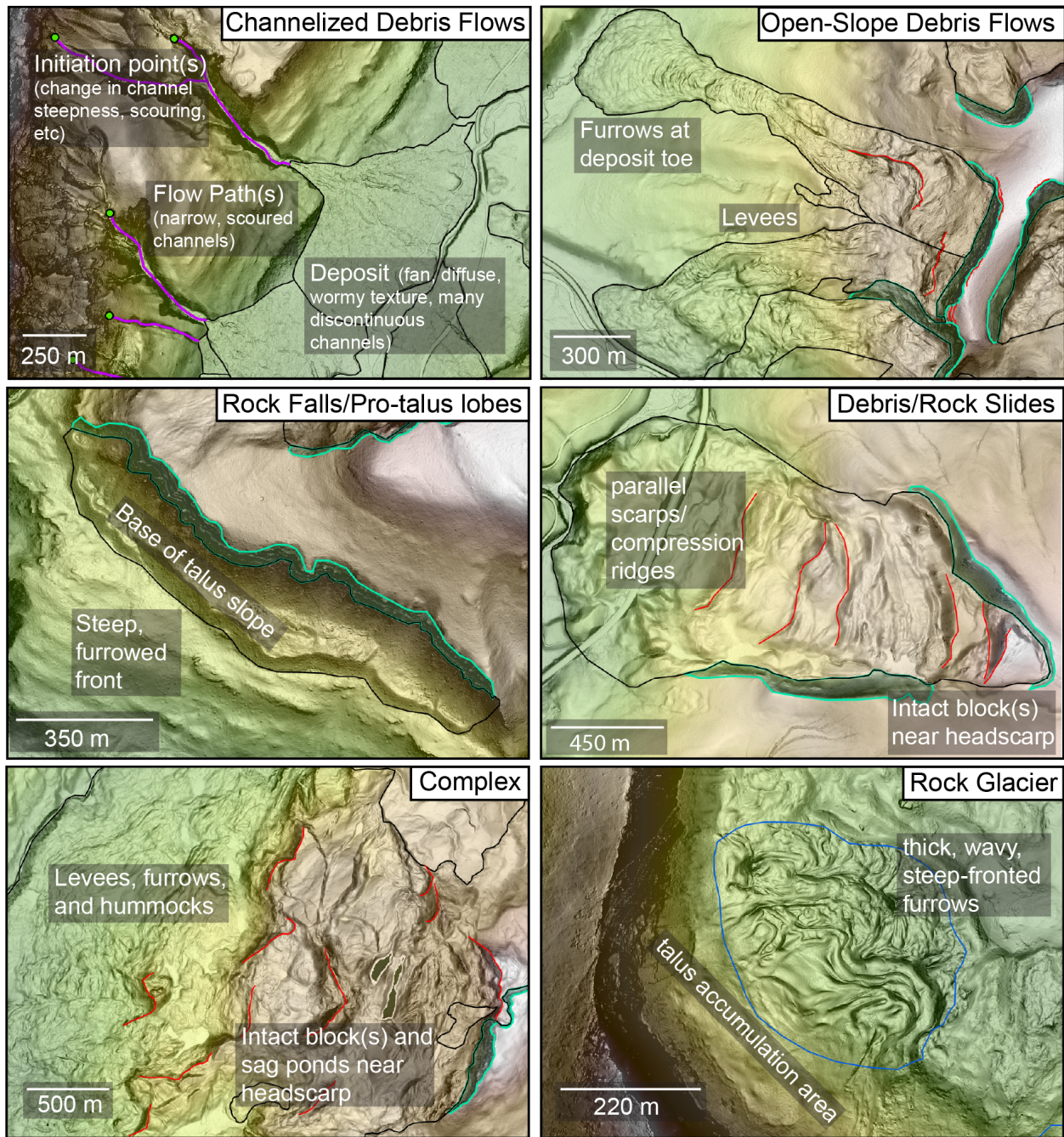


Figure 2.1. Examples of each landslide type in our inventory and some of their defining characteristics. Black polygons outline deposits (rock glacier is outlined in blue); purple lines show channelized debris flow paths, green points show debris flow initiation points, red lines indicate internal scarps, and teal polygons bound head- and side scarps. Note that the complex extends beyond the boundaries of the image.

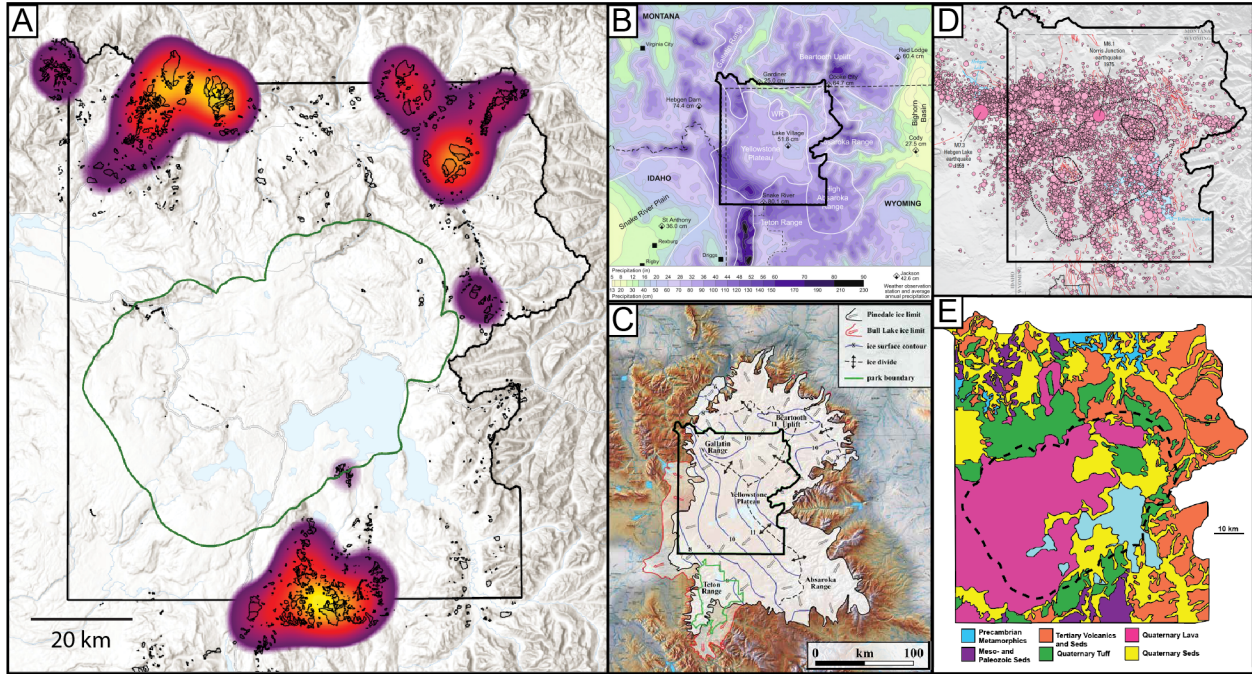


Figure 2.2. Distribution of mapped landslides (A) with maps of potential influences on that distribution (B-E). A) Shows all mapped landslides as small black polygons, fitted with a kernel density function, weighted by area, in order to show where the largest clusters of landslides are located. Hotter colors are greater concentrations of features. Large black polygon indicates national park boundary, green circular polygon outlines the 0.63 Ma collapsed and infilled caldera. B) Precipitation map of the Greater Yellowstone region; dark purple indicates higher annual precipitation. Adapted from Licciardi and Pierce (2018). C) Map of the greatest known extents of the Pinedale (22-13 ka) and Bull Lake (~150 ka) ice caps. Adapted from Licciardi and Pierce (2018). D) Map of recorded earthquakes in the Yellowstone region 1972-2017, adapted from Morgan et al., (2017). E) Simplified bedrock geology map of Yellowstone National Park, adapted from USGS (1972).

Distribution of Mapped Landslide Types

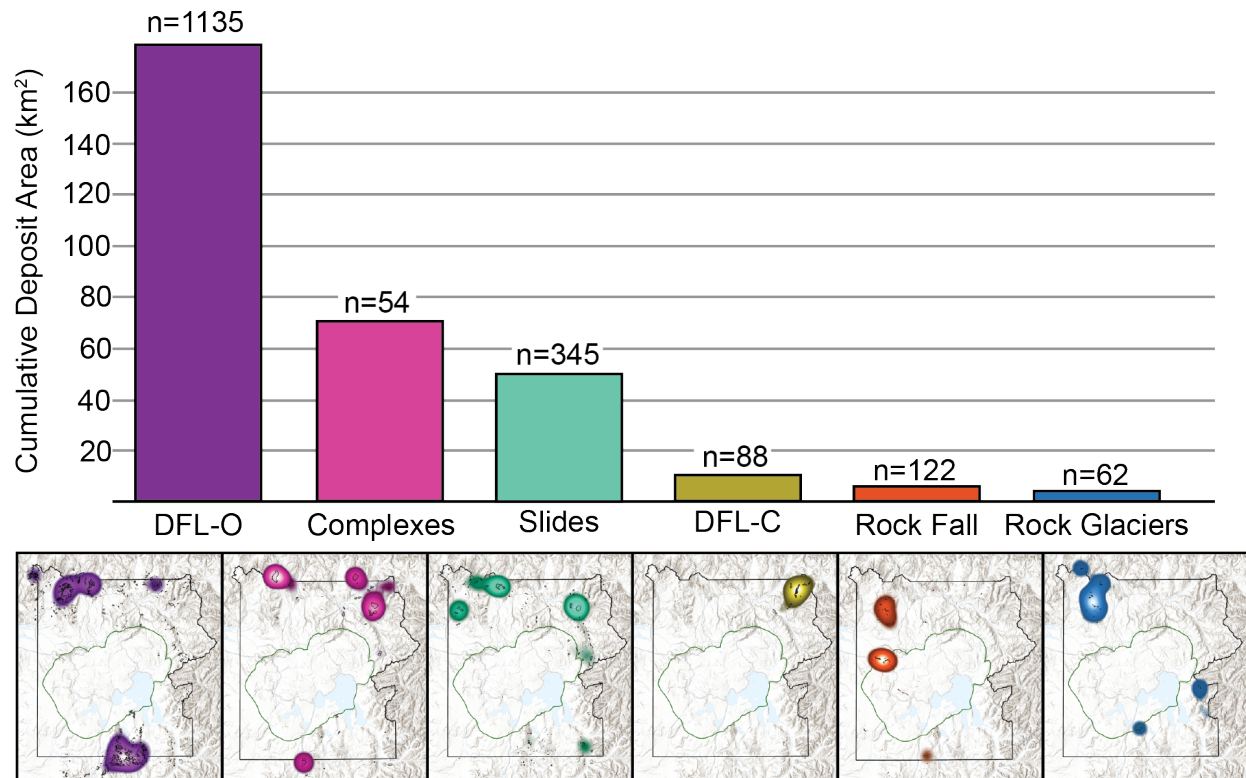


Figure 2.3. Distribution of mapped landslide types. Bar graph shows the cumulative area of each deposit type represented in the inventory, with the total count of deposits above each bar. Kernel density maps show the spatial distribution of each type of mass movement weighted by area, where whiter hues show the greatest concentration of features.

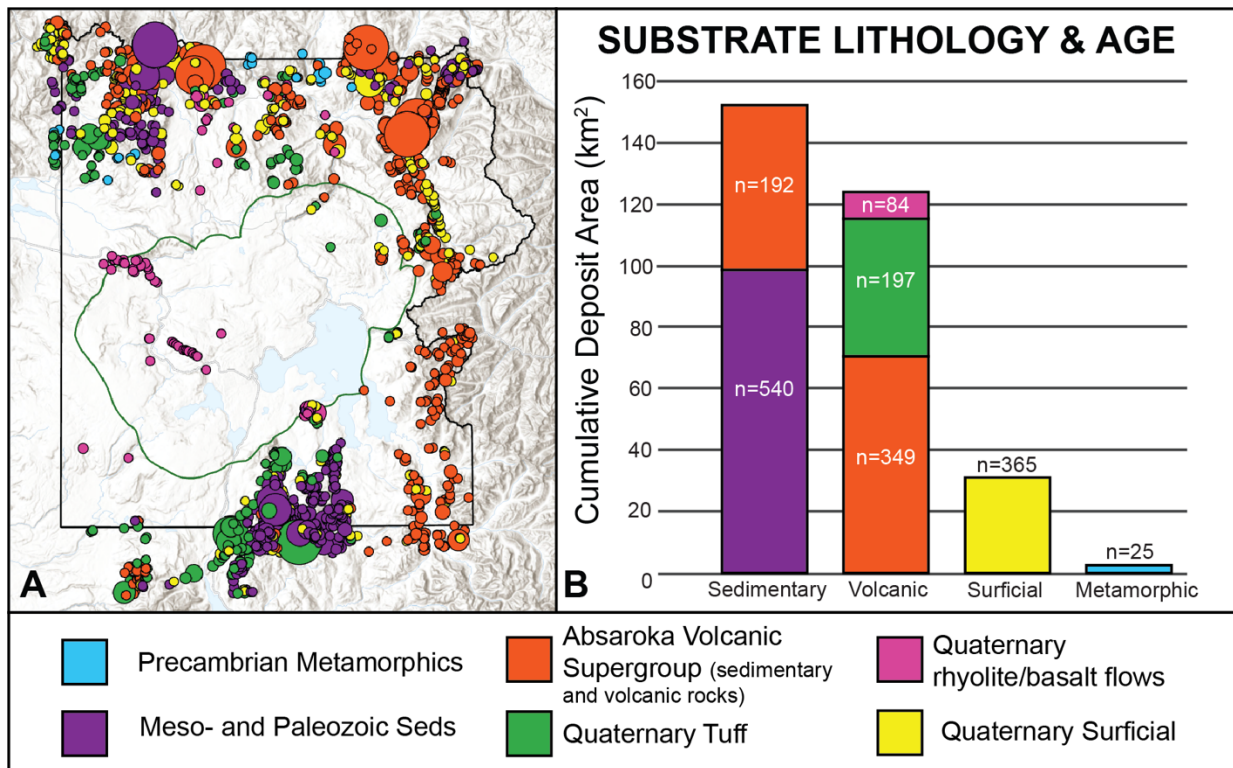


Figure 2.4. Distribution of bedrock lithologies associated with landslide deposits and rock glaciers. A) Map representing all mapped landslide deposits as points; points are scaled to landslide area. Colors indicate simplified bedrock type. B) Stacked bar plot shows the cumulative area of each simplified rock type represented in the inventory with the number of deposits noted in each category. 62 of our mapped deposits fell outside of the range of the geologic map boundaries so are not represented in this histogram.

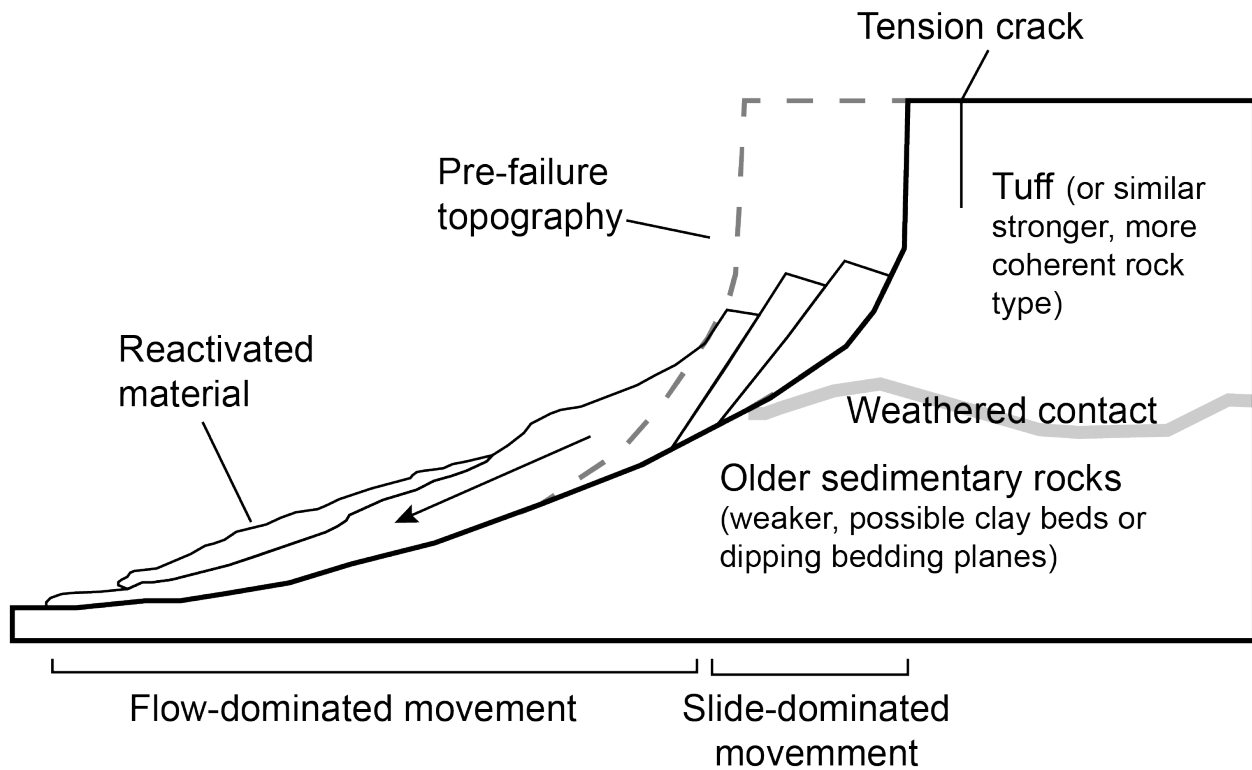


Figure 2.5. Conceptual cross-section depicting typical failure style of the open-slope debris flows throughout Yellowstone. Subsurface contacts between different rock types, along bedding planes, and/or with clay-rich paleosols or ash layers (labeled here as “weathered contact”) provide weaknesses that offer planes for slope failures to initiate as slide-type movements. With increasing transport, these slides pulverize their source material and may entrain significant amounts of water and rock below the failure plane, both of which facilitate more flow-type movement towards the toe of the deposit.

2.8. References

- Anderson, R.S., Anderson, L.S., Armstrong, W.H., Rossi, M.W., and Crump, S.E., 2018, Glaciation of alpine valleys: The glacier – debris-covered glacier – rock glacier continuum: *Geomorphology*, v. 311, p. 127–142, doi:10.1016/j.geomorph.2018.03.015.
- Ballantyne, C.K., 2002, Paraglacial geomorphology: *Quaternary Science Reviews*, v. 21, p. 1935–2017.
- Bennett, G.L., Miller, S.R., Roering, J.J., and Schmidt, D.A., 2016, Landslides, threshold slopes, and the survival of relict terrain in the wake of the Mendocino Triple Junction: *Geology*, v. 44, p. 363–366, doi:10.1130/G37530.1.
- Blahut, J., van Westen, C.J., and Sterlacchini, S., 2010, Analysis of landslide inventories for accurate prediction of debris-flow source areas: *Geomorphology*, v. 119, p. 36–51, doi:10.1016/j.geomorph.2010.02.017.
- Booth, A.M., Roering, J.J., and Perron, J.T., 2009, Automated landslide mapping using spectral analysis and high-resolution topographic data: Puget Sound lowlands, Washington, and Portland Hills, Oregon: *Geomorphology*, v. 109, p. 132–147, doi:[10.1016/j.geomorph.2009.02.027](https://doi.org/10.1016/j.geomorph.2009.02.027).
- Brencher, G., Handwerger, A.L., and Munroe, J.S., 2021, InSAR-based characterization of rock glacier movement in the Uinta Mountains, Utah, USA: *The Cryosphere*, v. 15, p. 4823–4844, doi:10.5194/tc-15-4823-2021.
- Burns, W.J., and Madin, I.P., 2009, Protocol for Inventory Mapping of Landslide Deposits from Light Detection and Ranging (lidar) Imagery: Oregon Department of Geology and Mineral Industries Special Paper 42, 36 p.

- Calabro, M.D., Schmidt, D.A., and Roering, J.J., 2010, An examination of seasonal deformation at the Portuguese Bend landslide, southern California, using radar interferometry: *Journal of Geophysical Research: Earth Surface*, v. 115, doi:10.1029/2009JF001314.
- Camp, V., and Wells, R., 2021, The Case for a Long-Lived and Robust Yellowstone Hotspot: *GSA Today*, v. 31, p. 4–10, doi:10.1130/GSATG477A.1.
- Cardinali, M., Guzzetti, F., and Brabb, E.E., 1990, Preliminary maps showing landslide deposits and related features in New Mexico: U.S. Geological Survey 90–293, doi:10.3133/ofr90293.
- Case, J.C., 1990, Preliminary Landslide Maps: Wyoming State Geological Survey, <http://www.wrds.uwyo.edu/wrds/wsgs/hazards/landslides/lshome.html>.
- Chleborad, A.F., 1998, Use of Air Temperature Data to Anticipate the Onset of Snowmelt-Season Landslides: U.S. Geological Survey Open-File Report 98-124, 16 p., <https://pubs.usgs.gov/of/1998/0124/report.pdf> (accessed April 2023).
- Christiansen, R.L., 2001, The Quaternary and Pliocene Yellowstone Plateau Volcanic Field of Wyoming, Idaho, and Montana: Washington, United States Government Printing Office, *Geology of Yellowstone National Park G*, 145 p.
- Christiansen, R.L., Foulger, G.R., and Evans, J.R., 2002, Upper-mantle origin of the Yellowstone hotspot: *Geological Society of America Bulletin*, v. 114, p. 1245–1256, doi:10.1130/0016-7606(2002)114<1245:UMOOTY>2.0.CO;2.

- Coe, J.A., Baum, R.L., Allstadt, K.E., Kochevar, B.F., Schmitt, R.G., Morgan, M.L., White, J.L., Stratton, B.T., Hayashi, T.A., and Kean, J.W., 2016, Rock-avalanche dynamics revealed by large-scale field mapping and seismic signals at a highly mobile avalanche in the West Salt Creek valley, western Colorado: *Geosphere*, v. 12, p. 607–631, doi:10.1130/GES01265.1.
- Coe, J.A., Kean, J.W., Godt, J.W., Baum, R.L., Jones, E.S., Gochis, D.J., and Anderson, G.S., 2014, New insights into debris-flow hazards from an extraordinary event in the Colorado Front Range: *GSA Today*, v. 24, p. 4–10, doi:10.1130/GSATG214A.1.
- Cossart, E., Braucher, R., Fort, M., Bourlès, D.L., and Carcaillet, J., 2008, Slope instability in relation to glacial debuitressing in alpine areas (Upper Durance catchment, southeastern France): Evidence from field data and ¹⁰Be cosmic ray exposure ages: *Geomorphology*, v. 95, p. 3–26, doi:10.1016/j.geomorph.2006.12.022.
- Cruden, D.M., and Varnes, D.J., 1996, *Landslide Types and Processes*, in Turner, A.K. and Shuster, R.L. eds., *Landslides: Investigation and Mitigation*, Transportation Research Special Report 247, p. 36–75.
- ESRI, 2023a, Differences between point, line, and kernel density—ArcGIS Pro | Documentation:, <https://pro.arcgis.com/en/pro-app/latest/tool-reference/spatial-analyst/differences-between-point-line-and-kernel-density.htm> (accessed April 2023).
- ESRI, 2023b, How Kernel Density works—ArcGIS Pro | Documentation:, <https://pro.arcgis.com/en/pro-app/latest/tool-reference/spatial-analyst/how-kernel-density-works.htm> (accessed April 2023).

- ESRI, 2023c, How Spatial Autocorrelation (Global Moran's I) works—ArcGIS Pro | Documentation:, <https://pro.arcgis.com/en/pro-app/latest/tool-reference/spatial-statistics/h-how-spatial-autocorrelation-moran-s-i-spatial-st.htm> (accessed April 2023).
- Froude, M.J., and Petley, D.N., 2018, Global fatal landslide occurrence from 2004 to 2016: *Natural Hazards and Earth System Sciences*, v. 18, p. 2161–2181, doi:10.5194/nhess-18-2161-2018.
- Gardner, W.P., Susong, D.D., Solomon, D.K., and Heasler, H., 2010, Snowmelt hydrograph interpretation: Revealing watershed scale hydrologic characteristics of the Yellowstone volcanic plateau: *Journal of Hydrology*, v. 383, p. 209–222, doi:10.1016/j.jhydrol.2009.12.037.
- Gariano, S.L., and Guzzetti, F., 2016, Landslides in a changing climate: *Earth-Science Reviews*, v. 162, p. 227–252, doi:10.1016/j.earscirev.2016.08.011.
- Geertsema, M., Hungr, O., Schwab, J.W., and Evans, S.G., 2006, A large rockslide–debris avalanche in cohesive soil at Pink Mountain, northeastern British Columbia, Canada: *Engineering Geology*, v. 83, p. 64–75, doi:10.1016/j.enggeo.2005.06.025.
- Godt, J.W., Wood, N.J., Pennaz, A.B., Dacey, C.M., Mirus, B.B., Schaefer, L.N., and Slaughter, S.L., 2022, National Strategy for Landslide Loss Reduction: United States Geological Survey Open-File Report Open-File Report 2022–1075, 36 p.
- Guzzetti, F., Mondini, A.C., Cardinali, M., Fiorucci, F., Santangelo, M., and Chang, K.-T., 2012, Landslide inventory maps: New tools for an old problem: *Earth-Science Reviews*, v. 112, p. 42–66, doi:10.1016/j.earscirev.2012.02.001.

- Hadley, J.D., 1964, Landslides and related phenomena accompanying the Hebgen Lake earthquake of August 17, 1959: U.S. Geological Survey Professional Paper 435-K.
- Handwerker, A.L., Huang, M.-H., Fielding, E.J., Booth, A.M., and Bürgmann, R., 2019, A shift from drought to extreme rainfall drives a stable landslide to catastrophic failure: *Scientific Reports*, v. 9, p. 1569, doi:10.1038/s41598-018-38300-0.
- Highland, L.M., and Bobrowsky, P., 2008, *The Landslide Handbook- A Guide to Understanding Landslides*: United States Geological Survey Circular Circular 1325, 129 p.
- Holm, K., Bovis, M., and Jakob, M., 2004, The landslide response of alpine basins to post-Little Ice Age glacial thinning and retreat in southwestern British Columbia: *Geomorphology*, v. 57, p. 201–216, doi:10.1016/S0169-555X(03)00103-X.
- Hostetler, S. et al., 2021, Greater Yellowstone climate assessment: past, present, and future climate change in greater Yellowstone watersheds: Montana State University, doi:10.15788/GYCA2021.
- Hungr, O., Evans, S., Bovis, M., and Hutchinson, J.N., 2001, Review of the classification of landslides of the flow type: *Environmental & Engineering Geoscience*, v. 7, p. 221–238, doi:10.2113/gsegeosci.7.3.221.
- Hungr, O., Leroueil, S., and Picarelli, L., 2014, The Varnes classification of landslide types, an update: *Landslides*, v. 11, p. 167–194, doi:10.1007/s10346-013-0436-y.
- Hungr, O., McDougall, S., Wise, M., and Cullen, M., 2008, Magnitude–frequency relationships of debris flows and debris avalanches in relation to slope relief: *Geomorphology*, v. 96, p. 355–365, doi:10.1016/j.geomorph.2007.03.020.

- Jones, J.N., Boulton, S.J., Bennett, G.L., Stokes, M., and Whitworth, M.R.Z., 2021, Temporal Variations in Landslide Distributions Following Extreme Events: Implications for Landslide Susceptibility Modeling: *Journal of Geophysical Research: Earth Surface*, v. 126, doi:10.1029/2021JF006067.
- Keefer, D., K., 1984, Landslides caused by earthquakes: *GSA Bulletin*, v. 95, p. 406–421, doi:10.1130/0016-7606(1984)95<406:LCBE>2.0.CO;2.
- Korup, O., Densmore, A.L., and Schlunegger, F., 2010, The role of landslides in mountain range evolution: *Geomorphology*, v. 120, p. 77–90, doi:10.1016/j.geomorph.2009.09.017.
- Lauknes, T.R., Piyush Shanker, A., Dehls, J.F., Zebker, H.A., Henderson, I.H.C., and Larsen, Y., 2010, Detailed rockslide mapping in northern Norway with small baseline and persistent scatterer interferometric SAR time series methods: *Remote Sensing of Environment*, v. 114, p. 2097–2109, doi:10.1016/j.rse.2010.04.015.
- Licciardi, J., Hurwitz, S., and Harrison, L., 2022, The Last Deglaciation of the Yellowstone Plateau: Timing and Implications: *Geological Society of America Abstracts with Programs*, v. 54, doi:10.1130/abs/2022AM-381490.
- Licciardi, J.M., and Pierce, K.L., 2018, History and dynamics of the Greater Yellowstone Glacial System during the last two glaciations: *Quaternary Science Reviews*, v. 200, p. 1–33, doi:10.1016/j.quascirev.2018.08.027.
- Love, J.D., and Keefer, W.R., 1975, *Geology of sedimentary rocks in southern Yellowstone National Park, Wyoming*: U.S. Geological Survey Professional Paper 729-D, <https://pubs.er.usgs.gov/publication/pp729D> (accessed March 2023).

- Mackey, B.H., and Roering, J.J., 2011, Sediment yield, spatial characteristics, and the long-term evolution of active earthflows determined from airborne LiDAR and historical aerial photographs, Eel River, California: *Geological Society of America Bulletin*, p. 17.
- Marc, O., Gosset, M., Saito, H., Uchida, T., and Malet, J.-P., 2019, Spatial Patterns of Storm-Induced Landslides and Their Relation to Rainfall Anomaly Maps: *Geophysical Research Letters*, v. 46, p. 11167–11177, doi:10.1029/2019GL083173.
- Montgomery, D.R., Schmidt, K.M., Greenberg, H.M., and Dietrich, W.E., 2000, Forest clearing and regional landsliding: *Geology*, v. 28, p. 311–314.
- Morgan, L., Shanks, W.C.P., Lowenstern, J., Farrell, J., and Robinson, J., 2017, *Geologic Field-Trip Guide to the Volcanic and Hydrothermal Landscape of the Yellowstone Plateau: U.S. Geological Survey Scientific Investigations Report Scientific Investigations Report 2017-5022-P*.
- NPS, 2020a, DataStore - Digital Geologic-GIS Map of the Yellowstone National Park and Vicinity, Wyoming, Montana and Idaho (NPS, GRD, GRI, YELL, YELL digital map) adapted from U.S. Geological Survey maps by Christiansen, Blank, Prostka, Smedes, Pierce, the U.S. Geological Survey, Elliot, Nelson, Wahl, Witkind, Love and others (1956 to 2007), and a Montana Bureau of Mines and Geology map by Berg, Lonn and Locke (1999):, <https://irma.nps.gov/DataStore/Reference/Profile/1044842> (accessed April 2023).

- NPS, 2020b, DataStore - Digital Surficial Geologic-GIS Map of Yellowstone National Park and Vicinity, Wyoming, Montana and Idaho (NPS, GRD, GRI, YELL, YELL_surficial digital map) adapted from U.S. Geological Survey maps by Richmond (1973, 1974, 1977), Pierce (1973, 1974), Richmond and Waldrop (1972, 1975), Waldrop (1975), Richmond and Pierce (1971, 1972), Waldrop and Pierce (1975) and the U.S. Geological Survey (1972):, <https://irma.nps.gov/DataStore/Reference/Profile/1044651> (accessed April 2023).
- Paguican, E.M.R., van Wyk de Vries, B., and Lagmay, A.M.F., 2014, Hummocks: how they form and how they evolve in rockslide-debris avalanches: *Landslides*, v. 11, p. 67–80, doi:10.1007/s10346-012-0368-y.
- Parise, M., and Cannon, S.H., 2012, Wildfire impacts on the processes that generate debris flows in burned watersheds: *Natural Hazards*, v. 61, p. 217–227, doi:10.1007/s11069-011-9769-9.
- Pierce, K.L., 1979, History and dynamics of glaciation in the northern Yellowstone National Park area: Professional Paper, doi:10.3133/pp729F.
- Pierce, K.L., 1973, Surficial geologic map of the Mount Holmes quadrangle and parts of the Tepee Creek, Crown Butte, and Miner quadrangles, Yellowstone National Park, Wyoming and Montana: IMAP Report 640, doi:10.3133/i640.
- Pierce, K.L., and Morgan, L.A., 2009, Is the track of the Yellowstone hotspot driven by a deep mantle plume? — Review of volcanism, faulting, and uplift in light of new data: *Journal of Volcanology and Geothermal Research*, v. 188, p. 1–25, doi:10.1016/j.jvolgeores.2009.07.009.

- Roering, J.J., Kirchner, J.W., and Dietrich, W.E., 2005, Characterizing structural and lithologic controls on deep-seated landsliding: Implications for topographic relief and landscape evolution in the Oregon Coast Range, USA: *Geological Society of America Bulletin*, v. 117, p. 654, doi:10.1130/B25567.1.
- Roering, J.J., Mackey, B.H., Marshall, J.A., Sweeney, K.E., Deligne, N.I., Booth, A.M., Handwerger, A.L., and Cerovski-Darriau, C., 2013, ‘You are HERE’: Connecting the dots with airborne lidar for geomorphic fieldwork: *Geomorphology*, v. 200, p. 172–183, doi:10.1016/j.geomorph.2013.04.009.
- Ruppel, E.T., 1972, Geology of pre-Tertiary rocks in the northern part of Yellowstone National Park, Wyoming: U.S. Geological Survey Professional Paper USGS Numbered Series 729-A, doi:10.3133/pp729A.
- Shelly, D.R., Hill, D.P., Massin, F., Farrell, J., Smith, R.B., and Taira, T., 2013, A fluid-driven earthquake swarm on the margin of the Yellowstone caldera: *Journal of Geophysical Research: Solid Earth*, v. 118, p. 4872–4886, doi:10.1002/jgrb.50362.
- Slaughter, S.L., Mickelson, K.A., Biel, A., and Contreras, T.A., 2017, Protocol for Landslide Inventory Mapping from LiDAR Data in Washington State: *Washington Geological Survey Bulletin* 82, 35 p.
- Smedes, H., and Prostka, H., 1972, Stratigraphic Framework of the Absaroka Volcanic Supergroup in the Yellowstone National Park Region: United States Geological Survey Geological Survey Professional Paper 729–C.
- Tanyaş, H., Kirschbaum, D., Görüm, T., van Westen, C.J., Tang, C., and Lombardo, L., 2021, A closer look at factors governing landslide recovery time in post-seismic periods: *Geomorphology*, v. 391, p. 107912, doi:10.1016/j.geomorph.2021.107912.

- USGS, 1972, Geologic Map of Yellowstone National Park: U.S. Geological Survey
Miscellaneous Geologic Investigations I-711.
- Watkins, J.A., Ehlmann, B.L., and Yin, A., 2020, Spatiotemporal evolution, mineralogical composition, and transport mechanisms of long-runout landslides in Valles Marineris, Mars: *Icarus*, v. 350, p. 113836, doi:10.1016/j.icarus.2020.113836.
- Whalley, W.B., and Azizi, F., 2003, Rock glaciers and protalus landforms: Analogous forms and ice sources on Earth and Mars: *Journal of Geophysical Research: Planets*, v. 108, doi:10.1029/2002JE001864.
- Xu, Y., Schulz, W.H., Lu, Z., Kim, J., and Baxstrom, K., 2021, Geologic controls of slow-moving landslides near the US West Coast: *Landslides*, v. 18, p. 3353–3365, doi:10.1007/s10346-021-01732-3.
- Zellman, M.S., DuRoss, C.B., Thackray, G.D., Personius, S.F., Reitman, N.G., Mahan, S.A., and Brossy, C.C., 2020, Holocene Rupture History of the Central Teton Fault at Leigh Lake, Grand Teton National Park, Wyoming: *Bulletin of the Seismological Society of America*, v. 110, p. 67–82, doi:10.1785/0120190129.

3. Using InSAR to Identify Creeping Landslides in Yellowstone

3.1. Introduction

Landslides are masses of material that travel downslope at rates that range from extremely rapid (m/second) to extremely slow (mm/year) and these rates can fluctuate over time (Cruden and Varnes, 1996). Rapid landslides are incredibly destructive and are unpredictable and violent, making them difficult to measure in real time. Rapidly emplaced landslides break up hillslope material, likely creating conditions that are favorable for continuing gradual movement after an initial “catastrophic” failure. These slower creeping movements, on the order of mm to m per year, can persist for years, thus offering the opportunity to study the processes that drive movement (Lacroix et al., 2020). Continual deformation can also demand continuous upkeep of infrastructure such as roads, pipelines or other built features and indicate incipient reactivation and the potential for catastrophic failure (e.g., Šilhán, 2020), making the identification of slow-moving slope failures an important component of landslide hazard assessment.

Slow movements, or creep, occur on a variety of scales to move material down slopes. Surficial soil particles move extremely slowly simply under the influence of gravity (Deshpande et al., 2021) and cycles of volumetric particle expansion and contraction further mix and transport soil (Hung et al., 2014). High-relief slopes deform very slowly under the process of deep-seated gravitational slope deformation (DSGSD) where bedrock slowly collapses on a hillslope or mountain-slope scale, possibly as a consequence of glacial debuitressing (Crosta et al., 2013). Landslide creep, which is the focus of this study, occurs as masses of debris move downslope, often in response to hydrologic forcings (Handwerger et al., 2013).

Actively creeping landslides display a variety of kinematic behaviors linked to their dominant forcing mechanisms (Lacroix et al., 2020). Broad categories of movement may include

continuous displacement (e.g., Bekaert et al., 2020), episodic displacement linked to a specific triggering event (e.g., Bennett et al., 2016; Handwerger et al., 2019), or cyclical, seasonal displacement (e.g., Coe et al., 2003; Handwerger et al., 2022; Figure 3.1). Creep tends to occur in fractured, clay-rich, or other mechanically weak materials (Lacroix et al., 2020).

Interferometric Synthetic Aperture Radar (InSAR) is particularly useful for measuring creeping landslides as it can measure millimeter to centimeter-scale changes over large areas (Gabriel et al., 1989). A variety of previous studies have leveraged InSAR to study landslides and rock glaciers, creating inventories of active features and examining the temporal patterns of individual features and linking them to specific triggering conditions related to variations in seasonal precipitation patterns (e.g., Guzzetti et al., 2009; Barboux et al., 2014; Handwerger et al., 2015; Brencher et al., 2021; Cook et al., 2022).

Here, we use InSAR to investigate active landslides in Yellowstone National Park. This study takes advantage of our ~1800-feature LiDAR-derived inventory to compare all mappable landslide deposits to InSAR-identified patches of ground deformation. The combination of these two data sets provides a unique opportunity to investigate creep on features that may have been initially emplaced through rapid movement. With InSAR, we are able to both identify areas of creep and to investigate temporal patterns of that creep over a period of five years (2017-2021). We hypothesize that most of the LiDAR-mapped landslides are not moving; that moving landslides have characteristics that are distinct from non-moving landslides, and that individual slides may show different movement patterns over time as they reflect snapshots of the different combinations of triggering mechanisms that are present across the park.

3.2. Site Description

Yellowstone National Park rests on a broad, high-elevation plateau surrounded by the rugged Gallatin, Beartooth, and Absaroka Mountain Ranges in northwestern Wyoming. The plateau is the collapsed and infilled caldera of a massive volcanic hotspot that has migrated northeastward across North America over the last 17 Ma (Pierce and Morgan, 2009). The surrounding mountain ranges expose a diverse array of bedrock units that span most of North America's geologic history. The Quaternary caldera is underlain by thousands of cubic kilometers of rhyolite flows; thick tuff deposits of similar ages ring the caldera boundary (Christiansen, 2001). The most recent eruptions occurred at 2 Ma, 1.3 Ma, and 0.63 Ma. The Tertiary-age Absaroka Volcanic Supergroup, found mostly along the eastern side of the park, is made up of intrusive and extrusive igneous rock with interbedded sedimentary units, recording an earlier episode of volcanic activity (Smedes and Prostka, 1972). Mesozoic and Paleozoic sedimentary rocks form the Gallatin Range in the northwest and crop out in the south-central part of the park (Ruppel, 1972; Love and Keefer, 1975). Limited exposures of Precambrian metamorphic rocks are found to the north (Ruppel, 1972). During the Pleistocene, the Yellowstone Plateau hosted the largest ice cap south of Laurentia (Licciardi and Pierce, 2018). During the most recent glacial episode, known as the Pinedale glaciation, ice coalesced on the plateau ~22 ka. The ice cap retreated rapidly at ~13 ka (Licciardi et al., 2022). As ice flowed down valleys, over mountain ranges, and across plateaus, we assume that it largely eroded previous surficial deposits and features.

Yellowstone experiences a significant orographic precipitation effect as storms are channeled from the Pacific Ocean across the low-elevation Snake River Plain until they hit the higher-elevation plateau (Whitlock et al., 1995). Since the retreat of the Pinedale ice cap, the

park has experienced shifts between relatively cooler and wetter and warmer and drier climate patterns (Brown et al., 2021). Under the modern climate regime, Yellowstone receives 25-80 cm of precipitation annually, much of which falls as snow (Gardner et al., 2010; Licciardi and Pierce, 2018). Snow typically begins to accumulate in October and spring runoff begins in mid-April and continues through June. As the Earth's climate warms, overall precipitation is expected to increase and a greater proportion is expected to fall as rain and that seasonal hydrologic regime may change significantly (Hostetler et al., 2021).

The Yellowstone area is one of the most seismically active regions in the United States due to the combined influences of the volcanic hot spot, associated hydrothermal activity and Basin-and-Range extension. Swarms of generally low-magnitude earthquakes occur in the caldera area as fluids and magma move through the subsurface (Shelly et al., 2013). Large earthquakes have been recorded over the last several thousand years on Basin-and-Range-related faults adjacent to the Yellowstone Plateau (Hadley, 1964; Zellman et al., 2020).

Our recent inventory from 2020 LiDAR data mapped and classified over 1800 landslides and rock glaciers and found that lithology appears to exert an important control over the distribution of mass movement features throughout the park. Landslide deposits are almost entirely absent from the central plateau area, while they are disproportionately found on hillsides underlain by Mesozoic and Paleozoic sedimentary rocks and are pervasive within much of the Absaroka Volcanic Supergroup. These mapped deposits represent mostly the accumulation of landslides that occurred over the last ~13 ka. This study aims to identify actively deforming deposits and describe some of their movement characteristics. In future studies, this may shed some light on which deposits may pose risk to infrastructure and offer opportunities to explore how movement is affected by contemporary forcings.

3.3. Methods

3.3.1. Data Acquisition and InSAR Processing

We used the Alaska Satellite Facility's (ASF) on-demand processing (Hogenson et al., 2020) to generate Sentinel-1 interferograms to create a time series of activity between May 2017 and October 2021. Before 2017 or after 2021, limited numbers of SAR images impeded our ability to create a dense and redundant interferogram network. We processed data on both ascending- and descending-tracks, which provide two independent views of ground surface deformation.

To avoid issues related to snow cover, we chose shorter temporal baseline (12-60 days) interferograms within snow-free periods (mid-May through mid-October) and longer temporal baseline (~200-380 days) interferograms to span between the snowy seasons. We expected that high-coherence, shorter time-span interferograms would help to illuminate some intra-season patterns and that the longer interferograms enable us to create a continuous network that can be used to constrain inter-year displacement rates. We downloaded 371 interferograms from ascending track 122 (flying towards the north and looking towards the east), and 439 interferograms from descending track 100 (flying towards the south and looking towards the west). A full list of these interferograms is available as supplemental material. We used 10 looks in range and 2 looks in azimuth to create interferograms that have a pixel spacing of 40 m. Large water bodies (e.g., Yellowstone Lake, Heart Lake, and Shoshone Lake) were masked in individual interferograms as part of the HyP3 processing at the Alaska Satellite Facility.

We used Sentinel-1 data for this study because we can access a large volume of interferograms through ASF without requiring significant local computational resources. HyP3 interferograms are also well-integrated into the relatively user-friendly MintPy software, again

lowering the computational and expertise barriers to perform time series analysis. Because it is C-band, Sentinel-1 is not the most ideal sensor for this study, especially since it does not penetrate vegetation as well as an L-band sensor would. This drawback is dramatically outweighed by the temporal density of the data and its accessibility.

3.3.2. MintPy Velocity Inventory

We used the open-source Miami INsar Time-series software in Python (MintPy; Yunjun et al., 2019) to create displacement time series and velocity estimates for ascending and descending interferogram stacks. We applied a minimum coherence threshold of 0.3 to eliminate poor-quality interferograms and applied an ERA5 model for tropospheric correction using PyAPS software (Jolivet et al., 2014). We examined 6 different combinations of interferograms for both the ascending and descending tracks. The first combination resulted in a “superstack” that provided a continuous time series from May 2017 to October 2021 and combines all of the shorter- and longer-baseline interferograms. The other 5 time series datasets were broken into smaller time chunks, using only the shorter-baseline interferograms within individual snow-free periods to isolate effects of “seasonal” changes (Figure 3.2).

Visualizing the line-of-sight velocity maps in ESRI ArcGIS Pro, we created an inventory of active features by identifying high-velocity patches that overlap our LiDAR-based landslide inventory (Chapter 2). We defined a landslide “patch” as a group of at least 4 pixels (about 6400 m²) that showed a higher velocity than their surroundings, though most patches were composed of 10s-100s of elevated-velocity pixels. The subsiding Yellowstone caldera showed a clear velocity signal on the scale of 10s of kilometers, so it was easily excluded from our inventory.

The subsiding caldera may complicate the detection of any smaller landslide-motion patches within the region, but our lidar-based inventory shows very few landslides in this area.

Upon inspecting the velocity maps for each stack, we chose to create our movement inventory using the superstacks because they were the least noisy and the patches we identified in the superstack maps were generally consistent with those we saw in the seasonal maps. We created a polygon feature class that combined all patches from both the ascending and descending track velocity maps and used ESRI's Select By Location Tool to identify landslides from our previous inventory that overlapped with the velocity patches. We then inspected each of these moving landslide polygons to ensure that we were accurately matching movement patches with deposits. The final movement inventory contains the landslide deposits and rock glaciers, as previously identified from LiDAR, that show distinct movement patches in either the ascending or descending velocity maps, or both.

3.3.3. Time Series Analysis on Individual Features

From the velocity inventory, we selected three landslides for time series analysis. We chose these slides due to their clear velocity signal, relatively high coherence, mostly east or west aspect, and stable, high-coherence local reference points. We processed the full five-year superstack and each individual snow-free seasonal stack for each landslide, selecting local reference points and individually inspecting and removing individual poor-quality interferograms that were not automatically removed through the coherence-based network modification. We plotted the average absolute displacement in each stack of 9 pixels that were within the zone of movement within each landslide polygon, excluding any pixels that had a temporal coherence of less than 0.3. By plotting the absolute cumulative displacement values, we expect to see

continuously increasing displacement to indicate downslope movement. We averaged the same 9 pixels in each stack in order to make direct comparisons between their behavior on different time scales.

3.4. Results

3.4.1. Movement Inventory

3.4.1.1. Spatial Distribution

Of the ~1800 landslide deposits and rock glaciers we previously mapped using LiDAR, we identified 222 that were moving in the InSAR velocity maps. Though this subset makes up ~12% of the total count of landslides, the moving deposits represent 40% of the area of the entire inventory (Figure 3.3). Given the resolution of the SAR data, we may be slightly biased towards detecting larger area of movements, but this also suggests that larger, and likely thicker landslides are more likely to experience creep. The active landslides share a similar spatial distribution to the LiDAR-mapped landslides, occurring outside of the caldera and being clustered in the northwest, northeast, and south-central parts of the park. The mean centers of each inventory are about 3 km apart within our study area of about 10,000 km².

There are 5 high-velocity patches in the 5-year superstacks of both ascending and descending velocity maps that do not correlate to LiDAR-mapped landslide deposits. Many of these false-positive patches fall over areas that appear in satellite imagery as wetlands or hydrothermal areas that are too small to be included in the water mask during the HyP3 interferogram processing. Given the large number of active faults in Yellowstone, these patches may also represent small surface displacements or topographic or atmospheric errors that have not been fully corrected. They make up a very small percentage of all of the patches we mapped,

so we feel confident excluding them from our analysis and trusting that the patches we identify as landslides are actually landslides.

3.4.1.2. Type & Lithology Distribution

The movement inventory contains open-slope debris flows, complexes, slides, rock falls, and rock glaciers. We did not observe any creeping movement on channelized debris flow deposits and significantly less movement in slide deposits. Open-slope debris flows make up about 60% of both the LiDAR and the movement inventories (Figure 3.4). Complexes make up a greater proportion of the movement inventory than the LiDAR inventory. Rock falls and rock glaciers occupy similarly small proportions of both inventories. Much like the LiDAR inventory, Mesozoic and Paleozoic sedimentary rocks are the most common source lithology for creeping deposits (Figure 3.5). The other lithologies show a similar distribution throughout both inventories.

3.4.2. Time Series of Motion

3.4.2.1. Lava Butte

Lava Butte is located in the very northwest corner of the park (Figure 3.3A); the butte forms a resistant cliff topped by Huckleberry Ridge Tuff that overlies Jurassic and Cretaceous-aged sedimentary rocks (USGS, 1972). We mapped a dozen open-slope debris flows sourced from the resistant cliff and focus our displacement measurements on one of these. Displacement on the Lava Butte landslide is linearly continuous through the snow-free season and there appears to be no motion during the winter (Figure 3.6). 2018 seems to have a slightly higher velocity than the other years, though interferograms for that year were only available through

July. In the displacement time series from stacks of individual years, each year has a similar, nearly linear displacement rate, with slightly faster velocities at the beginning of each season. 2018 also appears to have a faster overall velocity in the seasonal stack. This result is similar to our seasonal displacement time series in Figure 3.1C.

3.4.2.2. Silvergate

Silvergate is a cluster of open-slope debris flows just south of Mammoth Hot Springs (Figure 3.3A). These landslide deposits are sourced from cliffs composed of travertine overlying Jurassic and Cretaceous-aged sedimentary rocks (USGS, 1972) and are composed of extremely large blocks ~3m in diameter. The superstack time series shows a significant episode of displacement in early 2018 with displacement becoming increasingly variable through 2021 (Figure 3.6). In the displacement time series from individual years, we see highly variable displacement patterns and the episode in 2018 does not stand out. Because several years show considerable negative displacement, we suspect that we have not eliminated all noise sources from this data set. This result is similar to a combination of our continuous and event-based time series in Figure 3.1A and B.

3.4.2.3. Flagg Ranch

Flagg Ranch is located near the south entrance of the park (Figure 3.3A). The cluster of complex-type (slide/flow) landslide deposits are sourced from cliffs topped by Huckleberry Ridge Tuff overlying Cretaceous-aged sedimentary rocks (Love, 1974). The superstack time series shows a generally consistent rate of displacement with an increase in displacement in early 2021 (Figure 3.6). The displacement time series from individual years show a more consistent,

mostly linear accumulation of displacement through each snow-free season that is slightly faster at the beginning of each season. Velocity reaches nearly zero at the end of the 2021 season. The superstack shows a much greater total displacement than what we might estimate from the seasonal stacks, suggesting that there may be significant motion between the snow-free periods. This result is similar to our continuous time series in Figure 3.1A.

3.5. Discussion

3.5.1. LiDAR Inventory vs. InSAR Inventory

Though it is composed of substantially fewer individual deposits, the spatial, movement type, and lithologic characteristics of the InSAR movement inventory are very similar to the complete LiDAR landslide inventory. We do not see creep on any channelized debris flow deposits, which is to be expected due to their mode of emplacement. Channelized debris flows deposits tend to occur as discrete depositional events on the timescale of hours to days and are unlikely to have saturated basal planes or thick deposits required for creep (Hung et al., 2001). Additionally, the LiDAR inventory does contain 178 deposits that are smaller than we expect to be able to detect with InSAR; however, these deposits represent less than 1% of the area of the total inventory so we are confident that InSAR measurements were generally able to characterize the creep activity LiDAR inventory.

Surprisingly, the actively creeping deposits were not readily distinguishable from all the deposits in the LiDAR inventory. We visited ~40 of the LiDAR-mapped landslide deposits in the field and were readily able to identify signs of activity on some of them (which were subsequently identified in the InSAR inventory) including fresh tension cracks, split trees, and freshly exposed portions of head scarps. Future work could include a more systematic

comparison of roughness or other topographic characteristics of the InSAR inventory in order to identify any unique attributes of the actively creeping deposits. On the other hand, perhaps the exceptional preservation of landslides on the Yellowstone landscape fundamentally limits the unique topographic expression of the active landslides.

With 40% of the area of the LiDAR inventory represented in ~200 creeping deposits, our InSAR results suggest that creeping movement is more common in the largest landslide deposits. The large landslide deposits throughout the park are characterized by features that suggest rapid initial failure, including self-formed levees, hummocks, and compression ridges. We suspect that characteristics of these deposits, as distinct from undisturbed ground, facilitate creeping movement for an extended period after the initial rapid emplacement. These initial failures break up a large amount of material, which generates a thick deposit, changes local slope angles and infiltration capabilities, and creates a subsurface plane of weakness that may respond more readily to perturbations such as storms events, or fluctuations in atmospheric pressure than undisturbed hillslopes do (Coe et al., 2003; Schulz et al., 2009; Handwerger et al., 2019). Many of these large deposits also terminate into or near small stream channels where continual erosion may also prevent the deposit from stabilizing completely. With many creeping landslides and a variety of possible perturbations (especially rapid snowmelt, storm events, and earthquakes) Yellowstone is an ideal natural laboratory to study mechanisms driving creeping movement on landslides.

3.5.2. Time Series Interpretations

In the three different displacement time series we saw three different movement patterns. We characterized Lava Butte as seasonal displacement with little movement between the end of

one snow-free period and the next. Silvergate exhibits an event-like displacement, marked by a jump in displacement in 2018. This jump is not obvious in the seasonal stacks; the displacement may be too small to measure in the shorter temporal baseline interferograms. Flagg Ranch demonstrates a more consistent rate of displacement throughout the study period, though measurement on this slide is particularly impeded by our inability to measure displacement while there is snow on the ground. At Flagg Ranch, we cannot be sure if movement between snow-free periods is continuous or if the landslide stabilizes like Lava Butte appears to. Smaller displacements in the seasonal stacks compared to the superstack suggest that motion does occur between snow-free periods on Flagg Ranch landslide.

We suspect that these different time series patterns relate to different movement mechanisms or triggers on these three features. Yellowstone contains abundant potential landslide triggers, including earthquakes, seasonal snowmelt, and intense storms. Some or all of these landslides may have been creeping for thousands of years, responding and adjusting to a variety of different conditions; our work highlights the importance of examining multiple temporal scales to assess movement patterns and processes, because those different scales show different movement patterns.

The movement on these features may also be occurring at different depths, related to the movement mechanisms, which are then again perturbed by different forcings. The InSAR measurements show only that the ground surface is moving; this movement may be related to shallow soil creep, gradual deformation of the landslide body, movement along a basal plane of weakness, or a combination of some or all of those mechanisms. Because this movement is concentrated on landslide deposits, which likely contain both readily deformable material and

basal planes of weakness, we strongly suspect that these mechanisms are in play, but more work is needed to determine how this movement occurs.

Other slides throughout the inventory showed generally similar time series patterns though we did not create careful analyses for each. We suspect that the many creeping landslides throughout the park may be grouped together by their displacement behavior and the spatial distribution of those groups may shed light on the processes driving those different rates of movement. This analysis likely requires different displacement measurements; we were unable to find stable local reference points for other landslide features in the interferogram stacks we used here.

3.5.3. Hazard/Risk Implications

This InSAR-based inventory provides an enhanced identification of landslide hazards throughout Yellowstone, complementing the LiDAR-based inventory. Creeping movement offers a different risk to infrastructure than rapid movement, but not an inconsequential one. The creeping deposits we identified are strong candidates for continued monitoring. Slow movement may be a precursor to more rapid failure; continual monitoring may be able to identify accelerations and offer an early warning to catastrophic events.

3.5.4. Limitations and Future Opportunities

This study likely underestimates the number of active landslides for several reasons. We acknowledge that there may be some bias in both the InSAR and LiDAR inventories towards larger deposits. Because the Sentinel-1 satellite flies on a north-south track and “looks” perpendicular to the right of its flight path, it is essentially blind to motion that parallels its flight

track. Our LiDAR-mapped landslide deposits occupy all hillslope aspects so we are likely underestimating the number of actively creeping landslides because the satellite cannot capture their motion. We did recognize some creeping landslides with generally north and south aspects, though there were far fewer of these landslides in the movement inventory than in the LiDAR inventory.

Additionally, we suspect that there are some errors related to coherence issues due to atmospheric delays and vegetation cover; however, because almost all of the movement patches we observed overlapped with clearly visible landslide deposits, we do not believe these coherence issues hindered our ability to detect active landslides. We mitigate these sources of error as much as possible by creating a well-connected and highly redundant interferogram network containing interferograms with a diversity of temporal baselines (the superstack and the seasonal stacks), applying a tropospheric delay correction, and choosing local stable reference points for our analysis of individual features.

Unwrapping errors in the long temporal baseline interferograms may also be affecting the measured movement rates in our superstack time series and may obscure our ability to identify some active movements, especially on the Lava Butte landslide. In the seasonal stacks, we see much larger displacements than in the superstack. These landslides may be moving faster than we can accurately measure in long-temporal baseline interferograms (200-380 days) with C-band InSAR, leading to phase aliasing (Manconi, 2021). This finding highlights the importance of examining subsets of interferogram stacks in order to better characterize motion. This detection issue may also be overcome by using L-band SAR data; the launch of the NISAR satellite (which uses L-band SAR, can measure displacements of about 12 cm in individual interferograms, compared to C-band which can measure about 5 cm) presents an exciting opportunity for future

analysis of these landslides (Rosen et al., 2017). The range of displacements we observed over Yellowstone suggests that combining L-band and C-band measurements over the same area may have the capacity to illuminate patterns on different scales.

3.6. Conclusion

In this study, we used maps of InSAR velocity estimates to compile an inventory of actively creeping landslides in Yellowstone National Park between May 2017 and October 2021. We compared this movement inventory to ~1800 landslide deposits that we identified using a 2020 LiDAR dataset and found that ~200 of these deposits were actively creeping. The active deposits represent 40% of the aerial extent of the LiDAR inventory and share a very similar spatial distribution, as well as movement types and underlying lithologic characteristics. Though rapid emplacement events are largely responsible for the landforms we characterize as landslide deposits, these deposits appear to remain unstable over time, with implications for hazard and risk assessment. This study is a brief snapshot into the lifetime of possibly thousands of years of creeping movement on these features, and highlights the persistence of slope instability, especially on large mass movements as observed in Yellowstone.

Detailed time series analysis of three individual landslides revealed three distinct movement behaviors over time: continuous, event-based, and seasonal. We suspect that these behaviors are linked to specific deformation processes and triggers. Future work may identify those triggers, providing important insights into the processes driving creep and variations in landslide movement over time. This study forces an evaluation of our assumptions of landform stability and threshold-based transport rules.

3.7. Figures

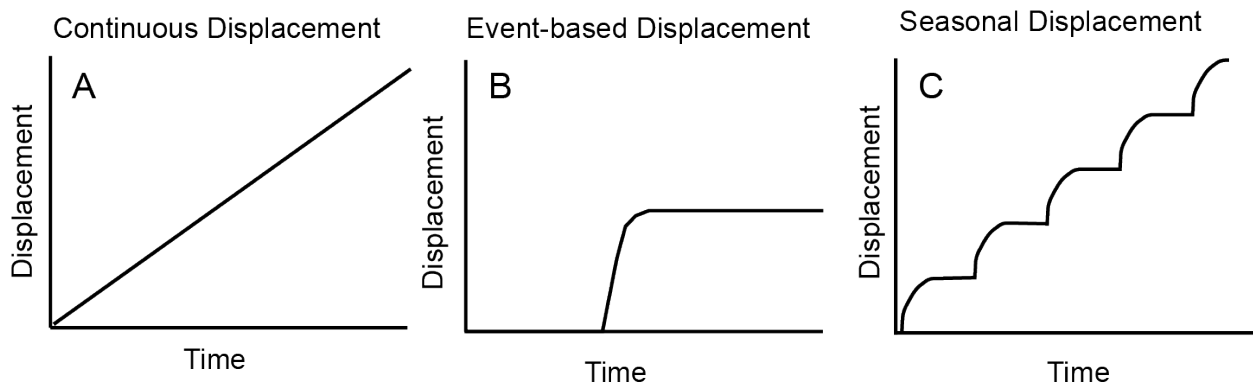


Figure 3.1. Hypothetical time series graphs of landslide movement. We expect landslides with different triggering mechanisms or deformation processes to exhibit different temporal patterns in movement. A) Continuous displacement that occurs at a consistent rate through the observed time period. B) Displacement is concentrated over a very short time period. C) Seasonal displacement showing cycles of acceleration, deceleration, and dormancy.

Schematic configuration of interferogram network

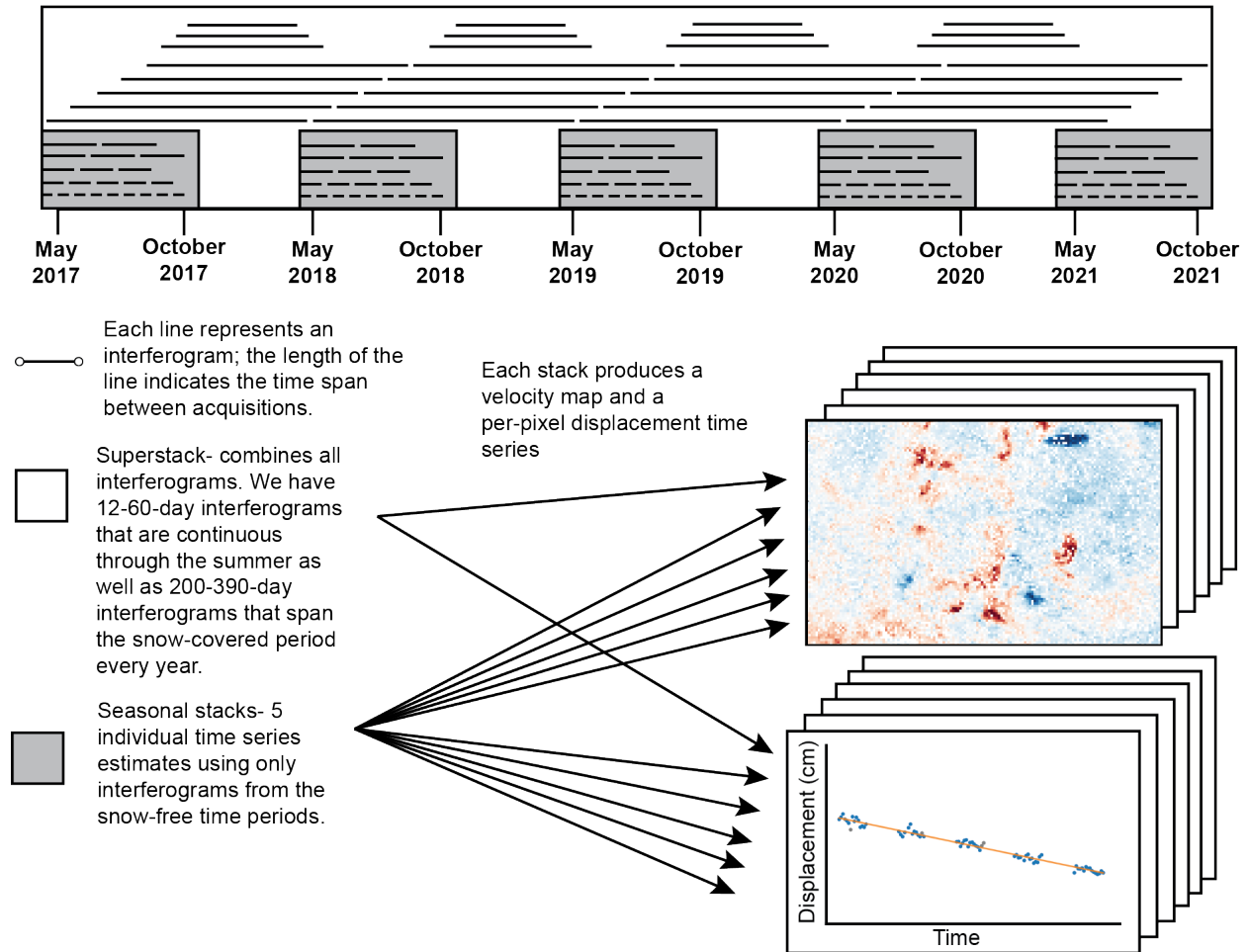


Figure 3.2. Conceptualization of the interferogram networks used in this study. We compiled three general types of interferograms: (1) those with relatively short temporal baselines (12-60 days) that formed continuous networks across the snow-free seasons for an individual year, (2) those with ~200-day temporal baselines that spanned the shortest time periods between snow-free seasons, and (3) ~365-day temporal baselines that span full years from snow-free season to snow-free season. For each ascending and descending frame, we processed 6 different configurations of interferograms to produce velocity maps and displacement time series. The “superstack” used all of the interferograms spanning our entire 5-year study period; the ascending frame started with 371 individual interferograms and each descending frame started with 439 interferograms. The seasonal stacks, one for each year, only used the short-baseline interferograms. Each of the seasonal stacks started with 20-60 individual interferograms.

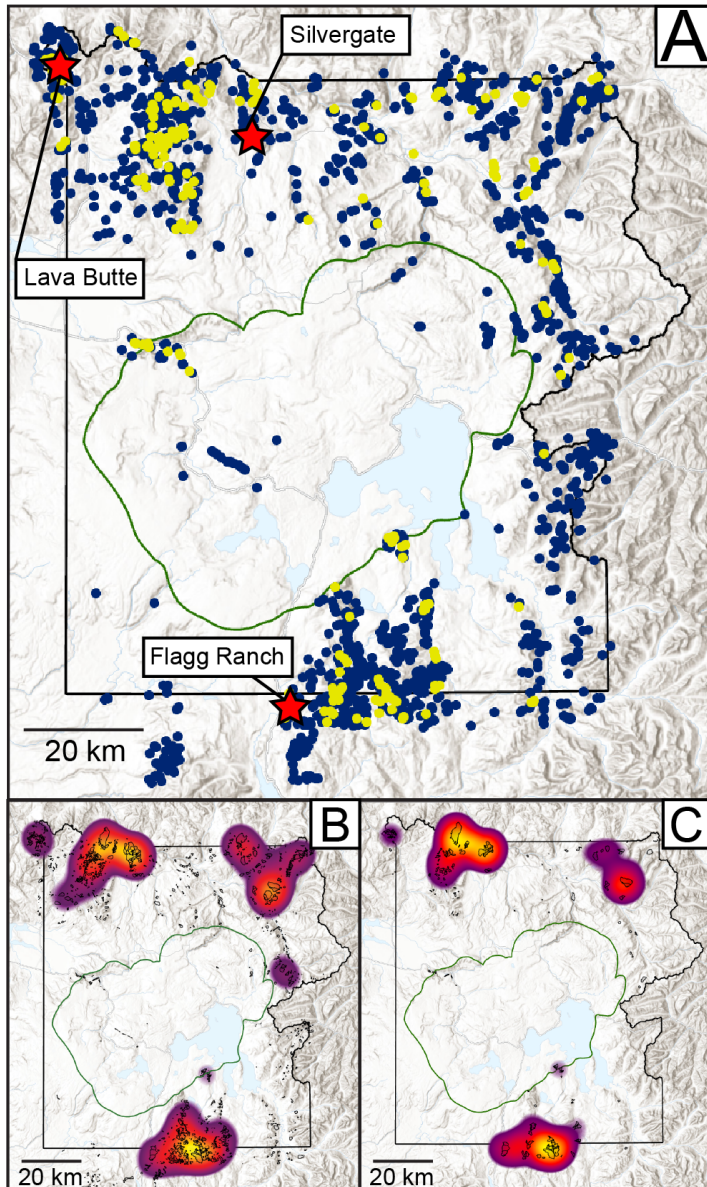


Figure 3.3. Parkwide landslide distribution. A) Points represent the centroids of all landslide deposits mapped from LiDAR (blue) and moving landslide deposits mapped using InSAR velocity maps (yellow). Locations of landslides selected for time series analysis in Figure 3.6 are marked by red stars. B) Kernel density heat map of all LiDAR-mapped landslide deposits, weighted by area; yellow indicates dense clusters of larger features. Small black polygons are mapped deposits. C) Heat map of all InSAR-mapped active landslide deposits. In all three maps, the boundary of Yellowstone National Park is shown as a large black polygon, the outline of the youngest caldera is a green oval in the center of the park.

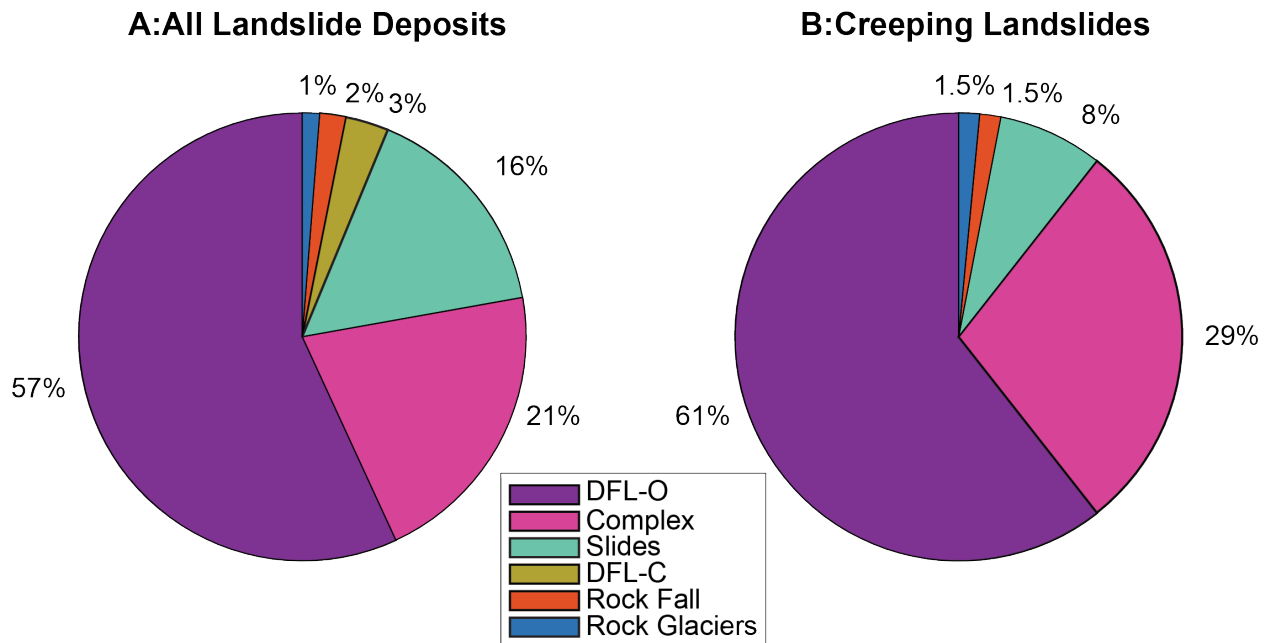


Figure 3.4. Pie charts of the % area of landslide types in each inventory. DFL-O: open-slope debris flow. DFL-C: channelized debris flow. (A) is the LiDAR-based inventory and (B) is the InSAR-based inventory of creeping landslides. Open-slope debris flows make up nearly 60% of both inventories. The major difference between the two inventories is that there are no channelized debris flow deposits in the InSAR inventory and complexes are more prevalent in the InSAR inventory.

Comparison of Simplified Lithologies Between Inventories

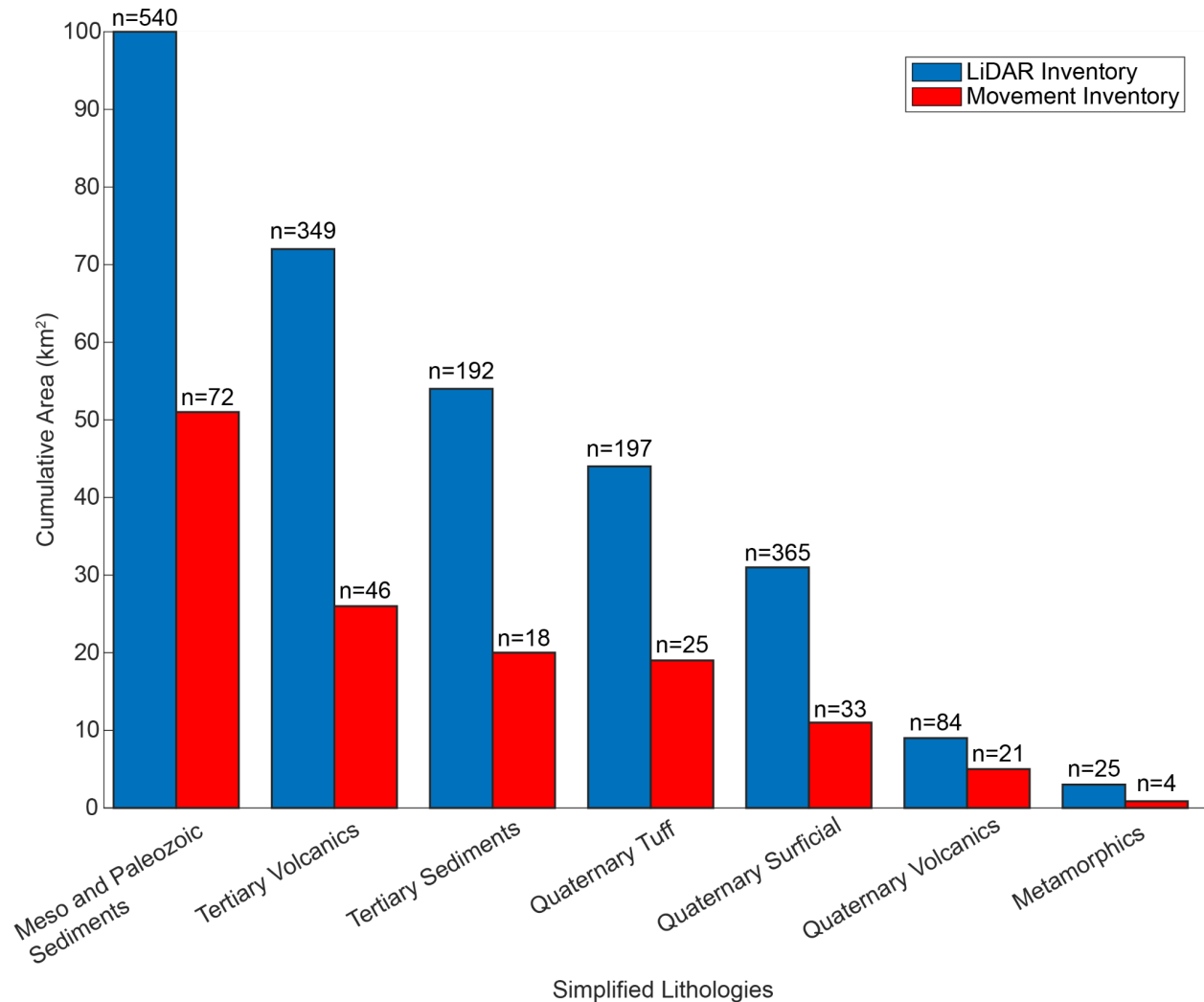


Figure 3.5. Bar plot showing the lithology of LiDAR-identified deposits (blue) and InSAR-identified creeping deposits (red). Quantities are reported in cumulative area, counts refer to the number of deposits in each category. Several mapped landslides were located outside of the boundary of the geologic map and are not included in this chart.

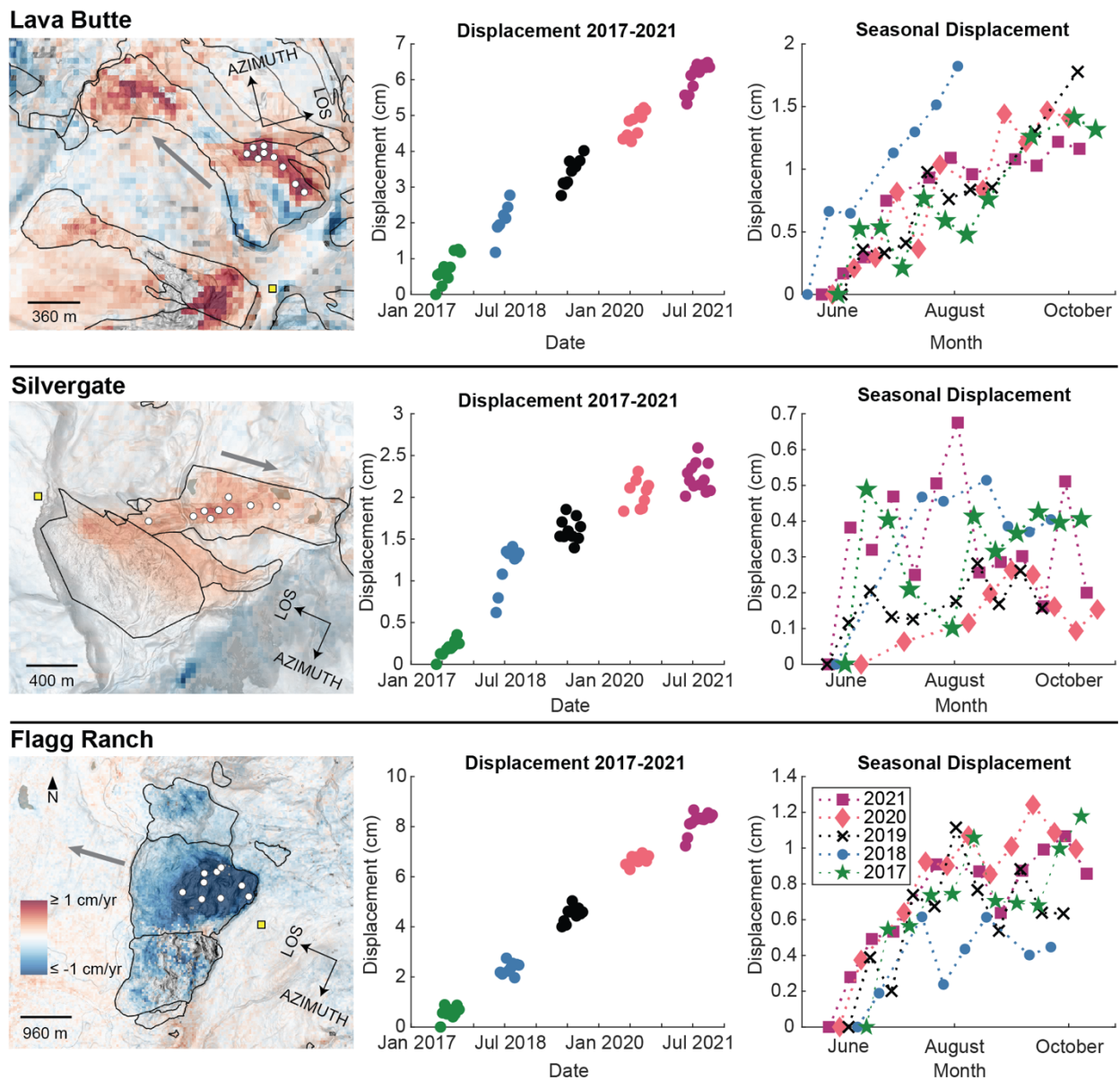


Figure 3.6. Analysis of kinematics at three representative landslides identified on Figure 3.3. Maps show superstack line-of-sight velocity maps with a yellow box marking the reference pixel. White points show pixels used to generate time series plots. Grey arrows indicate direction expected for downslope movement. Note the spatial heterogeneity in velocity within landslide polygons. Pixels with a temporal coherence of less than 0.3 are transparent. Time series for Lava Butte, Silvergate and Flagg Ranch denote seasonal, event-based, and continuous displacement, respectively, as defined in Figure 3.1. Note that displacement axes all have different scales.

3.8. References

- Barboux, C., Delaloye, R., and Lambiel, C., 2014, Inventorying slope movements in an Alpine environment using InSAR: *Earth Surface Processes and Landforms*, v. 39, p. 2087–2099, doi:10.1002/esp.3603.
- Bekaert, D.P.S., Handwerger, A.L., Agram, P., and Kirschbaum, D.B., 2020, InSAR-based detection method for mapping and monitoring slow-moving landslides in remote regions with steep and mountainous terrain: An application to Nepal: *Remote Sensing of Environment*, v. 249, p. 111983, doi:10.1016/j.rse.2020.111983.
- Bennett, G.L., Roering, J.J., Mackey, B.H., Handwerger, A.L., Schmidt, D.A., and Guillod, B.P., 2016, Historic drought puts the brakes on earthflows in Northern California: *Drought Puts Breaks on Earthflows: Geophysical Research Letters*, v. 43, p. 5725–5731, doi:10.1002/2016GL068378.
- Booth, A.M., LaHusen, S.R., Duvall, A.R., and Montgomery, D.R., 2017, Holocene history of deep-seated landsliding in the North Fork Stillaguamish River valley from surface roughness analysis, radiocarbon dating, and numerical landscape evolution modeling: *Journal of Geophysical Research: Earth Surface*, v. 122, p. 456–472, doi:10.1002/2016JF003934.
- Brencher, G., Handwerger, A.L., and Munroe, J.S., 2021, InSAR-based characterization of rock glacier movement in the Uinta Mountains, Utah, USA: *The Cryosphere*, v. 15, p. 4823–4844, doi:10.5194/tc-15-4823-2021.
- Brown, S.R. et al., 2021, Multi-proxy record of Holocene paleoenvironmental conditions from Yellowstone Lake, Wyoming, USA: *Quaternary Science Reviews*, v. 274, p. 107275, doi:10.1016/j.quascirev.2021.107275.
- Christiansen, R.L., 2001, The Quaternary and Pliocene Yellowstone Plateau Volcanic Field of

- Wyoming, Idaho, and Montana: Washington, United States Government Printing Office, Geology of Yellowstone National Park G, 145 p.
- Coe, J.A., Ellis, W.L., Godt, J.W., Savage, W.Z., Savage, J.E., Michael, J.A., Kibler, J.D., Powers, P.S., Lidke, D.J., and Debray, S., 2003, Seasonal movement of the Slumgullion landslide determined from Global Positioning System surveys and field instrumentation, July 1998–March 2002: *Engineering Geology*, v. 68, p. 67–101, doi:10.1016/S0013-7952(02)00199-0.
- Cook, M.E., Brook, M.S., Hamling, I.J., Cave, M., Tunncliffe, J.F., Holley, R., and Alama, D.J., 2022, Engineering geomorphological and InSAR investigation of an urban landslide, Gisborne, New Zealand: *Landslides*, v. 19, p. 2423–2437, doi:10.1007/s10346-022-01938-z.
- Crosta, G.B., Frattini, P., and Agliardi, F., 2013, Deep seated gravitational slope deformations in the European Alps: *Tectonophysics*, v. 605, p. 13–33, doi:10.1016/j.tecto.2013.04.028.
- Cruden, D.M., and Varnes, D.J., 1996, *Landslide Types and Processes*, in Turner, A.K. and Shuster, R.L. eds., *Landslides: Investigation and Mitigation*, Transportation Research Special Report 247, p. 36–75.
- Deshpande, N.S., Furbish, D.J., Arratia, P.E., and Jerolmack, D.J., 2021, The perpetual fragility of creeping hillslopes: *Nature Communications*, v. 12, p. 3909, doi:10.1038/s41467-021-23979-z.
- Gabriel, A.K., Goldstein, R.M., and Zebker, H.A., 1989, Mapping small elevation changes over large areas: Differential radar interferometry: *Journal of Geophysical Research*, v. 94, p. 9183, doi:10.1029/JB094iB07p09183.

- Gardner, W.P., Susong, D.D., Solomon, D.K., and Heasler, H., 2010, Snowmelt hydrograph interpretation: Revealing watershed scale hydrologic characteristics of the Yellowstone volcanic plateau: *Journal of Hydrology*, v. 383, p. 209–222, doi:10.1016/j.jhydrol.2009.12.037.
- Guzzetti, F., Manunta, M., Ardizzone, F., Pepe, A., Cardinali, M., Zeni, G., Reichenbach, P., and Lanari, R., 2009, Analysis of Ground Deformation Detected Using the SBAS-InSAR Technique in Umbria, Central Italy: *Pure and Applied Geophysics*, v. 166, p. 1425–1459, doi:10.1007/s00024-009-0491-4.
- Hadley, J.D., 1964, Landslides and related phenomena accompanying the Hebgen Lake earthquake of August 17, 1959: U.S. Geological Survey Professional Paper 435-K.
- Handwerger, A.L., Fielding, E.J., Huang, M., Bennett, G.L., Liang, C., and Schulz, W.H., 2019, Widespread Initiation, Reactivation, and Acceleration of Landslides in the Northern California Coast Ranges due to Extreme Rainfall: *Journal of Geophysical Research: Earth Surface*, v. 124, p. 1782–1797, doi:10.1029/2019JF005035.
- Handwerger, A.L., Fielding, E.J., Sangha, S.S., and Bekaert, D.P.S., 2022, Landslide Sensitivity and Response to Precipitation Changes in Wet and Dry Climates: *Geophysical Research Letters*, v. 49, p. e2022GL099499, doi:10.1029/2022GL099499.
- Handwerger, A.L., Roering, J.J., and Schmidt, D.A., 2013, Controls on the seasonal deformation of slow-moving landslides: *Earth and Planetary Science Letters*, v. 377–378, p. 239–247, doi:10.1016/j.epsl.2013.06.047.
- Handwerger, A.L., Roering, J.J., Schmidt, D.A., and Rempel, A.W., 2015, Kinematics of earthflows in the Northern California Coast Ranges using satellite interferometry: *Geomorphology*, v. 246, p. 321–333, doi:10.1016/j.geomorph.2015.06.003.

- Hogenson, K. et al., 2020, Hybrid Pluggable Processing Pipeline (HyP3): A cloud-native infrastructure for generic processing of SAR data:, <https://doi.org/10.5281/zenodo.4646138>.
- Hostetler, S. et al., 2021, Greater Yellowstone climate assessment: past, present, and future climate change in greater Yellowstone watersheds: Montana State University, [doi:10.15788/GYCA2021](https://doi.org/10.15788/GYCA2021).
- Hungr, O., Evans, S., Bovis, M., and Hutchinson, J.N., 2001, Review of the classification of landslides of the flow type: *Environmental & Engineering Geoscience*, v. 7, p. 221–238, [doi:10.2113/gsegeosci.7.3.221](https://doi.org/10.2113/gsegeosci.7.3.221).
- Hungr, O., Leroueil, S., and Picarelli, L., 2014, The Varnes classification of landslide types, an update: *Landslides*, v. 11, p. 167–194, [doi:10.1007/s10346-013-0436-y](https://doi.org/10.1007/s10346-013-0436-y).
- Jolivet, R., Agram, P.S., Lin, N.Y., Simons, M., Doin, M.-P., Peltzer, G., and Li, Z., 2014, Improving InSAR geodesy using Global Atmospheric Models: *Journal of Geophysical Research: Solid Earth*, v. 119, p. 2324–2341, [doi:10.1002/2013JB010588](https://doi.org/10.1002/2013JB010588).
- Lacroix, P., Handwerger, A., and Bièvre, G., 2020, Life and death of slow-moving landslides: *Nature Reviews Earth & Environment*, v. 1, [doi:10.1038/s43017-020-0072-8](https://doi.org/10.1038/s43017-020-0072-8).
- Licciardi, J., Hurwitz, S., and Harrison, L., 2022, The Last Deglaciation of the Yellowstone Plateau: Timing and Implications: *Geological Society of America Abstracts with Programs*, v. 54, [doi:10.1130/abs/2022AM-381490](https://doi.org/10.1130/abs/2022AM-381490).
- Licciardi, J.M., and Pierce, K.L., 2018, History and dynamics of the Greater Yellowstone Glacial System during the last two glaciations: *Quaternary Science Reviews*, v. 200, p. 1–33, [doi:10.1016/j.quascirev.2018.08.027](https://doi.org/10.1016/j.quascirev.2018.08.027).
- Love, J.D., 1974, Geologic map of the south half of the Huckleberry Mountain quadrangle, Teton

- Country, Wyoming: U.S. Geological Survey Open-File Report OF-74-54.
- Love, J.D., and Keefer, W.R., 1975, Geology of sedimentary rocks in southern Yellowstone National Park, Wyoming: U.S. Geological Survey Professional Paper 729-D, <https://pubs.er.usgs.gov/publication/pp729D> (accessed March 2023).
- Manconi, A., 2021, How phase aliasing limits systematic space-borne DInSAR monitoring and failure forecast of alpine landslides: *Engineering Geology*, v. 287, p. 106094, doi:[10.1016/j.enggeo.2021.106094](https://doi.org/10.1016/j.enggeo.2021.106094).
- Pierce, K.L., and Morgan, L.A., 2009, Is the track of the Yellowstone hotspot driven by a deep mantle plume? — Review of volcanism, faulting, and uplift in light of new data: *Journal of Volcanology and Geothermal Research*, v. 188, p. 1–25, doi:[10.1016/j.jvolgeores.2009.07.009](https://doi.org/10.1016/j.jvolgeores.2009.07.009).
- Rosen, P.A., Kim, Y., Kumar, R., Misra, T., Bhan, R., and Sagi, V.R., 2017, Global persistent SAR sampling with the NASA-ISRO SAR (NISAR) mission, *in* 2017 IEEE Radar Conference (RadarConf), p. 0410–0414, doi:[10.1109/RADAR.2017.7944237](https://doi.org/10.1109/RADAR.2017.7944237).
- Ruppel, E.T., 1972, Geology of pre-Tertiary rocks in the northern part of Yellowstone National Park, Wyoming: U.S. Geological Survey Professional Paper USGS Numbered Series 729-A, doi:[10.3133/pp729A](https://doi.org/10.3133/pp729A).
- Schulz, W.H., Kean, J.W., and Wang, G., 2009, Landslide movement in southwest Colorado triggered by atmospheric tides: *Nature Geoscience*, v. 2, p. 863–866, doi:[10.1038/ngeo659](https://doi.org/10.1038/ngeo659).
- Shelly, D.R., Hill, D.P., Massin, F., Farrell, J., Smith, R.B., and Taira, T., 2013, A fluid-driven earthquake swarm on the margin of the Yellowstone caldera: *Journal of Geophysical Research: Solid Earth*, v. 118, p. 4872–4886, doi:[10.1002/jgrb.50362](https://doi.org/10.1002/jgrb.50362).

- Smedes, H., and Prostka, H., 1972, Stratigraphic Framework of the Absaroka Volcanic Supergroup in the Yellowstone National Park Region: United States Geological Survey Geological Survey Professional Paper 729–C.
- USGS, 1972, Geologic Map of Yellowstone National Park: U.S. Geological Survey Miscellaneous Geologic Investigations I-711.
- Whitlock, C., Bartlein, P.J., and Van Norman, K.J., 1995, Stability of Holocene Climate Regimes in the Yellowstone Region: *Quaternary Research*, v. 43, p. 433–436, doi:[10.1006/qres.1995.1049](https://doi.org/10.1006/qres.1995.1049).
- Yunjun, Z., Fattahi, H., and Amelung, F., 2019, Small baseline InSAR time series analysis: Unwrapping error correction and noise reduction: *Computers & Geosciences*, v. 133, p. 104331, doi:[10.1016/j.cageo.2019.104331](https://doi.org/10.1016/j.cageo.2019.104331).
- Zellman, M.S., DuRoss, C.B., Thackray, G.D., Personius, S.F., Reitman, N.G., Mahan, S.A., and Brossy, C.C., 2020, Holocene Rupture History of the Central Teton Fault at Leigh Lake, Grand Teton National Park, Wyoming: *Bulletin of the Seismological Society of America*, v. 110, p. 67–82, doi:[10.1785/0120190129](https://doi.org/10.1785/0120190129).

4. Conclusion

4.1. Summary

We created a 1:4000-scale inventory of landslide deposits and rock glaciers in Yellowstone National Park. The inventory contains over 1800 features, documents their style of failure, and notes the underlying bedrock lithology. We found that almost all landslides in the park have occurred outside of the most recent caldera and that Mesozoic and Paleozoic sedimentary rocks represent a disproportionate fraction of the bedrock underlying these deposits. We suspect that lithology exerts a significant control over the location of landslide deposits on a park-wide scale; mass movements exploit contacts between rock types, clay layers, and bedding planes that are not present in the relatively homogenous caldera area.

We used InSAR to create surface velocity maps of the entire park between May 2017 and October 2021. Compared against the LiDAR-map of 1800 landslide deposits, the InSAR map showed that 222 of these deposits are actively creeping. These creeping deposits represent 40% of the total area of mapped landslide deposits, suggesting that creep generally occurs on the larger deposits in the inventory. These larger deposits may remain more unstable over time than smaller ones; they may be more sensitive to continued perturbation, and being inherently unstable, they may be more susceptible to future movement. We also found that these deposits do not necessarily creep consistently, but experience both cyclical and episodic periods of acceleration, which we suspect are indicative of their failure mechanisms and external triggering factors.

4.2. Limitations

One of the greatest limitations to this study is that we are using a static measurement (i.e. a 2020 LiDAR DEM) to characterize what we have come to realize are temporally complex, dynamic landforms. Many, if not most of the landslide deposits we mapped represent multiple generations of movement, either through creep or large-scale reactivation. Representing those movements with a single polygon seems to oversimplify their complexity; but it is rarely possible to properly identify all of the boundaries of overlapping features. Intermediate morphologies and variations in roughness suggest that these landforms are evolving over time and that we are just getting a small glimpse of their evolution. We do not have information about the initiation date of any of these landslides; assuming that they are post-Pinedale gives us a general maximum age, but even that is a broad simplification and does not acknowledge the dynamic nature of the ice cap or address corners of the park that did not experience ice (Licciardi and Pierce, 2018).

This study also has a very specific scope; we were unable to characterize most of the topographic attributes of our mapped landslide deposits and focused on interpreting park-scale patterns in overall distribution and lithology. These polygons could be used to extract a myriad of other topographic and other spatial characteristics. Here we opted for a simplified classification of these features to be able to examine the distribution of landslide deposits across all of Yellowstone National Park.

Our movement inventory was similarly very specific in scope; it adds a temporal dimension to the LiDAR inventory, but it is also still a short snapshot in the potentially long histories of these landslides. We can only speculate about the context in which our five measured years of movement have occurred; this may have significant implications for the processes that

shape these features. We were also limited by SAR's inability to make accurate measurements under snow cover, potentially obscuring interesting temporal patterns in the behavior of the landslides we examined. We assumed that frozen ground was unlikely to experience creep, but that is not always true (Coe et al., 2003) and the displacement measurements on the Flagg Ranch landslides challenge this assumption.

4.3. Opportunities

Despite its limitations, this study sets a robust foundation for future work. These inventories together serve as contextual data sets for any future study of landslides in Yellowstone; they identify thousands of potential features of interest. The LiDAR polygons are a valuable spatial data set that represents thousands of hours of work and can be used to easily and quickly define attributes of these landslides that we have not yet collected. These attributes could include a host of topographic characteristics including slope, aspect, elevation, roughness, curvature, and aspect ratio all of which could be used in a statistically robust susceptibility analysis (e.g. Reichenbach et al., 2018). Though we focused on identifying patterns on a parkwide scale, future work could examine more local patterns, such as the distribution of landslide deposits within particular rock types, within different drainage basins, or between Yellowstone's two major climate zones (Brown et al., 2021). Future LiDAR acquisitions could be compared against this inventory and may help to identify event-triggered landslide movements or north-south creeping movements.

Our InSAR movement inventory raises multiple questions about the temporal behavior of these landslide deposits. We have identified distinct temporal behaviors on three different landslides throughout the park. Other studies have linked specific climate patterns to landslide

behavior (e.g., Handwerger et al., 2013; Bennett et al., 2016) and we would love to compare the Lava Butte, Silvergate, and Flagg Ranch landslides to potential local and regional triggers. We had hoped to be able to extract displacement measurements for dozens of creeping landslides in order to assess the spatial similarity of displacement patterns but were stymied by coherence issues in the InSAR data set. Such a study would provide exciting insight into the processes that manifest as different displacement patterns and Yellowstone's highly clustered population of landslides offers a perfect opportunity to study the scale of those processes.

We also hope that this study inspires further InSAR research in Yellowstone that is not necessarily focused on landslides. InSAR has been previously used to study the broad scale deformation of the caldera (e.g., Kelevitz et al., 2021), but to our knowledge, has not been applied to other features. We identified several patches of movement throughout the park that were not associated with LiDAR mapped landslide deposits. Given that Yellowstone contains abundant surface-rupturing faults and hydrothermal systems that move water through the subsurface, we wonder if InSAR might be used to study some of these processes. SAR data are widely available and tools like Hyp3 and MintPy greatly increase the ease of processing stacks of interferograms for time series analysis.

4.4. Recommendations for Future Landslide Inventories

This study serves as a valuable foundational characterization of landslide hazards in Yellowstone. Park managers may use this inventory to better prioritize areas for landslide hazard mitigation, and to better understand and prepare for the risks associated with those hazards. Crossing multiple state borders, this inventory fills several small gaps in a national inventory (Mirus et al., 2020). We know that Yellowstone's dynamic landscape will continue to evolve

over a range of timescales and this data set (both the LiDAR and the InSAR) can be used as a baseline from which to study the effects of dramatic events (like the June 2022 floods) or climate change over the foreseeable future.

Additionally, this work highlights the importance, often repeated, of recognizing where landslides have occurred in the past (Highland and Bobrowsky, 2008). These past occurrences are not necessarily discrete events, but rather they evolve continuously over a range of time scales. Understanding this evolution is fundamental to understanding how landscapes form and change over time and may have important implications for characterizing hazards.

In terms of making progress towards a much-needed universal set of methods for creating landslide inventories (Guzzetti et al., 2012), this study really raises more questions than it answers. We have a couple of takeaways for future preparers of landslide inventories:

1. **Consider the open-slope debris flow.** To our knowledge, open-slope debris flows are rarely mapped. We do not believe that they are features unique to Yellowstone; Lingbloom (2022) mapped them adjacent to our study area in Grand Teton National Park. Examples of features with similar morphologies have been otherwise mapped as debris avalanches (e.g., Geertsema et al., 2006; Coe et al., 2016), though the classification is generally non-specifically defined (Hung et al., 2014). We believe that the open-slope debris flow is grounded in direct observations and makes an important distinction between earthflows and flow-type deposits that mobilize larger material.

2. **Include rock glaciers in landslide inventories.** Rock glaciers transport sediment down valleys, exhibit creeping behavior, likely form via mass movements and often share some morphological characteristics with landslide deposits. Because of their interstitial ice, they deserve their own classification, separate from open-slope debris flows that may be mobilized by liquid water, but we believe that rock glaciers play important landslide-like roles in landscape evolution and natural hazard assessment.

3. **Reactivations need to be addressed.** Existing mapping protocols suggest noting the most recent known date of motion, but do not systematically address the role of continuous creeping motion within an inventory (Burns and Madin, 2009; Slaughter et al., 2017). Mapping reactivations and overlapping deposits raises questions about how we quantify and describe landslide area and how to define relative timing of events.

4.5. References

- Bennett, G.L., Roering, J.J., Mackey, B.H., Handwerger, A.L., Schmidt, D.A., and Guillod, B.P., 2016, Historic drought puts the brakes on earthflows in Northern California: Drought Puts Breaks on Earthflows: *Geophysical Research Letters*, v. 43, p. 5725–5731, doi:10.1002/2016GL068378.
- Brown, S.R. et al., 2021, Multi-proxy record of Holocene paleoenvironmental conditions from Yellowstone Lake, Wyoming, USA: *Quaternary Science Reviews*, v. 274, p. 107275, doi:10.1016/j.quascirev.2021.107275.
- Burns, W.J., and Madin, I.P., 2009, Protocol for Inventory Mapping of Landslide Deposits from Light Detection and Ranging (lidar) Imagery: Oregon Department of Geology and Mineral Industries Special Paper 42, 36 p.
- Coe, J.A., Baum, R.L., Allstadt, K.E., Kochevar, B.F., Schmitt, R.G., Morgan, M.L., White, J.L., Stratton, B.T., Hayashi, T.A., and Kean, J.W., 2016, Rock-avalanche dynamics revealed by large-scale field mapping and seismic signals at a highly mobile avalanche in the West Salt Creek valley, western Colorado: *Geosphere*, v. 12, p. 607–631, doi:10.1130/GES01265.1.
- Coe, J.A., Ellis, W.L., Godt, J.W., Savage, W.Z., Savage, J.E., Michael, J.A., Kibler, J.D., Powers, P.S., Lidke, D.J., and Debray, S., 2003, Seasonal movement of the Slumgullion landslide determined from Global Positioning System surveys and field instrumentation, July 1998–March 2002: *Engineering Geology*, v. 68, p. 67–101, doi:10.1016/S0013-7952(02)00199-0.
- Geertsema, M., Hungr, O., Schwab, J.W., and Evans, S.G., 2006, A large rockslide–debris avalanche in cohesive soil at Pink Mountain, northeastern British Columbia, Canada:

- Engineering Geology, v. 83, p. 64–75, doi:10.1016/j.enggeo.2005.06.025.
- Guzzetti, F., Mondini, A.C., Cardinali, M., Fiorucci, F., Santangelo, M., and Chang, K.-T., 2012, Landslide inventory maps: New tools for an old problem: *Earth-Science Reviews*, v. 112, p. 42–66, doi:10.1016/j.earscirev.2012.02.001.
- Handwerger, A.L., Roering, J.J., and Schmidt, D.A., 2013, Controls on the seasonal deformation of slow-moving landslides: *Earth and Planetary Science Letters*, v. 377–378, p. 239–247, doi:10.1016/j.epsl.2013.06.047.
- Highland, L.M., and Bobrowsky, P., 2008, *The Landslide Handbook- A Guide to Understanding Landslides*: United States Geological Survey Circular Circular 1325, 129 p.
- Hungr, O., Leroueil, S., and Picarelli, L., 2014, The Varnes classification of landslide types, an update: *Landslides*, v. 11, p. 167–194, doi:10.1007/s10346-013-0436-y.
- Kelevitz, K., Tiampo, K.F., and Corsa, B.D., 2021, Improved Real-Time Natural Hazard Monitoring Using Automated InSAR Time Series: *Remote Sensing*, v. 13, p. 867, doi:10.3390/rs13050867.
- Licciardi, J.M., and Pierce, K.L., 2018, History and dynamics of the Greater Yellowstone Glacial System during the last two glaciations: *Quaternary Science Reviews*, v. 200, p. 1–33, doi:10.1016/j.quascirev.2018.08.027.
- Lingbloom, J., 2022, *A Landslide Inventory and Analysis for Grand Teton National Park, Wyoming* [MS Thesis]: Idaho State University, 95 p.
- Mirus, B.B. et al., 2020, Landslides across the USA: occurrence, susceptibility, and data limitations: *Landslides*, v. 17, p. 2271–2285, doi:10.1007/s10346-020-01424-4.
- Reichenbach, P., Rossi, M., Malamud, B.D., Mihir, M., and Guzzetti, F., 2018, A review of statistically-based landslide susceptibility models: *Earth-Science Reviews*, v. 180, p. 60–

91, doi:10.1016/j.earscirev.2018.03.001.

Slaughter, S.L., Mickelson, K.A., Biel, A., and Contreras, T.A., 2017, Protocol for Landslide Inventory Mapping from LiDAR Data in Washington State: Washington Geological Survey Bulletin 82, 35 p.